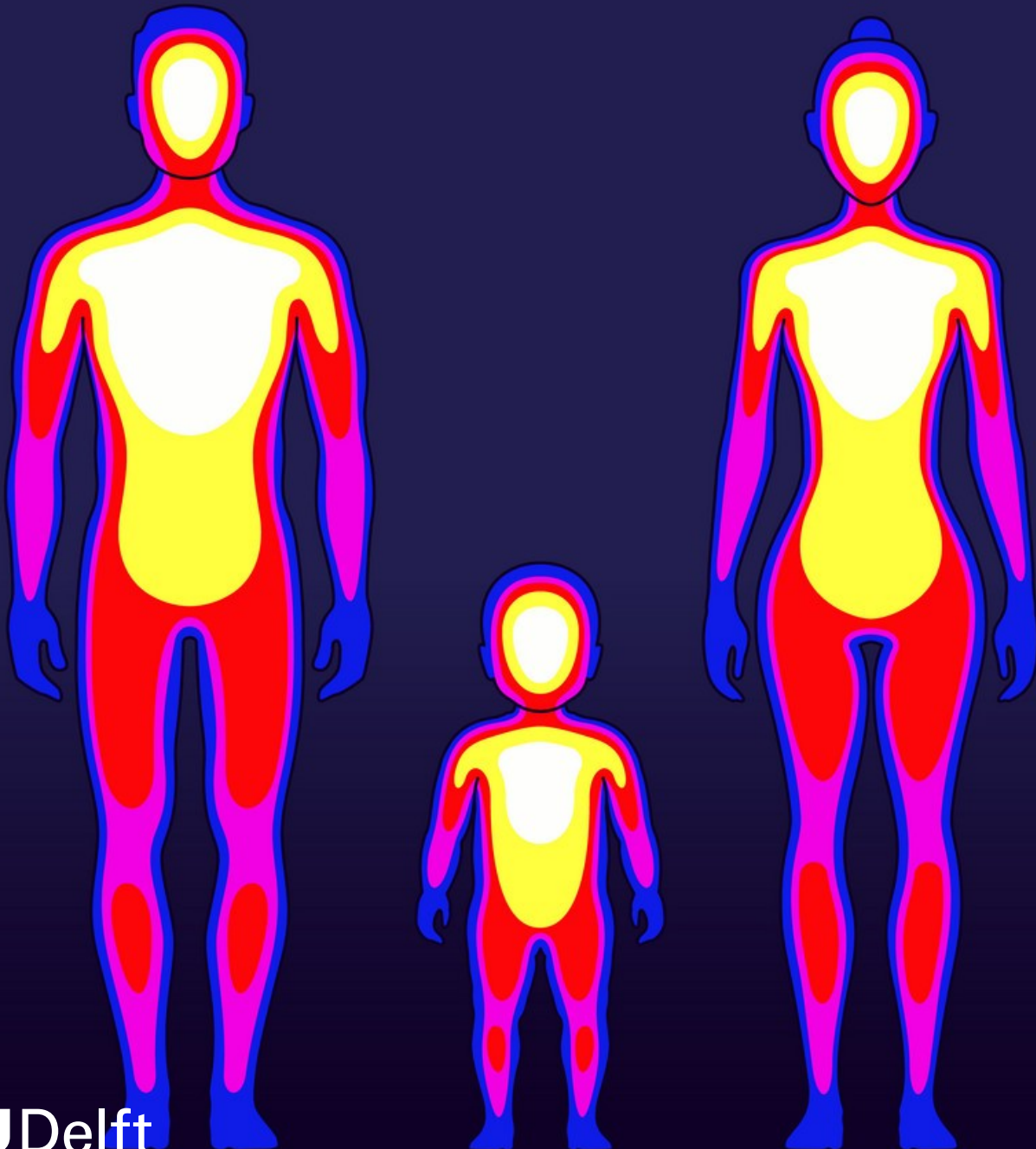


Predicting Infection Using Infrared Thermography in Premature Infants

Quantifying the Interaction Between Infrared Thermography and a Neonatal Incubator
B. Bosma

Technische Universiteit Delft



Predicting Infection Using Infrared Thermography in Premature Infants

Quantifying the Interaction Between Infrared Thermography and a Neonatal Incubator

by

B. Bosma

to obtain the degree of Master of Science
at the Delft University of Technology,
to be defended publicly on Wednesday February 24, 2021 at 13:30 PM.

Student number: 4240898
Project duration: July 2, 2018 – November 29, 2019
Thesis committee: Prof. dr. ir. W. A. Serdijn, TU Delft, supervisor
Dr. ir. G. de Graaf, TU Delft
Dr. R. Delfos, TU Delft
Prof. dr. ir. P. P. Jonker, TU Delft, supervisor

This thesis is confidential and cannot be made public until March 1, 2022.

An electronic version of this thesis is available at <http://repository.tudelft.nl/>.

Abstract

Predicting when a neonate will fall victim to an infection or a disease allows prevention through early medicine administering. Such physiological conditions can be made visible using infrared thermography (IRT). This is a technique for measuring heat emitted in the infrared spectrum and transforming them into visible signals that can be recorded photographically. This thesis will contribute to the prediction of infection in (pre)term neonates by quantifying the interaction between IRT and a neonatal incubator without (and with) a neonate in it.

A system was designed that consisted of three modules: a measurement (incubator and IRT camera), back-end (embedded system and server), and front-end module. The scope of this thesis is limited to the measurement module and the embedded system of the back-end module. Minimum camera requirements were set up which required the camera to: be inexpensive (i.e. $\leq \text{€}1000,-$), be mobile, be open-source (for Linux), have a minimum frames-per-second of 5, have a resolution of at least 160x160 pixels with a field of view (FOV) of 27°, sensitivity of $< 0.1^\circ\text{C}$, and safe to the patient. Such a camera was found in the FLIR One Pro. For this thesis a different FLIR camera was used due to lack of budget, namely the FLIR A305sc, which was already available at the TU Delft. The A305sc is not open-source, which required a work-around. The Aravis Open Source Project allowed for communication with the camera. Internal camera parameters had to be determined to calculate temperature based on analogue-to-digital values. ExifTool was used on a file stored by the camera to extract these parameters. This calculated temperature was compared to the temperature as determined by FLIR's software and led to a difference in the range of $1 \cdot 10^{-6}^\circ\text{C}$. An open-source application was written that can connect with this IRT camera that has a GenICam interface using Aravis. Additionally, this application implemented the temperature calculation based on the internal camera parameters.

The hood of the incubator is opaque to infrared, which required the design of a measurement setup to circumvent this. Three different setups were discussed, with the final choice falling on placing the camera in front of an opened incubator porthole on a tripod, and sealing this porthole with high or low density ethyl polyethylene (HDPE/LDPE). Regular H/LDPE used for construction site was found to have an attenuated transmissivity as found in literature. To quantify the interaction between IRT and a neonatal incubator, the IRT measurements were to be compared against the current golden standard sensor, namely thermistors. These sensor values were to be read out from the incubator as this would also be used in the final product. Code was written which allows for automatic detection between the GE GiraffeTM Omnibed and the Dräger Caleo[®] incubator, automatic connecting, and manipulation of all sensors values to a standard string which allows for easy uploading to the InfluxDB database on the server.

To be allowed to perform measurements on human subjects, approval had to be acquired by the human research ethics committee (HREC) of the TU Delft and the respective hospital. A “non-wet medisch wetenschappelijk onderzoek met mensen” (nWMO) request was submitted and approved, which resulted in 25 recorded sick and healthy neonates in incubators divided over two hospitals (the JKZ in The Hague, and the RDGG in Delft), with over 25 hours of recording material. Simultaneously, measurements were performed on an empty incubator to gain an understanding in the behaviour of an incubator when actors from outside interacted with the internal environment. Measurements that were performed included determining the reflected apparent temperature (RAT) for every possible opened porthole and for both incubator types. The RAT for the Caleo was found to be higher for every measurement for the GE. The accuracy of the IRT and hospital skin temperature sensors was compared against a calibrated Pt-100 sensor, which shows that the Pt-100 sensor measures an equal value as the hospital skin temperature sensor, whereas the IRT camera measured $.6^\circ\text{C}$ higher. The effect of changing the distance on IRT values was measured, which shows that for a distance of 0.2m to 1.2m the accuracy of the IRT camera is within the specified accuracy. Finally, the effect of opening additional portholes on IRT was measured, the effect of the airboost setting on IRT, and the measurement of opening additional portholes was repeated with a different IRT camera. Overall the IRT camera measures a higher temperature than the hospital skin temperature sensors, but follows the skin temperature sensors' pattern.

Preface

Dear reader,

Before you lies the result of a journey that has seen it all: success, failure, everything in between, and at one point even the brink of a complete stop. It began with a simple interview to be allowed to write this thesis. Not short after, personal circumstances led to postponing the actual start with two months. My supervisor, at the time, was very understanding, which I would like to thank him for. Sadly, over the course of time, we began to have our differences and had to part ways.

Study advisor Drs. Evert Vixseboxse contacted Prof.dr.ir. Wouter Serdijn with my story, after which he became my new supervisor, for which I am grateful. They have listened to my story, and allowed for a happy ending of this thesis. Not only has their personal guidance given me the motivation and drive to finish this thesis, prof.dr.ir. W. Serdijn's substantive guidance ensured it was worthy of a master's degree.

A very big thanks to the hospital staff. From the RDGG I would like to thank the physician Laura van der Meer-Kappelle and all the nurses who have provided their support during their regular duties. From the JKZ I would like to thank physician Gertjan Driessen and all the nurses. Without you, there would have been no measurements.

I would like to thank my parents, *Marjanne Helmus & Bart Bosma*, who have always been there to listen to me, to provide support, to provide distraction during rough times. Even though they both do not have a technical background, they would try to think with me when I was stuck. I appreciate everything you have done, and continue to do for me.

Finally I would like to thank my girlfriend, *Catharina Nijholt*, who, even though she was on a continent 9000km away, would still find time to listen, to support me, and in general be there for me. I would not have made it without you.

Back to you, reader. I hope that this work can provide a building block in whatever goal you pursue with this knowledge. I want to give one big final thank you to all the people that have been there for me, in whatever seemingly insignificant manner. Bedankt.

B. Bosma
Bolsward, February 2021

Contents

Abstract	iii
1 Introduction	1
1.1 Thesis Objectives	2
1.2 Thesis Outline	3
2 Neonates	5
2.1 Skin	5
2.2 Thermoregulation	6
2.2.1 Hypothermia	6
2.2.2 Hyperthermia	6
2.3 Disease in neonates	6
2.3.1 Sepsis	7
2.3.2 Anemia	7
2.3.3 Rubella	7
2.3.4 Cytomegalovirus (CMV)	7
2.3.5 Breathing Problems	8
2.4 Conclusion	8
3 Thermography	9
3.1 Thermal Measurements	9
3.2 IR Cameras	11
3.2.1 Bolometer	11
3.3 Measurement Errors	11
3.3.1 Microbolometer Noise	13
3.3.2 Calibration	13
3.3.3 Camera Angle Effect on Emissivity	13
3.3.4 Condensation	14
3.3.5 Anti-Fog Coatings	14
3.4 Gold-Standard Temperature Measurements	15
3.5 Incubators	15
3.5.1 Incubator Hood Material	16
3.5.2 Incubator Evaluation	17
3.5.3 Polyethylene	19
3.6 IRT Research in Humans	19
3.6.1 IRT Research in (Premature) Neonates	20
3.7 Conclusion	20
4 Image Processing	21
4.1 Moving Average	21
4.2 Median Filter	21
4.3 Wavelet Transform	22
4.3.1 Denoising Image using Wavelet Transform	23
4.4 Fuzzy Logic	24
4.4.1 Denoising Image using Fuzzy Logic	24
4.5 Artificial Intelligence	25
4.5.1 Machine/Deep Learning	26
4.5.2 Deep Learning	27
4.5.3 Classification using Deep Learning	29
4.6 Conclusion	29

5	System Design	31
5.1	Minimum System Requirements	32
5.2	Measurement Module	32
5.2.1	Placing the Camera in Front of an Open Porthole	32
5.2.2	Placing the Camera in Front of an Open Porthole Sealed with IR Transmissive Material	33
5.2.3	Placing the Lens Inside a Tightly Fitting Gap	34
5.3	Back-end Module	35
5.4	Front-end Module	35
5.5	Conclusion	35
6	Infrared Thermography Camera	37
6.1	Selection	37
6.1.1	Seek Thermal	38
6.1.2	FLIR	38
6.1.3	Final Choice	39
6.2	Noise Reduction	39
6.3	Internal Camera Parameters	40
6.3.1	Temperature Parameters	40
6.3.2	Atmospheric Parameters	42
6.4	Conclusion	43
7	Software	45
7.1	Pre-Processing Block Diagram	45
7.2	Open Source GenICam Tools	46
7.2.1	Aravis Open Source Project	47
7.3	Incubator Communication	47
7.3.1	GE Giraffe™ Omnibed	48
7.3.2	Dräger Caleo®	48
7.3.3	Combining Both Incubator Types	51
7.3.4	Store Measurement in Influxdb Database	51
7.4	Conclusion	52
8	Data Acquisition Preparation and System	53
8.1	Human Research	53
8.1.1	HREC TU Delft	53
8.1.2	HREC Southwest Holland	54
8.1.3	Board of Directors	55
8.1.4	Flowchart of Forms and Proposals for HREC	55
8.2	Patients	55
8.3	Study Protocol	56
8.4	Experimental Settings	57
8.4.1	Temperature Sensors	57
8.5	IRT Camera Data Acquisition	59
8.6	Conclusion	60
9	Measurements	61
9.1	Missing Data	61
9.2	Quantifying Interaction Between IRT and Incubator	61
9.2.1	External Optic Window	62
9.2.2	Reflected Apparent Temperature (RAT)	63
9.2.3	Accuracy GE Temperature Sensor	64
9.2.4	Changing the Distance from Camera to Incubator	64
9.2.5	Opening Portholes	66
9.2.6	Airboost	68
9.2.7	Testo 890	70
9.3	Neonatal Measurements	71
9.4	Conclusion	72

10	Result Interpretation & Discussion	73
10.1	IRT Behaviour During Incubator Measurements	73
10.1.1	External Optic Window	73
10.1.2	RAT	73
10.1.3	Accuracy GE Temperature Sensor	75
10.1.4	Changing the Distance from Camera to Incubator	76
10.1.5	Opening Portholes	78
10.1.6	Airboost	80
10.1.7	Testo 890	81
10.2	Neonatal Measurements	81
10.3	Conclusion	82
11	Conclusions and Recommendations for Future Work	83
11.1	Conclusions	83
11.1.1	Limitations	84
11.2	Thesis' Contributions to Science	84
11.2.1	Open-Source IRT Camera Recording Application	84
11.2.2	Incubator Detection and Logging Application	84
11.2.3	Quantification of the Interaction Between IRT and Incubator	84
11.2.4	Data Collection	85
11.3	Recommendations for Future Work	85
11.3.1	Combining IRT Camera Recording Application with Incubator Detection Application	85
11.3.2	Quantifying Interaction Between IRT and Incubator	85
11.3.3	Data Collection	86
11.3.4	Future Work	86
A	Neutral Thermal Environmental Temperatures	87
B	Checklist HREC TU Delft	91
C	Ethics Application Full Proposal	97
D	Informed Consent Leaflet and Written Consent Form	103
E	WMO Checklist	109
F	Flowchart	113
G	GE Giraffe Omnibed Parameter Definition	115
H	Medibus Specification for Caleo	119
I	Opening Portholes - Filming Through Port 4	127
J	Changing Distance from Camera to Incubator	131
J.1	Porthole Covered with HDPE	132
J.2	Porthole Covered with LDPE	133
K	Pt-100 Certificate of Calibration	135
	Bibliography	139

1

Introduction

Prematurity is the leading cause of death in children under-5. 5.9 million under-5 deaths occur globally, of which 1.055 million are due to preterm birth complications. This is the second most common cause of death after pneumonia [53]. Prematurity also increases the risk of death due to other causes, especially neonatal infections [81]. Moreover, long-term complications are associated with prematurity. Approximately 15% of all preterms develop cerebral palsy, and as much as 50% develop cognitive and behavioural deficits [51]. As such preterms require specialized care in the neonatal department of the hospital, in so-called neonatal intensive care units (NICUs). Only 10 hospitals have such a department in The Netherlands [60]. In these NICUs, preterm neonates often are placed in an incubator, which is able to regulate the environmental temperature and humidity for the neonate, as they are unable to do so for themselves yet. Oxygen levels can also be controlled, depending on the type of incubator.

Within an incubator, a neonate can be monitored via sensors placed using adhesive pads. Nurses and physicians are hindered by said pads, and the wires attached, when they have to reach the neonate. Not only are hospital staff members hindered by sensors connected to the neonate, they also present discomfort to the neonate. Sadly, a neonate is not able to convey whether it is experiencing discomfort, or even worse, pain.

Infrared (IR) thermography (IRT) is a non-obtrusive, non-invasive method of monitoring physiological signals from a distance. Cameras designed to detect this radiation produce thermograms, which are images of said radiation. This technology can eliminate certain types of discomfort due to sensor wires and detect physiological changes. As the price of infrared thermography cameras start to reach affordable prices, it has found its way into the medical scene, with the first use of infrared thermography in detecting breast cancer as early as the 1950s [101]. In the following years, IRT was used in a multitude of medical applications, e.g. diabetic neuropathy [116],[79], vascular disorder [78], brain imaging [118], etc.

The material of the hood of the incubator is often chosen to be plexiglass. This material is completely opaque to radiation with wavelengths that humans emit [105]. All modern neonatal incubators have portholes on their sides which can be opened or closed. These exist to provide an easy entry for the nurse or physician to provide care for the neonate and disturb the internal environment as little as possible. The most obvious workaround is to position the camera in such a way that it can record through an opened porthole. When such a porthole is opened or closed, the thermal system within the incubator changes. It is therefore important to quantify the thermodynamic system of the incubator under these different conditions, e.g. when the incubator has not been touched and is considered in thermal equilibrium (under the assumption that at least one porthole has been opened so that IRT images can be made), and when the system has been changed due to outside actors. This will be done using the current golden standard for temperature measurements: negative/positive thermal coefficient (NTC/PTC) thermistors. Temperature measurements are preferably made at locations that closely reflect the core temperature. These are performed at so called “intermediate sites”, e.g. the rectum, bladder, and mouth. However, using IRT, skin surface temperatures are measured [3]. As such, of interest is the location where skin surface temperatures are measured. Multiple locations are possible to place a temperature sensor, but in The Netherlands it is most often placed underneath the diaper in the groin. These temperature sensors are connected to the incubator and displayed on the display. It is important to relate this golden standard to IRT recordings.

Once IRT interaction with an incubator has been quantified, it can be assured that the influence of the

incubator's thermal system on the IRT images and recordings can be compensated. Only then will IRT recordings correspond to the actual thermal status of the neonate. These recordings will then have to be visually analysed. This requires a human with expertise in the respective field to diagnose an image. An individual capable of doing so has probably followed a specific education. Over the years this individual will have learned to recognize healthy and unhealthy subjects based on their thermographic images. Even then, such a task is cumbersome, requires years of training, and is still prone to subjective judgement errors. This task would benefit from objective judgement performed by a computer. A computer can also learn to diagnose images, given that it is fed enough information [58]. This is a branch of artificial intelligence (AI) and is called machine learning (ML). In recent years ML has experienced an immense resurgence, as computational power has increased and is still increasing at a high pace.

The social and scientific relevance of this study are such that future work that aims to perform research in predicting infection in premature neonates can use this thesis to gain understanding in the interaction between incubators and IRT cameras. When that aspect is well understood, research can focus quicker on predicting infection using IRT. This can lead to a decrease in morbidity and mortality.

1.1. Thesis Objectives

An infection only becomes apparent by clinical signs and symptoms or by laboratory examinations. By then, the neonate has already fallen ill. One would prefer to prevent the infection, even though infections can be cured with antibiotics. In neonates it is difficult to determine which children need them. Current guidelines lead to over-treatment of neonates with antibiotics. Therefore, new methods are necessary to help clinicians to distinguish neonates with infections from children without infections. IRT may be such a method. Therefore the overall research question is:

“Can we predict disease in (pre)term neonates by using pattern recognition on early onset heat patterns using infrared thermography?”

However, such a research question is too complex for merely a master thesis. Such a research question can be split into smaller parts more suitable for a master thesis. This thesis will research how the current golden standard relates to IRT recordings, which will then be used to quantify the thermodynamic system of the incubator under different conditions. This thesis will contribute to the overall research question by answering the following smaller research question:

“Can we quantify the interaction between IRT and a neonatal incubator without (and with) a neonate in it?”

Additional sub-questions are:

- What are requirements for the IRT camera, e.g. accuracy, refresh rate, price?
 - What could be a suitable IRT camera given the requirements?
 - Can an open-source application be written to communicate with the camera?
- What are restraints for a possible measurement setup due to technical limitations and/or nurse/paediatrician request?
- How does IRT perform quantitatively when measuring from one system (roomtemperature) into another system (incubator) that is at a higher temperature/humidity at equilibrium?
 - Additionally, how does IRT perform quantitatively, when:
 - ◊ When compared to a calibrated Pt-100 sensor?
 - ◊ When the distance is changed between camera and incubator?
 - ◊ When one or more portholes are opened?
 - ◊ When a setting has been activated which prevents warm air from escaping?
 - ◊ When one type of camera is compared with another type of IRT camera?
 - ◊ When an external optic window is used?
- Can an application be written to read out sensor values from an incubator?
- Can a measurement protocol be devised that allows the researcher to perform measurements on neonates?

1.2. Thesis Outline

This literature will adhere to the following structure:

Chapter 2 through 4 consist of the literature study performed for this thesis. Chapter 2 will discuss premature neonates – when a neonate is defined as premature, what the consequences of prematurity are, i.e. to which diseases they are prone, and how they are kept safe. Chapter 3 describes the technology used in this thesis: infrared thermography (IRT). A small side step will be made to discuss measurement reports on incubators. This chapter then concludes with IRT research performed on humans and premature neonates. Chapter 4 describes methods to reduce noise in images, and concludes with artificial intelligence (AI), and how a branch of AI, deep learning, has been used with medical images. Chapter 5 provides a high level oversight of the system that is to be developed and its requirements. Several implementations are discussed and the best suitable option is chosen. Chapter 6 describes in detail possible options for an IRT camera to be used in this thesis, and the inner workings of the camera that was used. Chapter 7 provides a block diagram of the steps required prior to developing a prediction algorithm. It then describes in detail the software that was used and written for this thesis. Chapter 8 describes how approval to do research in a hospital was acquired and in detail describes the data acquisition. Chapter 9 describes in detail all measurements that were performed and displays all acquired data. Chapter 10 then elaborates on the measurements by interpret all data and provides a discussion per measurement. Chapter 11 provides a conclusion on the research (sub-)questions posed in this chapter.

2

Neonates

This chapter will provide a literature study on preterm neonates and describe their skin and thermoregulation. Due to their underdeveloped thermoregulation, they are more prone to hypo-, and hyperthermia, which is described afterwards. Finally several diseases neonates are prone to will be listed together with their symptoms.

Babies born alive before gestation has reached 37 weeks are called *premature neonates*, or *preterms*. Annually it is estimated that 15 million babies are born prematurely [14]. Preterm birth can be divided into three subcategories based on the duration of gestational age (GA): *extremely preterm* (GA less than 28 weeks), *very preterm* (GA of 28 to 32 weeks), and *moderate to late preterm* (GA of 32 to 37 weeks). Many organs in preterms have not fully developed yet, including the brain, lungs, and liver. This can cause serious disability or death [15]. Similarly to preterms, babies that have low birth weight (< 2500g) also require specialized care. Low birth weight babies can be divided into two subcategories: *Very Low Birth Weight* (VLBW) (weight < 1500g) and *Extreme Low Birth Weight* (ELBW) (weight < 1000g). A primary cause of VLBW is premature birth [21].

2.1. Skin

The skin is the largest organ of the body. It provides a barrier against UV radiation, pathogens, and regulates body temperature and sensory perception in adults. These functions are not readily available after birth, even less so in premature neonates. After birth, in term neonates, the skin starts to develop immediately, and reaches maturity in the first year. This development only starts in preterm neonates after two to three weeks after birth, and can only then be compared to a term neonate's skin [113]. The skin consists of two layers: the epidermis, and dermis. The epidermis is a superficial layer, which also consists of layers. The corneum stratum is the outer layer of the epidermis and is formed at 21 weeks of gestation. Both the epidermis and the corneum stratum have lower thickness in preterm neonates than those of adults [22]. As such, skin temperature measurements taken approach core temperatures [23]. Moreover, such a thin epidermis requires careful treatment of the preterm. The basal layer, which generates epidermis, can be easily damaged which consequently leads to scar formation during healing [25]. Skin adhesives provide another challenge, as removal increases transepidermal water loss (TEWL) at the removed adhesive location, which is correlated with damaged skin barrier function [30]. In an effort to control TEWL, restore skin elasticity, and skin homeostasis sustenance, emollients can be applied to the skin [38]. There is some controversy surrounding emollients, as some claim it increases the risk of infection [39], whereas others have found a reduction of nosomical infections when sunflower oil was topically applied, without side effects [41]. Due to the thinner corneum stratum, the skin is highly permeable to topically applied agents. If such agents are absorbed, they can cause toxic systemic effects, which lead to illness, and even death [34]. Similarly, repeatedly applying disinfectant such as isopropyl alcohol can induce systemic intoxication and can cause severe haemorrhagic skin necrosis [37].

TEWL should be reduced as much as possible. Environmental humidity aids TEWL reduction and supports temperature regulation, fluid and electrolyte management, and skin integrity. All very premature neonates who are < 2 weeks of age should be nursed inside an incubator with a high environmental humidity. After the first week, humidity should be reduced linearly. The first seven days of life they require an environmental humidity of 80%, with a decrease of 5% every consecutive day afterwards. On day 15, the

environmental humidity should have reached 45% and the premature neonate should no longer require an incubator. At this point the epidermis should behave as an effective barrier. These are merely guidelines and should be discussed with the medical staff [95].

2.2. Thermoregulation

Humans are homeotherm, which means humans aim to preserve their body temperature regardless of their environmental temperature. The oral temperature is around 37°C, whereas the core temperature is 0.6°C higher and can be measured rectally. The body relies on this temperature as most functions and tissues are in homeostasis. Only a few degrees variation from the core temperature is an indicator for a dysfunction in the body [42]. Neonates require a very specific core temperature: 36.5°C–37.5°C rectal and a thermoneutral environment (TNE) to prevent the neonate from thermal stress. This is however dependent on whether the neonate is clothed or not. A very preterm neonate's TNE is kept at 34°C–35°C naked, and 28°C–30°C clothed [77]. Moreover, the temperature range that a neonate should be warmed at, differs greatly depending on weight, age of gestation, and age of life. A table with neutral thermal environmental temperatures per age and weight is shown in Appendix A [24].

Adults produce heat in response to cold body temperatures by peripheral vascular constriction, inhibition of sweating, voluntary muscle movements, involuntary muscle movements, and nonshivering thermogenesis. Neonates are considered homeotherm as they show increased metabolic rate at low ambient air temperature [46]. However, thermoregulation is different in neonates when compared to adults. Neonates primarily produce heat using nonshivering thermogenesis [43]. The heat produced by a neonate is highly dependent on the body weight, and can be calculated [61].

2.2.1. Hypothermia

Immediately after birth a neonate starts to lose heat. Neonates experience heat loss through four different mechanisms: convection, radiation, evaporation, and conduction [44]. Within the first few minutes of birth a neonate's temperature can drop 2–3°C, where deep body and skin temperature drop 0.1°C/min and 0.3°C/min, respectively [48]. This is due to a preterm neonate having less brown fat and glycogen which can produce heat. These reserves are often depleted in the first few moments after birth. Moreover, a preterm neonate has a three times lower body surface area per kilogram of body weight. This increases the heat transfer with the environment [97]. A neonate will experience hypothermia at temperatures lower than 36.5°C. From 36.5–36°C mild hypothermia occurs, also known as cold stress. Moderate hypothermia occurs from 36–32°C, whereas severe hypothermia occurs at temperatures lower than 32°C [45]. As hypothermia causes a neonate to increase its cellular metabolism as it tries to stay warm, this leads to increased oxygen consumption, which can cause hypoxia, cardiorespiratory issues, and acidosis. Glucose consumption is also increased to produce more heat. This can cause hypoglycemia. If hypothermia is allowed to progress, even brain damage, hyperbilirubinemia and clotting disorders can occur [50]. Hypothermia is linked with increased mortality globally [49].

2.2.2. Hyperthermia

A neonate can be warmed to counter hypothermia. However, this should be done with care. If a neonate is warmed too much, it is at risk of developing hyperthermia. Hyperthermia is defined as a body temperature of > 37.5°C, and should not be confused with inflammation due to infection [45]. Hyperthermia can cause hypotension, dehydration, seizures and apnea, and hyponatremia [50]. If the core temperature rises above 42°C, neurological damage can occur [45].

In an attempt to lose heat, a neonate's skin vessels will dilate, it will appear flushed, hands and feet are suffused and warm, and it will take a spread-eagle posture. This is all assuming that a neonate is physiologically capable of doing so. Although less common in premature neonates, term neonates will start sweating [84].

2.3. Disease in neonates

Infection in neonates is the leading cause of mortality in the first days of life [81]. Preterms have an immature immune system, which could even be further compromised due to other preterm birth associated factors. Due to this they are at an increased risk of infection [65]. Infection is caused by microorganisms, such as viruses, prions, bacteria, and viroids that have invaded the body. These microorganisms are fought off by

the body's immune system, which often involves inflammation. The classical signs of inflammation are pain, heat, redness, swelling, and loss of function. Infection always causes inflammation, however, inflammation does not always mean that there is an infection. Infection can be acquired through different manners:

- In utero (transplacentally, or via ruptured membranes).
Infection can occur any time before birth and results from maternal infection. Depending on the time of gestation when the infection takes place, and the type of infection, different consequences are possible, e.g. spontaneous abortion, stillbirth, limited growth within the uterus, premature birth, congenital malformation (e.g. rubella), asymptomatic, and symptomatic infection [66].
- In the birth canal (intrapartum).
Herpes, HIV, hepatitis B, group B streptococci, chlamydiae are just a few examples of the infections that can occur during birth through an infected birth canal [66].
- After birth from external sources (postpartum).
After birth during contact with an infected mother (TB, HIV), family, visitors, or hospital staff and environments, an infection can occur [66].

The chances of receiving an infection intrapartum and postpartum are decreased as age of gestation is increased. Symptoms tend to be nonspecific, e.g. vomiting, fever, hypothermia, tachypnea, rashes, diarrhea, etc [66].

2.3.1. Sepsis

Sepsis is an invasive infection and occurs in 0.77 to 1 out of 1000 births in the US [70]. LBW neonates, minorities, and males are at an increased risk of sepsis. If symptoms occur within 3 days of birth, it is considered early onset neonatal sepsis (EONS). This is usually acquired from organisms intrapartum. Late onset neonatal sepsis (LONS) is when symptoms occur 72 hours after birth for neonates in the NICU, versus 7 days of life in term neonates. For LONS pathogens are usually acquired from the environment. Sepsis has many nonspecific symptoms, including lethargy, hypothermia, and poor feeding, and nonspecific signs may include anuria and acidosis. When the presenting infection is pneumonia, symptoms can include apnea, tachypnea, grunting, nasal flaring, and intercostal retractions. Cardiac symptoms may include cyanosis, desaturation, bradycardia, poor perfusion, reduced capillary refill, and hypotension. Temperature instability, respiratory status changes, or feeding problems can indicate an infection [71].

2.3.2. Anemia

A person with anemia lacks red blood cells, which means the body does not circulate enough oxygen-rich blood. In adults this can lead to fatigue or a weak feeling. Some other symptoms can include shortness of breath, headaches, irregular heartbeat, or cold hands and feet. It can be a sign for a more serious condition, such as chronic bleeding, or chronic inflammation from an infection, kidney disease, cancer, or autoimmune disease. Different types of anemia exist, e.g. iron deficiency anemia, hemolytic anemia, sickle cell anemia, and other forms [82].

2.3.3. Rubella

Rubella is a rare disease as immunization programs have essentially eliminated this disease. It is acquired from the mother during pregnancy. The fetus may experience no symptoms, however, death in utero could occur. After birth a list of symptoms have been associated with rubella, and as such are called congenital rubella syndrome (CRS). Symptoms include birth restriction in utero, cataracts, hearing loss, and cardiac defects [67].

2.3.4. Cytomegalovirus (CMV)

This virus is often asymptomatic in neonates, yet 0.2 to 1% of live births worldwide suffer from congenital CMV. As CMV is infectious, perinatal CMV is acquired when a neonate comes into contact with infected cervical secretions, breast milk, or blood. Preterm neonates do not possess the antibody to CMV, and can potentially die from this infection. Symptoms include birth restriction in utero, jaundice, pneumonitis [68].

2.3.5. Breathing Problems

Premature neonates have not fully developed lungs which can lead to breathing problems. Term neonates do have fully developed lungs, but due to complications at birth, infection, or birth defects, they can also develop breathing problems. There are several conditions associated with breathing problems.

Apnea

Apnea has been defined as no breathing for extended periods of time, i.e. respiratory pauses longer than 2 to 5 seconds, however, in a clinical setting, it is defined as “a pause in breathing of longer than 10 or 15 seconds, often associated with bradycardia, cyanosis, or both.” [76]. Sleep apnea of prematurity is defined as respiratory pauses longer than 20 seconds, or pauses less than 20 seconds with associated bradycardia (< 80 beats-per-minute (BPM)), and no other disorders causing apnea. Onset is usually only after two to three days after birth. If it starts more than 14 days after birth, it could indicate serious illness, other than apnea. Two different types of apnea exist: obstructive sleep apnea, and central sleep apnea. In obstructive sleep apnea the upper airway is either partially or completely closed. In central sleep apnea the medullary respiratory control centers have not matured fully [69].

Pneumonia

Pneumonia in neonates is the second most common invasive bacterial infection, trailing primary sepsis. Untreated it can lead to high mortality and high morbidity [72]. Worldwide neonatal pneumonia is estimated at 10% of mortality cases, with the highest rates in developing countries [73]. Depending on gestational age, incubation status, the incidence varies. Reported incidences vary from 1% to 35%, 1% being the most common for term neonates, and 10% for preterm neonates. Pneumonia can be acquired in utero, intrapartum or postpartum. Pathogens include bacteria, viruses, and fungi which induce inflammation. Early onset neonatal pneumonia (EONP) occurs within 3 days of life, whereas late onset neonatal pneumonia occurs within 4 and 28 days of life. Symptoms are nonspecific and include respiratory distress of various degree, suspicious appearing tracheal aspirates, cough, apnea, high or low temperature, poor feeding, abdominal distension, and lethargy [74]. A predominant sign is tachypnea and is present in 60-89% of cases [75].

2.4. Conclusion

Premature neonates do not yet possess the ability to regulate their own temperature. Additionally, their skin is not as developed as a term neonate, which leaves them vulnerable to infections and diseases. Currently skin adhesives are used to place a sensor on the child. Upon removal of such an adhesive, the skin can be damaged. Because neonates can not convey when they experience discomfort or pain, other than crying, in this thesis an attempt will be made to predict one of the many infections or diseases a premature child can experience, without providing them additional discomfort or pain, i.e. using non-intrusive, non-invasive technology.

3

Thermography

This chapter will provide a literature study on thermography. The part of the electromagnetic spectrum IR is located in will be discussed, along with how infrared thermography cameras function. Measurement errors that can occur will be discussed. Then the current gold standard for measuring skin temperature will be elaborated. Then a sidestep will be made to incubators, their material and functioning. Finally some light will be shed on infrared thermography research that has already been performed on humans and (preterm) neonates.

Infrared thermography is defined by the Merriam Webster dictionary as “a technique for detecting and measuring variations in the heat emitted by various regions of the body and transforming them into visible signals that can be recorded photographically (as for diagnosing abnormal or diseased underlying conditions)”, i.e. the tool that will be used to achieve the goal of this thesis.

Despite the fact that IRT has originally been developed for military purposes, IRT has been used in the medical scene for approximately 50 years and has first been used to find breast cancer in women, although the findings may have been controversial [101]. Compared to X-ray, computed tomography (CT), and mammography, it is not harmful as it does not emit any (harmful) radiation. Hence it is considered a passive measurement. Other benefits of IRT are that it is non-contact, which improves hygiene, and IRT system can be portable and imaging can be done in real time.

3.1. Thermal Measurements

As mentioned in Sec. 2.2.1, neonates lose heat through four different mechanisms. Conduction is the transfer of energy from higher to lower temperature areas, convection is associated with the heat transfer between a solid and a moving medium (e.g. air) [87], evaporation takes place in the lungs and body surface and is dependent on alveolar ventilation and relative humidity (RH) of the surrounding environment, respectively [44]. Finally, radiation takes place through emission and absorption and takes place in the IR part of the electromagnetic spectrum. It is found at wavelengths from $0.75\mu\text{m}$ to $300\mu\text{m}$.

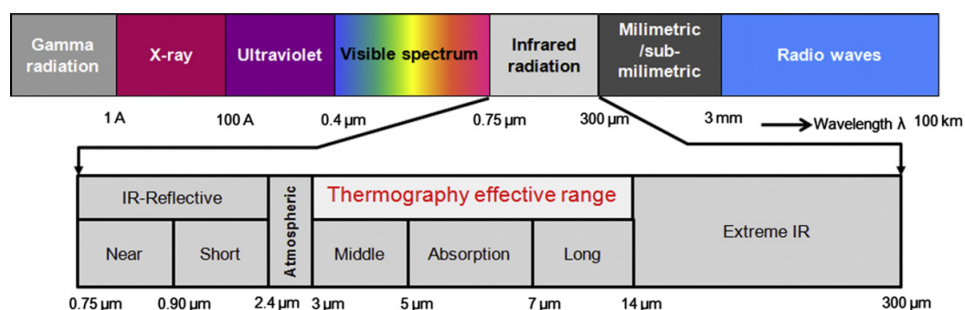


Figure 3.1: The electromagnetic spectrum with IR displayed in detail. Image taken from [85].

In Fig. 3.1 the IR band of the electromagnetic spectrum has been shown in detail. It can be divided

into five subbands: near, short, middle, long, and extreme IR. H₂O, CO₂, and other elements absorb certain wavelengths in the atmosphere, but from 3 to 5 μ m and from 7 to 14 μ m this absorption is less [100]. The transmission of the atmosphere for wavelengths of 1-28 μ m are depicted in Fig. 3.2.

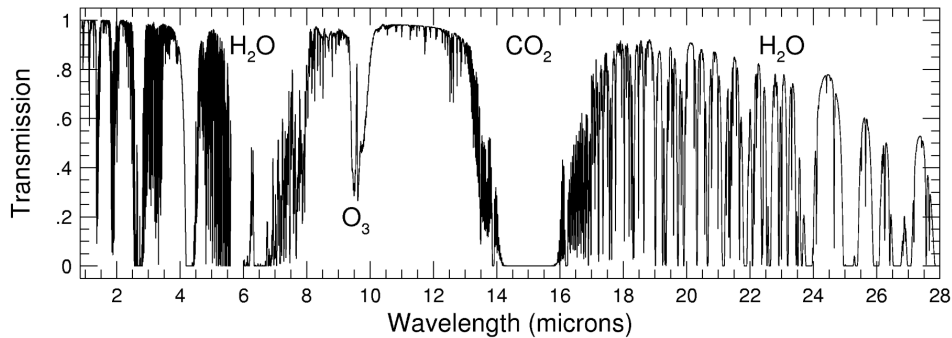


Figure 3.2: IR transmission of the atmosphere for the wavelengths 1-28 μ m. Image taken from [93].

The human body emits significant radiation at wavelengths ranging from 4-30 μ m, with a peak at 9 μ m, which falls in the long-wave IR band (LWIR) and slightly in the far-IR band [89]. Suppose the total radiation

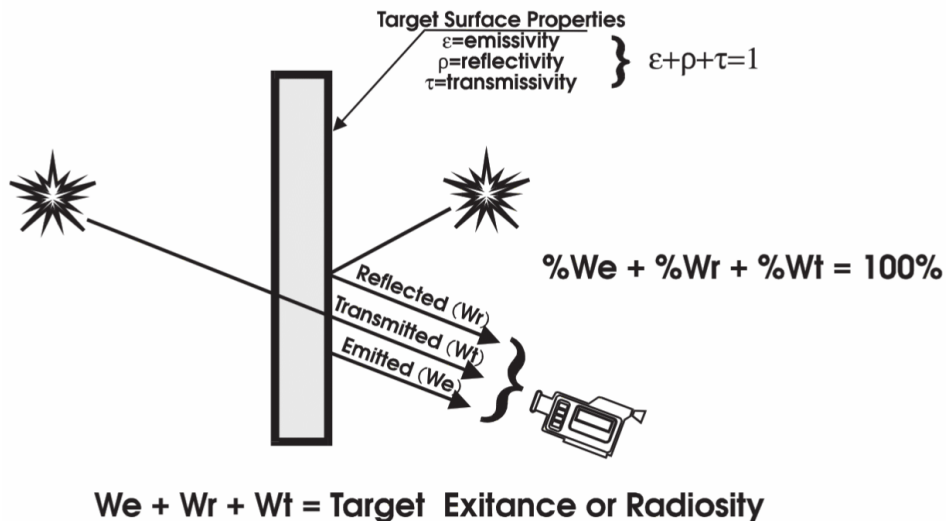


Figure 3.3: When interested in the radiation coming from a target surface T_e , the only variable of interest is the emitted radiation W_e , however, there are bound to be other radiation sources that reflect upon T_e or perhaps transmit through it, based on the material's emissivity, reflectivity, and transmissivity properties, respectively. Collectively these sum to 1. The contributions they deliver are W_e , W_r , and W_t respectively. Original image from [87].

from an object is to be measured. The total radiation, or exitance, is calculated by adding all three elements, $W_e + W_r + W_t$, as shown in Fig. 3.3. Often the variable of interest is only W_e , as this is the actual surface temperature of the target. Closely related to this is the emissivity (ϵ), which is defined as the fraction of light absorbed at a certain wavelength λ [89]. A theoretical material named a blackbody has an emissivity of $\epsilon = 1$ and will emit all its absorbed energy back. The Stefan Boltzmann law describes the power radiated per unit surface area across all wavelengths per unit time. This equation is given in Eq. (3.1). Here σ is the constant of proportionality, also known as the Stefan-Boltzmann constant, with a value of $\sigma = 5.670373 \times 10^{-8} [Wm^{-2}K^{-4}]$, and T the temperature in Kelvin.

$$\frac{P}{A} = \epsilon\sigma T^4 [j/m^2s] \quad (3.1)$$

However, all real materials have an $\epsilon < 1$, known as gray-bodies, and will not absorb all energy and can only emit what they absorbed. ϵ is a dimensionless number between 0 and 1 and is the ratio of energy radiated from the surface of a gray-body and a blackbody [104]. Equations for the radiation per radiation source are

given in Eq. (3.2-3.4) [139].

$$W_r = (1 - \epsilon)\tau\sigma T_r^4 \quad (3.2)$$

$$W_t = (1 - \tau)\sigma T_t^4 \quad (3.3)$$

$$W_e = \epsilon\tau\sigma T_e^4 \quad (3.4)$$

Summing all separate radiation sources lead to the total radiation picked up by the camera, and can be seen in Eq. (3.5). τ is the transmissivity of the atmosphere.

$$W_{\text{tot}} = (1 - \epsilon) \cdot \sigma T_r^4 + (1 - \tau) \cdot \sigma T_t^4 + \epsilon\tau\sigma T_e^4 \quad (3.5)$$

The transmittance of the atmosphere has been thoroughly studied. It is given by $\tau_{atm} \cong \tau_{H_2O} \cdot \tau_{CO_2}$. The transmissivity of water, τ_{H_2O} , depends on the number of absorbing molecules, on the partial pressure of water vapour, and the distance d travelled by radiation in the absorbing medium. The Passman-Larmore tables contain characteristics of the transmittance of IR in the range of 7.5-13 μm . Water vapour absorbance drops, τ_{H_2O} , as low as 0.947 for $\lambda = 7.5\mu\text{m}$, for $d = 200\text{m}$. Transmittance due to carbon dioxide absorbance, τ_{CO_2} , reaches as low as 0.987 for $\lambda = 12.5\mu\text{m}$, for $d = 200\text{m}$ [144]. Transmittance will only increase when decreasing the distance. For distances in the order of 2 meter at most, the transmittance can thus be regarded to be 1. This will be shown in Sec. 6.3.2.

Togawa reports human skin emissivity of $\epsilon = 0.971 \pm 0.005$ at $1\mu\text{m} < \lambda \leq 14\mu\text{m}$ [90], whereas Steketee reports an emissivity for this same range of $\epsilon = 0.98 \pm 0.01$ [91]. Moreover, they report that the emissivity for burnt, white, and black skin is the same, both *in vivo* and *in vitro*.

3.2. IR Cameras

Normal cameras capture light with a wavelengths in the visible spectrum, i.e. from 0.4 μm to 0.75 μm , as can be seen in Fig. 3.1. However, humans emit radiation with wavelengths in the range of 4 μm to 30 μm , with a peak intensity at 9 μm [89]. As mentioned in Sec. 3.1, two spectral “windows” exists that absorb less IR radiation. Radiation from the human body falls in the LWIR band and slightly in the far-IR band, but due to the window only existing from 8-14 μm , a camera in this range will be sought. This leaves a large part of the spectral range in which humans emit radiation uncovered, however only very specialized space-based systems that require intensive cooling or special short range imagers function in this part of the spectrum and will thus be more expensive [92] and are not considered as an option. Digital cameras often are made up of an active pixel sensor (CMOS sensor) or a charge-coupled-device (CCD), where the latter consists out of silicon, and are transparent past wavelengths of 1000nm [98]. In common use these digital cameras do not display IR because a filter is placed in the camera. Removing this filter would have been an option, had CCDs been sensitive to LWIR.

3.2.1. Bolometer

Many such, if not all, thermal cameras function using a staring focal plane array (IRFPA), which uses an array of light sensing, or in the case of IR, IR sensing pixels at the focal plane of a lens. Where a CCD transforms electromagnetic radiation into charge, an FPA can transform electromagnetic radiation, IR in this case, into resistance at each pixel. When radiation falls onto a pixel, the photon energy is converted to heat, which then changes the resistance of the pixel's thin film resistor. A device that measures the power of incident electromagnetic radiation via the heating of a material with a temperature-dependent electrical resistance is also known as a bolometer. An often used detector type for uncooled FPAs is an uncooled vanadium oxide (VO_x) bolometer.

An example of an uncooled FPA pixel is shown in Fig. 3.4. Radiation falls on the thin film resistor/absorption layer. The legs provide connection between the readout IC and the thin film resistor/absorption layer, and suspend it. As radiation falls onto the absorption layer, the resistance value of the thin film resistor changes. This change in resistance is sampled and converted into a digital value. The readout IC also biases the thin film resistor and multiplexes all the pixels to the imaging electronics.

3.3. Measurement Errors

Thermography measurements through an incubator are subject to erroneous temperature values due to various external sources, e.g. an external heat source, background temperature, external convective air flow, the

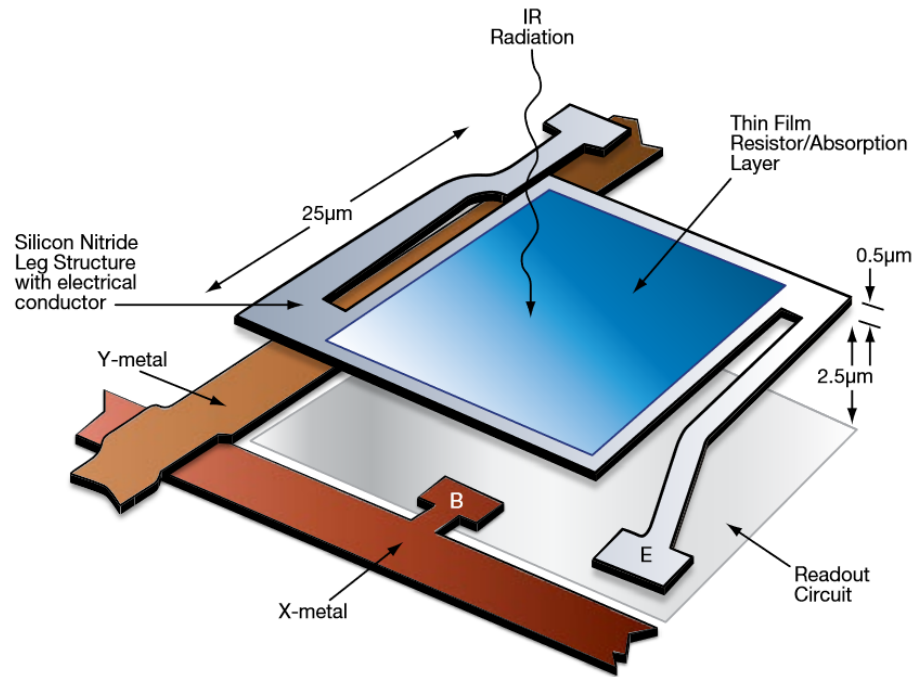


Figure 3.4: An uncooled FPA pixel. Image taken from [6].

Noise	Description	Source
σ_{tvh}	Random Spatio-Temporal Noise	Detector Temporal Noise
σ_{tv}	Temporal Row Noise, Line Bounce	Line Processing, $1/f$, readout
σ_{th}	Temporal Column Noise, Column Bounce	Scan Effects
σ_{vh}	Random Spatial Noise, Bi-Directional Fixed Pattern Noise	Pixel Processing, Detector-to-Detector Non-Uniformity, $1/f$
σ_v	Fixed Row Noise, Line-to-Line Non-Uniformity	Detector-to-Detector Non-Uniformity
σ_{vh}	Fixed Column Noise, Column-to-Column Non-Uniformity	Scan Effects, Detector-to-Detector Non-Uniformity
σ_t	Frame-to-Frame Noise, Frame Bounce	Frame Processing
S	Mean of All Noise Components	

Table 3.1: Three dimensional noise components [64].

material the measurement is made through, and different emissivity from the object [85]. Abbas et al. developed an error correcting method based on the skin temperature from preterm neonates as seen through an IR transparent window in the incubator, and when the baby was held close to the mother in so called “kangaroo mother care”. They developed a mathematical model for all heat fluxes in play, e.g. the heat flux emitted by the neonate, the reflections upon it, and ambient heat flux. They neglect the heat flux emitted by optical components and camera filters. A comparison between the neonates temperature, measured with a reference sensor, and the measured thermographic temperature after correcting for the determined heat fluxes, showed a temperature difference of 0.6°C [85]. Within the covered area of one pixel, small temperature deviations might occur. However, these small deviations are considered negligible and the total surface area measured by one pixel is considered to be an averaged constant [87]. This can of course yield some errors. Eq. (3.6) describes the error of a thermography measurement.

$$\Delta T_{Object} = T_C - T_R \quad (3.6)$$

T_C is the measured and calculated temperature by the camera of a single pixel, with T_R being the actual temperature on the object's surface. Not only is ΔT dependent on T_C and T_R , it also depends on the radiation coefficient ϵ_0 , the ambient (background) temperature T_a , and the angle ϕ of the camera with respect to the normal of the object's surface [86].

3.3.1. Microbolometer Noise

As described in Sec. 3.2.1 a device that transforms electromagnetic radiation into a change in electrical resistance is called a bolometer. A bolometer that uses an FPA array that is very small is called a microbolometer. Essentially such a FPA array consists of an array of tiny resistors. Because of the micro scale of such a device, variations occur in how a pixel responds to infrared energy from an object. All these different responses from all these pixels and their DC output have to be zeroed out. This is done by periodically placing an internal flag or iris in front of the detector as a constant temperature reference and is called a Non-Uniformity Correction (NUC) [6]. The analog signal from the resistor which is sent to be sampled, contains noise, as all analog signals contain noise. As this signal is amplified, the noise becomes visible, which is commonly referred to as "snow". The signal level of this noise is referred to as Noise Equivalent Temperature Difference (NETD). Most LWIR FPA microbolometers IR cameras that are used currently have an accuracy of $\pm 2^\circ\text{C}$ or $\pm 2\%$ of reading, with an NETD of $< 0.05^\circ\text{C}$ at 30°C . The NETD is an electronic measure which depends only on the noise sources, the sensor circuitry, and the measuring point and circuitry [7]. Noise in a microbolometer system can come from three sources: the detector, the electronics (readout integrated circuit (ROIC) and imaging electronics), and other system sources. Noise from the bolometer detector system is currently the limiting factor in performance. Thermal noise, thermal fluctuation noise, and $1/f$ noise are the three major sources in uncooled VOx bolometer detectors [8].

3D Noise

An infrared camera can be specified by its 3D noise. By taking measurements of a blackbody over time, measurements as in Fig. 3.5 are made. Four different types of noise are present: pixel noise, row noise, column noise, and frame bounce. These can be determined by taking an average over each of the 7 possible directions from Fig. 3.5 by using the Cartesian coordinate system: $\vec{OP} = (p_h, p_v, p_t)$. For each direction that was not averaged, the standard deviation is calculated of all noise values. Each noise parameter describes a noise

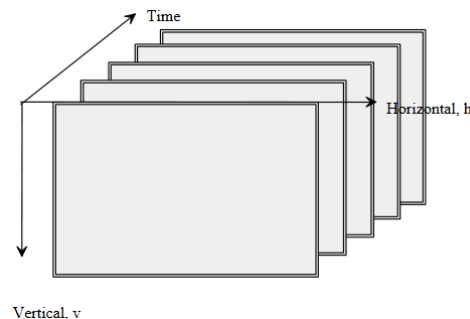


Figure 3.5: Three dimensional noise coordinates

source and can be seen in Table 3.1.

3.3.2. Calibration

Most modern cameras have an auto-calibration setting, but they generally require the emissivity to be set manually. All surfaces have an emissivity lower than 1, and as such will appear colder in thermographic measurements than they are in reality. By setting the emissivity correctly the camera can adjust for this. Emissivity of a material is however highly dependent on multiple chemical and physical properties and is often only estimated. By applying a high emissivity coating on the surface as reference, the real emissivity can be calculated [104].

3.3.3. Camera Angle Effect on Emissivity

Emissivity is also affected by the camera viewing angle of the camera. At angles deviating 15° , 30° , 45° , 60° , and 70° from the normal line, tests were performed, both on a conducting surface, and a non-conducting

surface. Angles deviating less than 45° from the normal show an approximately constant emissivity for the conducting surface, with a decrease at angles larger. The non-conducting surface was also approximately constant up until 45° , but increased in emissivity at angles larger than 45° . This was tested with a Tli400 (Fluke Corporation, USA) [99].

3.3.4. Condensation

A high relative humidity combined with a high temperature generates condensation on the inside of the incubator. The absorption coefficient of liquid water for IR in the range from 200nm to 200 μm is depicted in Fig. 3.6.

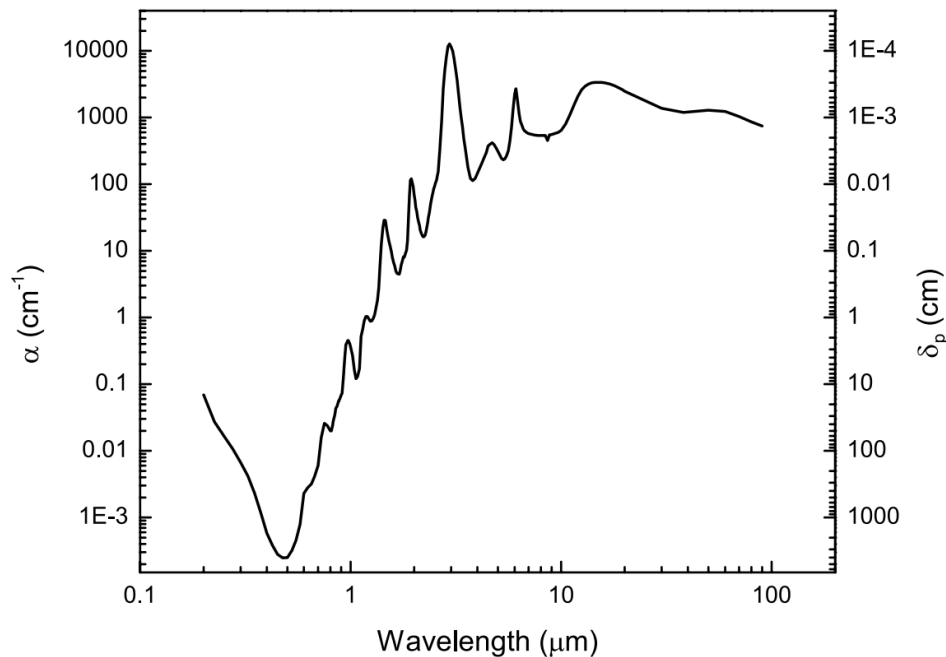


Figure 3.6: The absorption coefficient (α) of water for wavelengths ranging from 200nm to 100 μm at 298K on the left y-axis [134]. Penetration depth (δ_p) on the right y-axis ($\delta_p = \alpha^{-1}$). Original image taken from [135].

In the range from 390-750nm, i.e. the visible spectrum, absorption reaches 0.001cm^{-1} and penetration depths (δ_p) up to 1000m. At δ_p only $1/e$ of the surface power remains. The transmittance of water is much larger than 0 in this region. Sadly, in the IR region 750nm-100 μm the transmittance is close to 0. The absorption coefficient reaches values of 0.01 and 10^4cm^{-1} , which means that IR radiation is absorbed within 1m and 1 μm respectively of the water's surface [134]. For the range 7-15 μm IR will have been absorbed at depths of approximately 10 μm . Adsorption water films on glass has been found to be 0.1mm in thickness, whereas it has been found to be only 2 molecular layers on a clean gold surface near water vapor pressure levels. At 16mm pressure (89%RH) there is a strong adsorption which yields a layer with 3.0nm thickness [18]. However, in a study on droplet growths, it was found that droplets can form on a surface at 70% RH cooled to 15°C degrees with a range of radii from 15 μm to 25 μm [19].

3.3.5. Anti-Fog Coatings

Condensation is formed when water in a gaseous state comes into contact with a surface that is at a colder temperature. The gaseous water will try to transfer energy to the colder surface, which cools down the gaseous water and turns it into liquid droplets. Liquids scatter light which restricts its transmission. In situation where fogging of glasses or lenses cause hazardous situations, e.g. fire-fighter goggles, visual impairment should be prevented. As such, anti-fog coatings were developed. These coatings can differ in their methods of operation: they can be based on hydrophilicity or hydrophobicity. This property is expressed in the contact angle, i.e. the angle where a liquid-vapour interface meets a solid surface.

The difference between hydrophilicity and hydrophobicity based on their contact angle can be seen in Fig. 3.7. The smaller the angle, the more a given volume of liquid spread on a solid surface. This angle is also used to determine the wettability of a solid material by a liquid under static conditions [55].

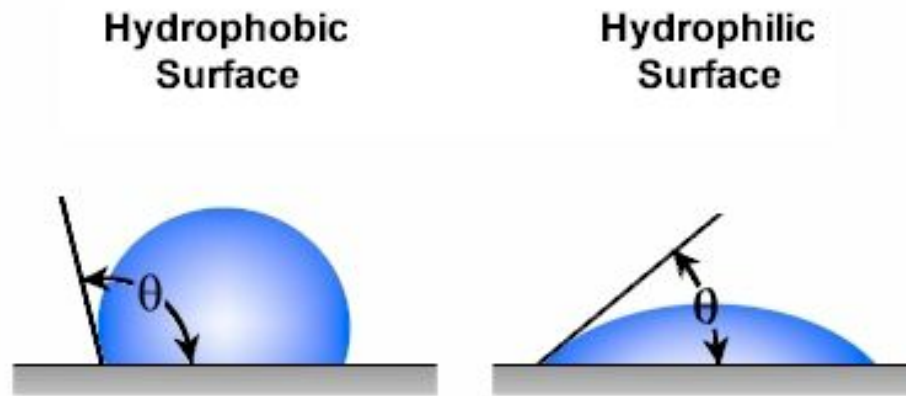


Figure 3.7: The contact angle θ is the angle where the liquid-vapor interface meets the solid interface. *Original image taken from [54].*

Hydrophilic Coatings

Hydrophilic coatings increase the surface energy of the surface it is applied on, which corresponds with a droplet contact angle $< 90^\circ$, and will promote the spreading of droplets. If the condensation has a low contact angle a continuous or near-continuous film is created, which reduces the scattering of light, and preserves its transmission [57]. Lowering the contact angle towards 0° yields superhydrophilicity. This is defined as $\theta < 5 - 10^\circ$ [56].

Hydrophobic Coatings

Hydrophobic coatings lower the surface energy of the surface it is applied on, but increase the droplet contact angle, and as such $\theta > 90^\circ$ for hydrophobic coatings. A high contact angle means separate droplets will form on the surface, through which light will scatter and fog will still cover the surface [57]. If the contact angle is raised to values $\theta > 150^\circ$, a surface has reached superhydrophobicity [56].

However, these coatings are often made of chemicals which have not been tested for their transmission in the LWIR spectrum. Moreover, these chemicals could very pose a health hazard. Applying such a coating will break the CE certification of the camera and possibly the incubator, and as such will not be considered a viable option for this research.

3.4. Gold-Standard Temperature Measurements

Measurement of neonate's temperature can be done either rectally or axillary. The gold standard for this remains mercury-in-glass thermometers. Digital thermometers offer a good alternative as mercury-in-glass takes some time to properly adjust to the correct temperature. For healthy neonates that can withstand an error of $\pm 0.2^\circ\text{C}$ digital thermometers can be used [103]. Measuring a neonates skin temperature in an incubator where the humidity and temperature are increased to keep the neonate's body temperature normal is done using skin electrodes. These are considered the gold standard for measuring skin temperature. They can determine skin temperature with an accuracy of $\pm 0.1^\circ\text{C}$ [52]. Air, and skin temperature servocontrol, and manual control were tested as methods to regulate the temperature inside an incubator. Skin temperature servocontrol was found to most accurately regulate the temperature in an incubator [102].

3.5. Incubators

Due to the neonates' lack of the complex mechanisms that adults utilize to remain warm and produce heat, it is crucial that they do not lose excessive heat, or are too warm. In order to guard them against hypothermia or hyperthermia, they are often placed in an incubator. An incubator is a transparent box that is able to control the environment inside and in which a (preterm) neonate will fit. Different manufacturers provide incubators. At the HagaZiekenhuis, location Juliana Kinderziekenhuis (JKZ) in The Hague, the Dräger Caleo[®] is the incubator of choice, whereas the Ohmeda Giraffe[™] Omnibed is used at the Reinier de Graaf Gasthuis (RDGG) in Delft. It has an air control mode, baby temperature control mode, powered vertical height adjustment as main features, and humidity control, and oxygen level control as optional features. Its dimensions are as follows [35],[36]:

	GE Giraffe™ Omnibed	Dräger Caleo®
Width x depth x height (min/max) [cm]	69 x 112 x 147/236	68.7 x 116.7 x 122/152

Table 3.2: Incubator dimensions.



(a) GE Giraffe™ Omnibed.



(b) Dräger Caleo®.

The environment is generally controlled by an AC-powered heater, a fan to circulate the air inside the incubator, servocontrol to control the air temperature, a water dispenser that is used to humidify the incubator, and a valve through which oxygen may be added. Convection is the main method incubators use to transfer heat to the neonate. A cooler air temperature than the skin of the neonate results in heat loss due to the velocity of the air flow. Modern incubators should not have an air flow velocity higher than 6 to 8 cubic decimeter per second (cds). This low air flow does reduce the ability to warm hypothermic neonates as quickly as possible [83]. Technical aspects of the incubator will be discussed in Sec. 3.5.1. Despite the advantage of being able to monitor and regulate the environment, an incubator has some disadvantages: they are expensive, both in purchase and in use, and a mother is not able to bond with and breastfeed her newborn as there is a barrier between them [62]. Moreover, heat is not distributed equally in incubators, which leaves hot, and cold spots. Incubators with an average temperature of $\geq 34^{\circ}\text{C}$ and relative humidity of $\geq 60\%$ were found to have elevated abundance levels of staphylococci in cold spots. Staphylococci are the main causative agents of late-onset sepsis in preterms [63].

3.5.1. Incubator Hood Material

The hood of an incubator is generally made out of polymethyl methacrylate (PMMA) (also known as acrylic), or polycarbonate (PC). Both have different physical and chemical properties which affect their emissivity, reflectivity, and transmissivity. Transmission properties of seven different kind of plastics in the range of $0.4\text{-}40\mu\text{m}$ were tested. Each sheet was 5.08mm thick. Among the materials tested were polysulfone, polymethyl pentene (TPX), polystyrene, PMMA, styrene-acrylic copolymer, nylon, and PC. They found similar properties for the range of $1.0\text{-}2.0\mu\text{m}$. They found that all materials, except TPX from $15\mu\text{m}$ to $40\mu\text{m}$, are completely opaque in the LWIR range [114].

Plexiglas is one of the trade names for PMMA and is often used as alternative to glass. Plexiglas thicker than 3mm is completely opaque at wavelengths from $2.8\mu\text{m}$ to $25\mu\text{m}$ [105].

3.5.2. Incubator Evaluation

Many of the features of the most commonly used incubators in The Netherlands (Dräger Caleo[®] and GE Giraffe[™] Omnibed) were professionally tested by the Medicines and Healthcare Products Regulatory Agency (MHRA) [136][137]. All tests are performed according to European Standard for Baby Incubators BS EN60601-2-19 (1997).

Temperature Response

The temperature response of both a single wall hood and a double walled hood were tested and can be seen in Table 3.3.

Setting	Single wall	Double wall
34°C 50%RH	33.7°C after 1 hour	18 min
36°C 70%RH	35.7°C after 1 hour	35.8°C after 1 hour
38°C 99%RH	51 min	41 min

Table 3.3: The temperature response of a Dräger Caleo[®] incubator. Single wall hoods could not quite reach the set temperature. Data from [136].

The display of the incubator for the single wall hood temperature measurements indicated 34°C after one hour, whereas in reality it had only reached 33.7°C.

The GE Giraffe[™] Omnibed was also tested for its temperature response. The results can be seen in Table 3.4.

Setting	Single wall
34°C 50%RH	32.5 min
36°C 70%RH	–
38°C 95%RH	50 minutes

Table 3.4: The temperature response of a GE Giraffe[™] Omnibed incubator. Data from [137].

For the Dräger Caleo[®] the average incubator temperature at the centre of the mattress was measured for over one hour at three different temperatures: 34, 36, 38°C and can be seen in Table 3.5.

Setting	Single wall	Double wall
34°C	33.6°C	34.1°C
36°C	35.7°C	35.9°C
38°C	37.9°C	37.9°C

Table 3.5: The average temperature measured over one hour of a Dräger Caleo[®] incubator. Data from [136].

The actual average temperature is slightly lower than the set temperature. During this hour, temperature variations no larger than $\pm 0.1^\circ\text{C}$ were measured, which is well within the $\pm 0.5^\circ\text{C}$ standard as set by Dräger[®].

Temperature Drop When Opening Portholes, Access Door, and Lifting the Canopy

Finally, tests were performed on how far the temperature and RH for the Dräger Caleo[®] would drop in different scenarios given a set temperature of 38°C and an RH of 99% with a double walled hood. For the GE Giraffe[™] Omnibed the temperature was set to 38°C and RH to 95% also using a double walled hood. The temperature and RH were given the chance to restore after each test.

The three situations were as follows:

1. All four hand ports were opened for 5 minutes.
2. One large access door on one of the sides was opened for 5 minutes.
3. The hood was removed for 5 minutes.

All three situations and according temperature and RH can be seen in Fig. 3.9.

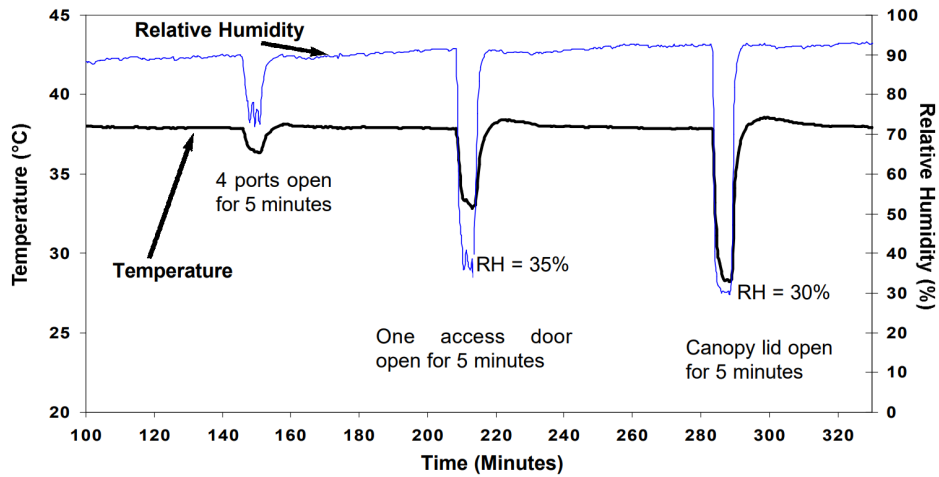
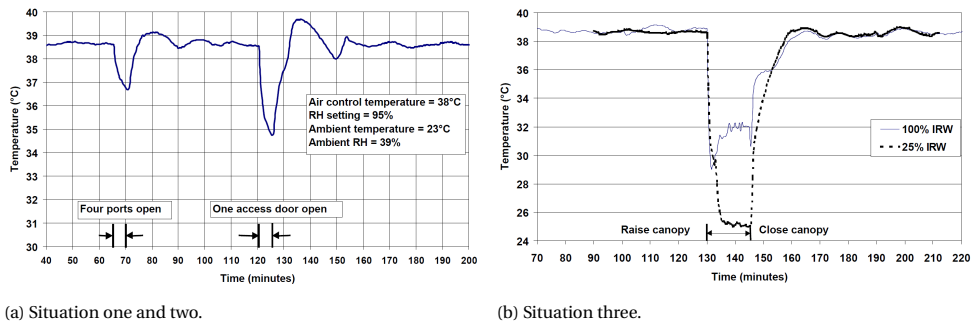


Figure 3.9: Temperature and RH displayed over time during all three different scenarios for the Dräger Caleo[®]. The blue line shows the RH. The black line shows the temperature. *Image taken from [136].*



(a) Situation one and two.

(b) Situation three.

Figure 3.10: Temperature displayed over time during situation one and two for the GE Giraffe[™] Omnibed. *Image taken from [137].*

Relative Humidity

In the range of 40% to 80% the RH was always within 5% of the set value. The maximum RH of 99% was never achieved, neither via independent measurements, or via the Dräger Caleo[®] display. The maximum was 96%. The measurements can be seen in Fig. 3.11.

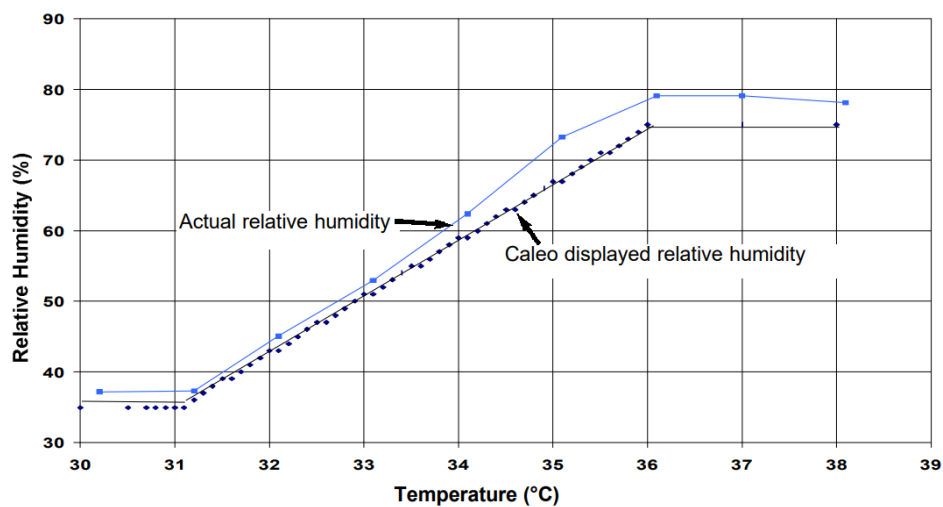


Figure 3.11: RH displayed over time. The blue line shows the actual RH as measured by independent measurements. The black line shows the RH as displayed by the Dräger Caleo[®]. *Image taken from [136].*

3.5.3. Polyethylene

Looking through the opaque plexiglas in the LWIR band is not possible. To be able to see inside the incubator, a side of the incubator could be replaced with polyethylene [85]. In Fig. 3.12 the transmittance and reflectance of a 0.1mm high-density PE (HDPE) foil can be seen. The absorption of HDPE is negligible at all wavelengths except at $3.4\mu\text{m}$, $6.8\mu\text{m}$, and $13.7\mu\text{m}$ [106]. Not only is PE better suited than plexiglas to observe preterm

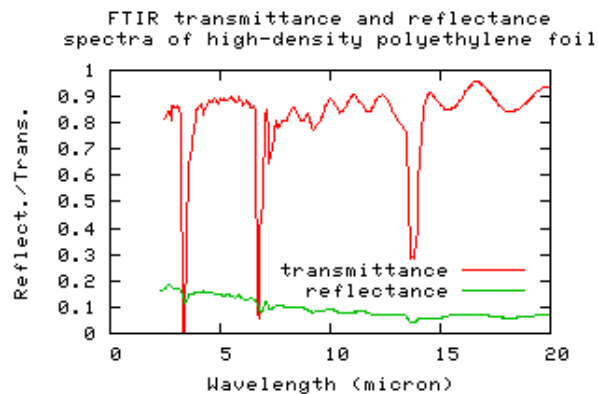


Figure 3.12: Transmittance and reflectance of a 0.1mm high-density PE foil. *Original image from [106], modified by [107]*

neonate radiation, it is also better at keeping a preterm neonate warm after birth. Rather than delay heat loss in very preterm neonates, occlusive PE skin wrapping prevented heat loss [108].

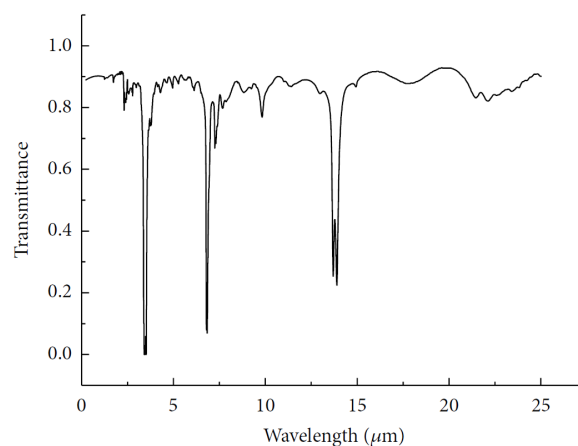


Figure 3.13: Transmissivity of a $30\mu\text{m}$ low-density PE foil. *Original image from [94]*

Suppose that the side of an incubator can not be replaced by PE foil, for instance because there are holes in the side through which nurses are able to reach the baby without having to lift the incubator hood. An alternative would be to replace the top of the incubator hood with PE foil. However, if this material were to protrude into the neutral thermal zone, it could disturb this environment.

3.6. IRT Research in Humans

Over the past decades, the possible use of IRT has been explored within several medical fields. Multiple studies have investigated the asymmetrical body temperature distributions which may indicate a number of diseases [78][79][80]. During an outbreak of Severe Acute Respiratory Syndrome (SARS) in 2003, IRT was put to use to mass-screen individuals [110][111]. However in a review of these kind of mass-screening at international airports, the risk of missing febrile individuals could reach 83% to 85% and that authors of the respective papers have said it could best be used as a proxy tool or that surveillance and contact tracing could be better suited [112]. Other topics in the medical field where the possibilities of IRT are being explored include diabetic neuropathy [116],[79], vascular disorder [78], [117], brain imaging [118], dentistry [119], [120], and

dermatology [121]. IRT has also been used in alternative medicine, e.g. acupuncture [122] and cryotherapy [124].

3.6.1. IRT Research in (Premature) Neonates

Unfortunately, IRT has barely touched the surface of its potential in neonates. Temperature distribution patterns in term neonates have been explored no earlier than 1980 [125]. In term neonates the skin temperature an hour after birth has been measured using IRT and compared to their core temperature [126]. Temperature distributions in the face have been studied during expressive behaviour in neonates. Neonates of 2-3 months, 4-6 months, and 8-10 months have been examined using IRT. During joyful expressions in neonates older than 4 months a decrease in skin temperature in the nose as much as 2°C degrees in 2 minutes was found [109]. Similarly breathing rate has been investigated using thermography, as an irregular respiratory frequency can be an early marker of physiological distress, and in diagnosing sudden neonate death syndrome. A region of interest (ROI) around the nose was defined, which was tracked during small head movements. Piezoplethysmography served as the gold standard. A mean error in breathing rate of 0.55 during small head movements was achieved [96].

Even less IRT research has been performed on premature neonates. Infrared thermographic calorimetry measurements have been performed on preterm neonates. In this study a specially designed incubator (Model C-86, Narco/Air Shields) was used to record IR. This incubator has a cutout with a polytetrafluoroethylene lid that could open and close. IR scanning periods only lasted for ~ 10 – 30s every 10 minutes for approximately 4 hours [127]. The relationship between body temperature in preterm neonates and necrotizing enterocolitis has also been studied. The premature neonates were placed inside a customized Dräger® incubator. A cutout was made in the top of the hood which was covered with saran wrap, which is a plastic made of polyethylene. The wrap however prevented the camera from focussing on the neonate. During the recording they removed the wrap and placed it back afterwards, with a plexiglas cover on top. Their recording periods lasted for ~ 5 minutes once a day during morning care. They tested using a datalogger whether a temperature drop occurred at the neonates location, and found it did not for those 5 minutes. [128].

Identifying Disease Based on Thermal Images

As of yet, a thermal image is made and then inspected by a trained professional, often as a confirmation of an infection or disease already diagnosed using different proven diagnostic tools. Such a thermal image can then be classified as a thermal image in which the patient was suffering from a certain infection or disease. Each infection or disease is identified by its own, hopefully, unique thermal image. All these thermal images would together create a database per infection/disease. Such a database can then be used to deduce early onset biomarkers which in turn can help prevent a disease.

3.7. Conclusion

IRT has been used on only a handful of occasions and even then only as exploratory diagnostic tool. Using IRT in combination with incubators comes with its own unique challenges. Humidity and camera angle have an effect on accuracy, whereas the hood of the incubator is opaque to LWIR. As such a measurement setup will have to be devised that circumvents the latter problem, and a model will have to be developed that accounts for the former problem. Subsequently software will have to be developed that implements the model.

Finally measurements on neonates have to be performed. Ideally, a database for each disease as described in Sec. 2.3 would be created of correctly classified IRT images of infections or diseases. Once such a database exists, strides can be made to manually predict infection. In this thesis a measurement setup will be chosen and described, a quantification will be researched that describes the interaction between IRT and an incubator, and IRT will be used to create images of neonates in incubators.

4

Image Processing

This chapter will provide a literature study on image processing. First several methods to reduce noise in images will be discussed and lastly artificial intelligence (AI), and how a branch of AI, deep learning, has been used with medical images.

As described in Section 3.3, most cameras have a certain sensitivity and accuracy. Generally subjects have a temperature several degrees kelvin hotter than their environment. However, when the environment has a temperature similar to the subject, this accuracy could become troublesome. Moreover, when a target is recorded over a long distance, environmental conditions can influence the temperature via atmospheric loss. In addition to the different types of microbolometer noise as described in Sec. 3.3.1, different types of image noise are also always present, e.g. impulse noise, Gaussian noise. Different methods have been developed and implemented to compensate for different noise types. This chapter will discuss a number of denoising methods often implemented in images.

4.1. Moving Average

For time domain encoded signals, the moving average is the most common and simplest filter. It is optimal for reducing random noise, while a sharp step response is retained. However the moving average filter is the worst possible filter for frequency encoded signals, as no band of frequencies can be separated [148].

Averaging over time can increase the spatial resolution, at the expense of a small degree of temporal resolution. This is often used in digital video images corrupted by random noise. The signal component is stable, whereas the noise component is additive uncorrelated zero mean noise, i.e. $g(x, y) = f(x, y) + n(x, y)$, with $g(x, y)$ being the noisy image, $f(x, y)$ the image without noise, and $n(x, y)$ is the noise. By adding these values per pixel and averaging them, the noise component should cancel out as can be seen in Eq. (4.1). Mathematically it can be shown that a moving average reduces the noise by a factor equal to the amount of frames the image was averaged over:

$$\text{Var}\left(\frac{1}{K}\sum_{i=1}^K g_i(x, y)\right) = \frac{1}{K^2}\text{Var}\left(\sum_{i=1}^K g_i(x, y)\right) = \frac{1}{K^2}\sum_{i=1}^K \text{Var}(g_i(x, y)) = \frac{1}{K^2}K\sigma^2 = \frac{1}{K}\sigma^2 \quad (4.1)$$

In Eq. (4.1) the average per pixel is taken over K frames, where each noisy image frame is denoted as $g_i(x, y)$. Then when the variance is taken over the averaged signal, it is clear that this removes the uncorrelated zero mean noise, and reduces noise power by a factor of K .

4.2. Median Filter

Median filters are particularly suited to reduce random noise and periodic patterns by smoothing the signal [145]. This filtering is done as follows: for any pixel, a window surrounding this pixel is constructed which consists of all surrounding pixels of the pixel under consideration. Such a window is said to have a size of 3x3, but different sizes are also used. The elements in this window are ordered and the median entry will replace the current pixel value value. The algorithm is finished when all pixels have been evaluated. An advantage of median filtering over average filtering is that no new values are created, rather taken from already existing

surrounding values, which should preserve edges. Hence the median filter is an edge preserving filter. Median filtering is especially useful against low levels of Gaussian noise, and “salt and pepper noise” [146]. However, small objects and details can be lost in median filtering. Therefore it is most often used in visual image processing, where the signal to noise ratio is higher than in thermal images [147]. To counteract this, it is most often used in conjunction with other filtering techniques, e.g. statistical test, edge detection kernel or boolean filter.

4.3. Wavelet Transform

The Fourier transform transforms a signal into a signal of possibly infinite series of sines and cosines. However, this comes at the cost of temporal resolution. For any given frequency in the Fourier transform it can not be known when in time it took place. This is due to Heisenberg’s uncertainty principle [149]. This means that a signal can not be represented as a point in time-frequency space. The wavelet transform aims to trade some temporal resolution for frequency resolution so that both simultaneously can be analysed. The idea is to cut a signal into separate parts, so that each part can be analysed separately. If the frequency at a certain time is of interest, taking a small window around this time using the Kronecker delta and transforming it to the frequency domain yields no solution. Wavelet analysis uses a fully scalable modulated window to solve this problem. The spectrum is calculated using this window and then the window is shifted. During each shift the duration of this window is either increased or decreased. This yields a set of time-frequency representations of the signal, each with a different resolution, also known as the wavelet coefficients [150].

The continuous wavelet transform (CWT) can be seen in Eq. (4.2). In theory, one should calculate the CWT for all values $-\infty \leq s \leq \infty \wedge -\infty \leq \tau \leq \infty \in \mathbb{R}$. This creates a three dimensional array, with on the x-axis all values of s , y-axis all values for τ , and z-axis, all values calculated by the CWT. These coefficients measure how closely correlated the wavelet is with each section of the signal. Due to the high computational cost of this calculation, in practice appropriate values for s and τ are used.

$$CWT_x^\psi(\tau, s) = \Psi_x^\psi(\tau, s) = \frac{1}{\sqrt{|s|}} \int x(t) \psi^* \left(\frac{t-\tau}{s} \right) dt \quad (4.2)$$

Several things can be made up from Eq. (4.2). $\psi(t)$ is called the “mother wavelet”, of which each other wavelets are derived, hence it can be considered a prototype wavelet. τ and s are called the translation and scale parameter respectively. The translation gives time information in the transform, i.e. it’s the location in time as the window is shifted. As frequency is reserved for the Fourier transform, scale s is used in the wavelet transform and is defined as $s = \frac{1}{f}$. A large scale gives a non-detailed global view of the signal, whereas a small scale gives detailed information [152]. Scaling is essentially compression in time, which is equivalent to shifting it upwards and stretching, i.e. $F\{f(at)\} = \frac{1}{a} F\left(\frac{\omega}{a}\right)$.

The CWT is too computationally expensive to calculate for continuous scale and translation and generates too much data. A solution to this is by choosing only a subset of scales and translation, often based on the power of two, which corresponds with the dyadic discrete wavelet transform (DWT). However, this leaves the spectrum uncovered from 0 to where the first wavelet covers the spectrum. By applying a low-pass spectrum this uncovered part of the spectrum is also covered. This function is called the “scaling function”, but is also referred to as the averaging filter.

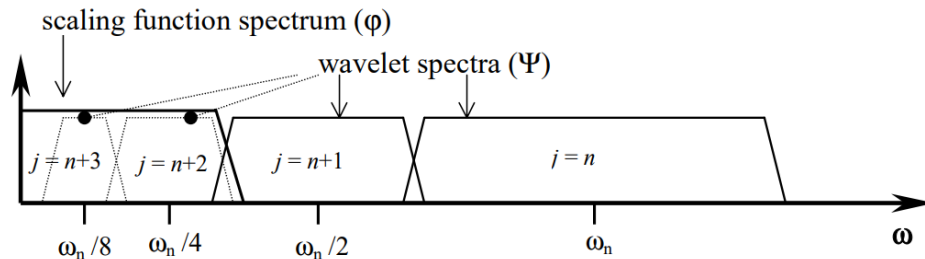


Figure 4.1: An infinite number of wavelets to a certain scale j would have been required to cover the entire spectrum, but by using the scaling function, a finite number of wavelets can be used. Image taken from [150].

This was first implemented using a “two channel subband coder” which yields the Fast Wavelet Transform [153]. This algorithm separates the high frequency and low frequency components, which are called the

details and approximations respectively.

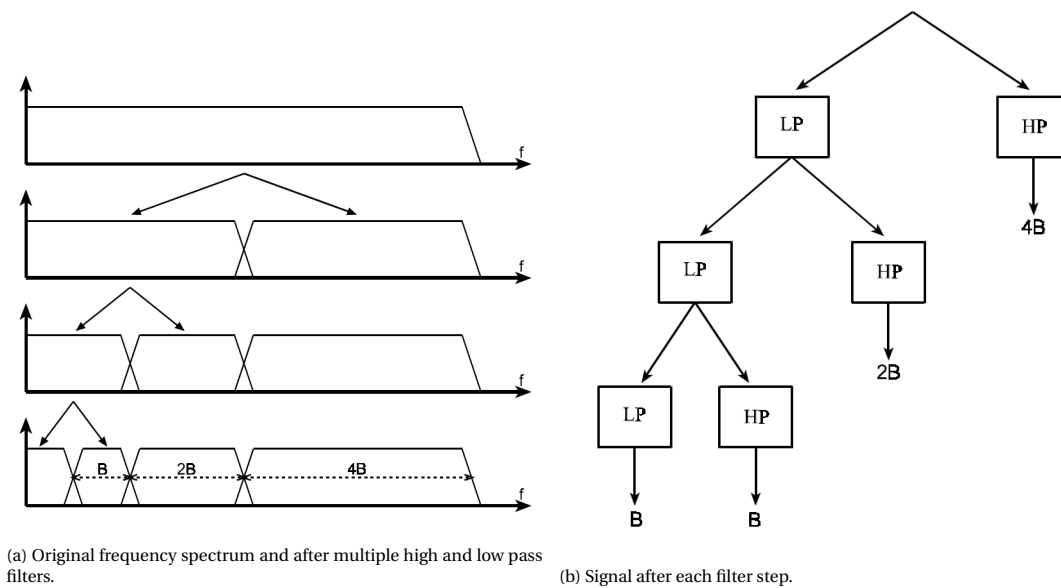


Figure 4.2: When the signal is low-pass (LP) and high-pass (HP) filtered, the signal spectrum is split in half. In the bottom left spectrum, the bandwidth of the signals are halved three times, i.e. 4 times smaller than the original signal only HP filtered once. Image taken from [150].

However, this produces twice the data than was originally started with. To correct this, both are down-sampled (or decimated) by two. By iterating this process over each newly acquired approximation, a wavelet decomposition tree (as seen in Fig. 4.2b) is created and many lower resolution components are created with corresponding wavelet coefficients. These filters combined are called an iterated filter bank.

Synthesis of the original signal constitutes of upsampling and filtering both the low and high frequency filtered signals and combining them. This is repeated until the original signal has been recovered. In order to reconstruct the original signal, correct filters have to be chosen based on quadrature mirror filter design. This design determines the shape of the wavelet. The wavelet chosen is entirely determined by the coefficients of the reconstruction filter. Wavelets must meet certain requirements and constraints which have not been discussed here. These constraints and requirements are the reason why so many different types of wavelets have been designed over the years. Examples of wavelet families include Haar, Daubechies, Cohen.

4.3.1. Denoising Image using Wavelet Transform

Everything discussed so far is considered in 1D. However, the DWT can also be applied on 2D data, for instance images. Suppose an image which has M rows by N columns. First the 1D DWT is performed in row direction, and is followed by the DWT in column direction. This creates one approximation (low frequency) and three detail (high frequency) subbands, named LL1, LH1, HL1, HH1 respectively. This can be seen in Fig. 4.3. Continuing this on the approximation subband LL1 yields four more subbands, namely LL2, LH2, HL2, and HH2. This is called the image decomposition of the second level, but can be repeated on LL2 and subsequent LL_n $n = 3, 4, \dots, \infty$ if computation power and time are of no concern.

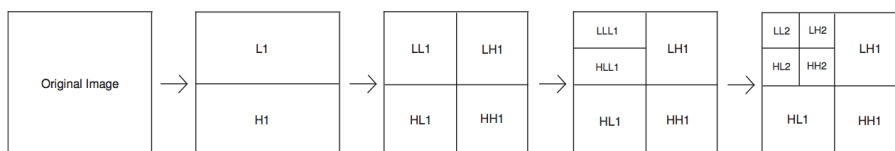


Figure 4.3: Image decomposition to the second level.

In [154] they use a Cohen-Daubechies-Feauveau 9/7 (CDF(9/7)) lifting scheme, which is a construction of

second generation wavelets (wavelets that are not based on one mother wavelet) [155]. First they add noise: Gaussian, Poisson, and impulse with three different levels of noise variance and density. Then they apply the lifting scheme up to 20 levels of decomposition. Yet three levels was found to be enough. In the next step the noise variance is determined using the median absolute deviation (MAD) as: $\sigma^2 = \left(\frac{MAD(|c_{i,j}|)}{0.6754}\right)^2$, with $c_{i,j}$ being the wavelet coefficient of the noisy image. They then calculate the VisuShrink threshold $Thr = \sigma\sqrt{2\log(N)}$, with N being the total number of pixels [156]. If the wavelet coefficients are larger than Thr they are unchanged, otherwise they are suppressed. Finally the denoised image is constructed by applying the inverse CDF 9/7 wavelet transform. They also denoise the original image by applying a 3x3 median filter, Gaussian filter, and Wiener filter. To validate their algorithm they compare the filter results with their algorithm based on MSE, PSNR, mean absolute error (MAE), mean structural similarity index (MSSIM), multiscale MSSIM (MSSSIM), feature similarity (FSIM), and Riesz-transform based FSIM (RFSIM). When noise with $\sigma = 0.2$ and density = 20% was added, the MSE decreased 83%; PSNR increased 98% and MSSIM increased 95%, MSSSIM enhanced 93%, FSIM grew 98.8%, RFSIM increased 83.4% with the same conditions in other methods.

4.4. Fuzzy Logic

Fuzzy logic is an extension of classic boolean logic and is based on fuzzy sets, which is a generalization of classical set theory. Fuzzy logic allows consideration of inaccuracies and uncertainties which also allows a condition to be something other than only true or false. The rules used in fuzzy logic are defined in natural language [157]. In classical set theory an element can either belong to a set, i.e. $3 \in \{2, 3, 4\} = 1$, or $5 \in \{2, 3, 4\} = 0$. In fuzzy logic, this membership, μ , can take a value ranging from 0 to 1, e.g. 0.8. Such a membership value corresponds with a membership function. For instance consider defining whether someone is tall. A sharp edged membership function for deciding whether someone is tall does not make sense. This is visually depicted in Fig. 4.4.

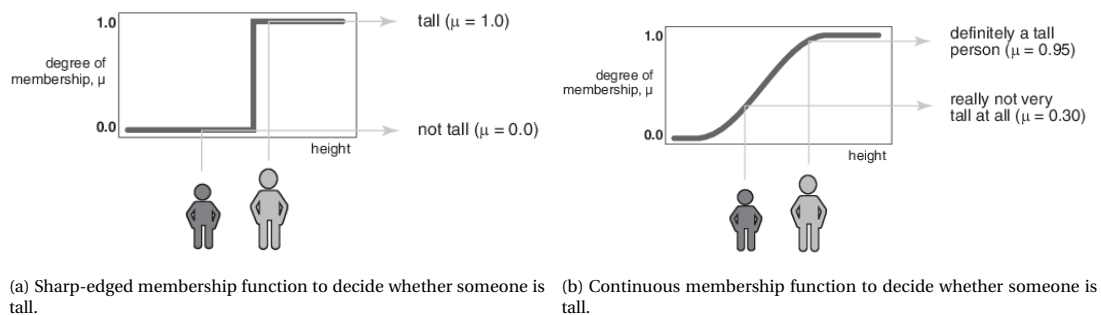


Figure 4.4: A sharp-edged membership function versus a continuous membership function. *Original image taken from [158].*

Similarly logical operations can be extended by fuzzy logic. Classical logical operations like AND, OR, NOT can be replaced by MIN, MAX, and (1-A) respectively. This does not change their truth tables, but does give rise to multivalued logic. This can be seen in Fig. 4.5.

This leads to fuzzy if-then rules, i.e. if x is A , then y is B , where A and B take linguistic values, e.g. if service is good, then tip is average [158].

4.4.1. Denoising Image using Fuzzy Logic

Multiple non-linear impulse noise removal approaches have been developed using fuzzy inference rule by else-action filter (FIRE) [159], the dual step FIRE (DS-FIRE) [160], and the piecewise linear FIRE (PWL-FIRE) [161]. They try to calculate positive and negative correction terms in order to express the degree of noise for a certain pixel. In [162] they propose a filtering method called Fuzzy Random Impulse Noise Reduction (FRINR). Their algorithm consists of two phases: detection and filtering. In the detection phase they define whether a pixel has been corrupted by impulse noise. First they look at the surrounding pixels or window of the pixel under consideration to determine whether the pixel under consideration is a noisy pixel, and then they use fuzzy gradients to determine the degree of impulse noise and the degree of it being a noise free pixel. They do this to create more robust noisy pixel detection. If both methods have determined a pixel to be noisy,

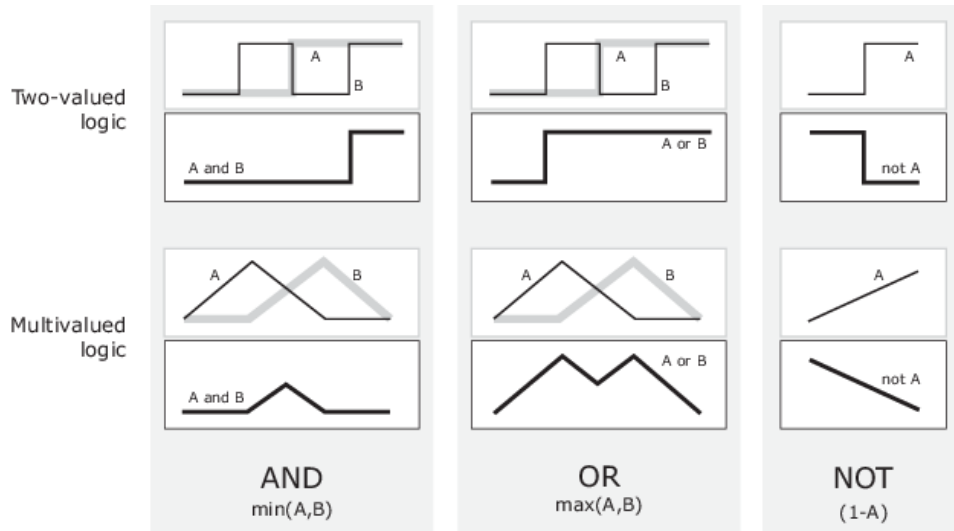


Figure 4.5: Classical logic graphs versus multivalued logic graphs. *Image taken from [158].*

they start the filtering process. For input pixel $A(i, j)$ the filtering method $F(i, j)$ is defined as follows:

$$F(i, j) = (1 - \lambda(i, j)) \frac{\sum_{k=-L}^L \sum_{l=-L}^L A(i+k, j+l) w(i+k, j+l)}{\sum_{k=-L}^L \sum_{l=-L}^L w(i+k, j+l)} \lambda(i, j) A(i, j) \quad (4.3)$$

As shown in Eq. (4.3) an area of $(2L+1) \times (2L+1)$ around pixel $A(i, j)$ is used. $w(i+k, j+l)$ is a weight indicating to which degree the pixel should be used, $\lambda(i+k, j+l)$ is used to control the amount of correction. They compare the PSNR of their algorithm with 22 other denoising algorithms that use fuzzy logic and outperform each for different noise densities. It should be noted that the only metric of performance they used was the PSNR which could give a skewed representation of the actual performance of their algorithm.

Similarly in [163] they first detect whether a pixel under consideration is a noisy pixel using the surrounding pixels. If a pixel is considered noisy, their fuzzy-based decision algorithm (FBDA) calculates the difference of each pixel in the surrounding pixels to the pixel under consideration. Then for each pixel in the window they calculate the membership value μ_s based on the maximum difference β . They call this the fuzzy set *small*. They then eliminate each pixel in the window if $T_1 < \mu_s < T_2$, with $T_1 \in [0, 0.05]$ and $T_2 \in [0.95, 1]$. They reason that when the central pixel is corrupted, it will hold either a very high or low value. So when the absolute difference between central pixel and neighboring pixels is computed, those pixels around the central pixel holding very high-intensity values or very low-intensity values (which may represent impulse noise) will have either very high or very low difference value. They compare the PSNR, structural similarity (SSIM), image enhancement factor (IEF) and image quality index (IQI) for different images and different noise densities. Their algorithm outperforms in each scenario.

4.5. Artificial Intelligence

Recently Stephen Hawking has warned humanity for Artificial Intelligence (AI). Hawking has said:

The development of full artificial intelligence could spell the end of the human race... It would take off on its own, and re-design itself at an ever-increasing rate. Humans, who are limited by slow biological evolution, couldn't compete and would be superseded.

(Stephen Hawking)

Even though this is far from reality, development in AI is ever increasing. What AI exactly entails has been discussed through the years, and multiple definitions have found its way into existence. Four major approaches include that AI must think humanly, think rationally, act humanly, or act rationally [164]. One example of AI is Waymo, formerly the Google self-driving car project. Where humans used to watch the environment to make decisions on how to control the car, this has been replaced by a plethora of sensors, both visible and invisible. Given enough data, this car can learn to recognize situations it may have seen before, and learn to understand new situations. This concept is based on probabilistic theory and is called machine learning.

4.5.1. Machine/Deep Learning

Whenever a data set is available in which people do not see the underlying trend, machine learning might offer a solution. By letting a computer “learn” from the given input, a computer may be able to determine features or outright the solution people would not have been able to find. It is essentially turning experience into knowledge. By offering a *training data* set, which represents this experience, the program outputs some form of expertise, which could be a label, or input to another program.

Another advantage of machine learning is its adaptivity. Once a program has been written, it will stay that way. However, input data can change per user. Machine learning takes its input and adapts itself to provide a wanted solution, thus overcoming a certain rigidity standard programs provide.

This learning can be divided into different types of learning, as the term learning itself is a very broad definition. There are two main methods to divide this in: supervised and unsupervised learning. Supervised learning is a way in which experience, or a label, is accompanied with the training data set, which is missing from the test data set. This data set can be defined as: $\{(\mathbf{x}_p, y_p)\}_{p=1}^P$, where \mathbf{x}_p are defined as input features taken from an arbitrary domain set \mathcal{X} , and y_p are taken from a label set \mathcal{Y} . The goal is to predict the corresponding labels for the test data set via a prediction rule: $h: \mathcal{X} \rightarrow \mathcal{Y}$. This function is also called a classifier. If these labels are not provided, and the goal is to find an underlying trend, or determine subclasses in a given dataset, this is called unsupervised learning [165]. Supervised learning lies at the essence of determining whether a neonate will develop an infection, however this would require labelling of neonates with an infection and neonates without. Paediatricians would be required to provide such a label after diagnoses. This seems not feasible, hence unsupervised learning would be the more preferred option.

Classifiers

Under the assumption that ill and healthy neonates will be labelled by a paediatrician, each neonate will possess a label. One method of classification for binary classification, i.e. two information classes, is by using support vector machines (SVM).

Support Vector Machine

SVMs separate the patterns of two classes by selecting a hyperplane such that $b + \mathbf{x}_p^T \mathbf{w} \approx y_p$, where b is a bias, and \mathbf{w} are *weights*, used to tune properly. The approximately equal sign is used, because it is not certain that all data is separated by a single line. If a two class dataset is linearly separable, there will be a hyperplane $b + \mathbf{x}_p^T \mathbf{w} = 0$ that passes between the two classes evenly. Given that there are no points on this hyperplane, a buffer zone can be created, a translated version of the hyperplane itself. If the two classes have a label of ± 1 , one translation will lie above the separator, such that $y_p = +1$, which gives $b + \mathbf{x}_p^T \mathbf{w} = 1$, and one below, such that $y_p = -1$, which would give $b + \mathbf{x}_p^T \mathbf{w} = -1$. The width of this buffer zone is called the margin and can be calculated to be $\frac{2}{\|\mathbf{w}\|_2}$, as can be seen in Fig. 4.6. Whether a hyperplane correctly classifies a point \mathbf{x}_p can be written as seen in Eq. (4.4).

$$\max\left(0, 1 - y_p \left(b + \mathbf{x}_p^T \mathbf{w}\right)\right), p = 1, \dots, P \quad (4.4)$$

If a point is correctly classified, Eq. (4.4) equals 0, but if it is wrongly classified, it will yield a positive value. Summing over the left part of Eq. (4.4) yields Eq. (4.5)

$$g(b, \mathbf{w}) = \sum_{p=1}^P \max\left(0, 1 - y_p \left(b + \mathbf{x}_p^T \mathbf{w}\right)\right) \quad (4.5)$$

and is also known as the *cost function*.

To find the separating hyperplane that has the minimum length of the normal vector and perfectly separates the data, Eq. (4.6) can be formulated as follows,

$$\begin{aligned} & \underset{b, \mathbf{w}}{\text{minimize}} \|\mathbf{w}\|_2^2 \\ & \text{subject to } \max\left(0, 1 - y_p \left(b + \mathbf{x}_p^T \mathbf{w}\right)\right) = 0, p = 1, \dots, P. \end{aligned} \quad (4.6)$$

Eq. (4.6) is also known as the hard-margin SVM, i.e. all data is perfectly separable. If on the other hand it is not known beforehand whether the given data can be perfectly separated, minimizing $\|\mathbf{w}\|_2^2$ for b, \mathbf{w} has no solution. This is why the hard-margin SVM is generally not used in practice. Adding $\|\mathbf{w}\|_2^2$ to the cost function with an added parameter $\lambda \geq 0$, relaxes the constraints as given in Eq. (4.5). The larger λ , the more

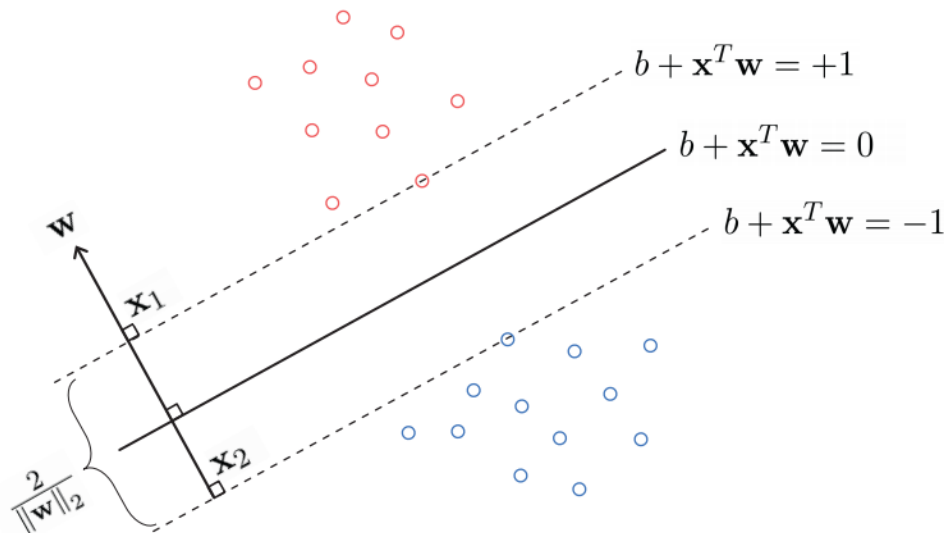


Figure 4.6: The margin of the hyperplane $b + \mathbf{x}_p^T \mathbf{w} = 0$ is the width of the buffer zone confined by two symmetric translation of itself, i.e. $b + \mathbf{x}_p^T \mathbf{w} \pm 1$. This margin can be calculated from two points of intersection of the normal vector \mathbf{w} , and two equidistant translations of the hyperplane, which is equal to $\frac{2}{\|\mathbf{w}\|_2}$. Picture taken from [167].

emphasis is placed on the hyperplane having a large margin. A small λ places pressure on satisfying the original constraints. This yields the soft margin SVM problem and can be written as seen in Eq. (4.7) [167].

$$\underset{b, \mathbf{w}}{\text{minimize}} \sum_{p=1}^P \max(0, 1 - y_p (b + \mathbf{x}_p^T \mathbf{w})) + \lambda \|\mathbf{w}\|_2^2. \quad (4.7)$$

k-Nearest Neighbors

Another method of classification is to use k-Nearest Neighbors (kNN). Opposed to an SVM, kNNs uses the data directly instead of building a model first. This leaves the only adjustable parameter, k , which represents the total number of neighbors the algorithm takes into account when deciding the class of a new point. It is calculated simply as the ratio of members of class y_p among the k nearest neighbors of \mathbf{x}_p .

An advantage of kNN is that it can provide an easy explanation for the classification result, whereas explanations provided by black-box models could prove to be inadequate.

The drawback is that some form of a metric has to be determined that measures the distance between data. Such a metric should include the relative importance of data, which is often unknown [166].

4.5.2. Deep Learning

An extension of machine learning is deep learning¹. At the basis are neural networks. Neural networks are based on how the human brain processes information. Each neuron has an activation a , and parameters $\Theta = \{\mathcal{W}, \mathcal{B}\}$ where \mathcal{W} is a set of weights and \mathcal{B} a set of biases, and is linked to other neurons. This activation is defined by a linear combination of \mathbf{x} and the weights followed by an element-wise non-linear transfer function σ . This can be expressed as $a = \sigma(\mathbf{w}^T \mathbf{x} + b)$. Often used transfer functions include the sigmoid and hyperbolic tangent function. However, in recent years the rectified linear unit $f(x) = \max(0, x)$ (ReLU) is used more often than the sigmoid and hyperbolic tangent function as it increases learning speed and classification performance [169]. If such a neuron is stacked and connected to another neuron, a network is created, aptly named multi-layered perceptron. This can be expressed as seen in Eq. (4.8).

$$f(\mathbf{x}; \Theta) = \sigma(\mathbf{W}^L \sigma(\mathbf{W}^{L-1} \dots \sigma(\mathbf{W}^0 \mathbf{x} + b^0) + b^{L-1}) + b^L) \quad (4.8)$$

\mathbf{W}^n is a matrix filled with rows \mathbf{w}_k associated with activation k in the output. n is the current layer, with L being the final layer. If additional layers are added in between input and output, these are often considered

¹Section 4.5.2 is based on [168]

“hidden layers”, and the network is considered deep, hence the name deep learning. When the activations of the final layer have been calculated, they are often mapped to a distribution over classes $P(y|\mathbf{x}, \mathbf{w}, b)$ using a softmax function as in Eq. (4.9).

$$P(y|\mathbf{x}; \Theta) = \text{softmax}(\mathbf{x}; \Theta) = \frac{e^{(\mathbf{w}_i^L)\mathbf{x} + b_i^L}}{\sum_{k=1}^K e^{(\mathbf{w}_k^L)\mathbf{x} + b_k^L}} \quad (4.9)$$

where \mathbf{w}_i^L is the weight vector leading to the output node associated with class i .

Convolutional Neural Networks (CNNs)

Currently the most popular deep learning network is the CNN. As the name would suggest, CNNs perform convolutions and are best used in imaging applications. At each layer the input image is convolved with a set of K kernels $\mathcal{W} = \{\mathbf{W}_1, \mathbf{W}_2, \dots, \mathbf{W}_K\}$ and biases $\mathcal{B} = \{b_1, b_2, \dots, b_K\}$, which each generate a new feature map \mathbf{X}_k . As with MLPs, the convolved feature map is subjected to a non-linear transform σ , formally noted as seen in Eq. (4.10).

$$\mathbf{X}_k^l = \sigma(\mathbf{W}_k^{l-1} * \mathbf{X}^{l-1} + b_k^{l-1}) \quad (4.10)$$

If more than one hidden layer is present in the network, it is considered a “deep” CNN. Two major differences between MLPs and CNNs exist. Firstly, CNNs share weights through layers. This means that later layers do not have to learn to detect objects already known in previous layers. Secondly, CNNs generally use pooling layers, which aggregates neighbourhood pixels, usually performed by a max, or mean operator.

Recurrent Neural Networks (RNNs)

RNNs were developed originally for discrete sequence analysis. They can best be compared to MLPs as both input and output can be of varying length, which makes them extremely suitable for translation tasks. For classification RNNs learn a distribution of classes $P(y|\mathbf{x}_1, \mathbf{x}_2, \dots, \mathbf{x}_T; \Theta)$ given a sequence instead of a single input vector. RNNs utilize a hidden state \mathbf{h} at time t as seen in Eq. (4.11).

$$\mathbf{h}_t = \sigma(\mathbf{W}\mathbf{x})_t + \mathbf{R}\mathbf{h}_{t-1} + \mathbf{b} \quad (4.11)$$

\mathbf{W} and \mathbf{R} are shared over time. For classification, often fully connected layers are added with a softmax at the end: $P(y|\mathbf{x}_1, \mathbf{x}_2, \dots, \mathbf{x}_T; \Theta) = \text{softmax}(\mathbf{h}_T; \mathbf{W}_{out}, \mathbf{b}_{out})$

Segmentation Architectures

Segmentation is a task often performed in medical images, used to distinguish the pixels of organs or lesions from tissue not under inspection, for instance, CT or MRI images, to deliver critical information about the shapes and volumes of these organs. CNNs can be manipulated to perform this efficiently. Without any manipulation, the sliding window will classify each pixel individually. This means that many convolutions are calculated multiple times. Due to the dot product and convolution being linear operations, the inner products can be written as convolutions and vice versa. This allows fully connected layers to be rewritten in convolutions and a likelihood map, instead of an output for a single pixel, can be produced from images larger than it was trained on. This is called the “fully convolutional network (fCNN)”.

Auto-encoders (AEs)

The neural networks discussed so far are used in supervised learning scenarios. As mentioned earlier, this is often not a practical solution. This section will describe an unsupervised learning architecture.

AEs learn how to efficiently compress and encode data to subsequently learn how to reconstruct the data back from the reduced encoded representation to a representation that is as close to the original input as possible. They do this by reducing the data dimensions through learning how to ignore noise in said data. They can, among other things, be used for anomaly detection, image denoising, and dimensionality reduction.

AEs are provided an input \mathbf{x} and reconstruct an output \mathbf{x}' through merely one hidden layer \mathbf{h} . The computation of \mathbf{h} can be seen in Eq. (4.12).

$$\mathbf{h} = \sigma(\mathbf{W}_{x,h}\mathbf{x} + \mathbf{b}_{x,h}) \quad (4.12)$$

From input to the hidden state weight matrix $\mathbf{W}_{x,h}$ and bias $\mathbf{b}_{x,h}$ are used, whereas from the hidden state to the output $\mathbf{W}'_{x,h}$ and bias $\mathbf{b}'_{x,h}$ are used. The idea behind AEs is that the dimension of $|\mathbf{h}|$ is smaller than the dimension of $|\mathbf{x}|$ such that latent dominant structures in the input can be discovered.

4.5.3. Classification using Deep Learning

Medical classification problems generally provide smaller datasets than for instance in computer vision. The goal is to detect a diagnostic variable as output (i.e. has an infection or not). An option to circumvent the problem of not having enough data is to use a network that has already been trained by others. This is called “transfer learning”. Such a network often requires some fine-tuning. The use of pre-trained CNNs with appropriate fine-tuning outperform CNNs that have to be trained from scratch [171].

In [172] a customized CNN network was developed to classify lung image patches with interstitial lung disease into five classes. Their first layer consisted of a CNN with a 7×7 kernel size and 16 output channels. The second layer was a 2×2 max pooling layer, followed by three fully connected layers with 100-50-5 neurons in each successive layer. In these fully connected layers they applied the dropout algorithm. This randomly disables half of the neurons during training, to improve performance [170]. The customized CNN network outperformed three different feature extraction networks that used SVMs. It must be noted that they have not compared their network against other networks that used customized features designed specifically for the interstitial lung disease images, and that their network did not use SVMs, hence the comparison could be skewed.

Instead of using CNNs, a regular deep NN was used in [173] to classify four classes of brain tumor. First they segmented the image using fuzzy C-means, and then extracted features using the DWT and principal component analysis (PCA). Their network consisted of a 7-fold cross validation building technique for building and training the 7-hidden layer structure. Their network performance was measured in terms of average classification rate, average recall, average precision, average F-Measure and average area under the ROC curve (AUC) of all the four classes and outperformed four other classifiers (kNN(k=1), kNN(k=3), linear discriminant analysis (LDA), sequential minimal optimization (SMO)) in all measures.

4.6. Conclusion

Methods to reduce noise in images have been described. A moving average filter can be used to reduce noise in time domain encoded signals, and is the simplest filter. When a scene is moving, blur is introduced. The median filter works well on salt and pepper noise, but small objects can be lost, and is therefore often used in visual image processing, rather than in thermal images. An elaborate explanation of the wavelet transform followed, and how the wavelet transform can aid in reducing noise. Several studies were listed with their results to support this. This section concluded with another method to reduce noise in images, along with several studies and their results, namely fuzzy logic. This chapter then concluded with an introduction to a branch of artificial intelligence, namely machine-, and deep learning. A look under the hood into classifiers was given by discussing SVM and k-NN. Then deep learning was explored more thoroughly. Several implementations, e.g. CNNs, RNNs, and AEs were discussed and their results in classifying medical images.

5

System Design

This chapter will describe several aspects of the system that is to be implemented. Firstly a high-level block diagram of the system is given. Secondly requirements for this system will be given. Then subsequently all blocks that are visible in the block diagram will be elaborated upon individually.

After a thorough literature study, an actual practical implementation will be developed. This system is meant to be used in hospitals, but should not clutter the room, hence an additional laptop per room and many wires treading through the room is not an option. This means a small embedded system will be the brain of the system. It will have tasks that consist of acquiring data from the IRT camera, running algorithms on this data, and communicating with the server and mobile app. At the heart of it all are the thermograms. The system in question will therefore consist out of three modules:

- A measurement module.
- A back-end module.
- A front-end module.

A block diagram of this system can be seen in Fig. 5.1.

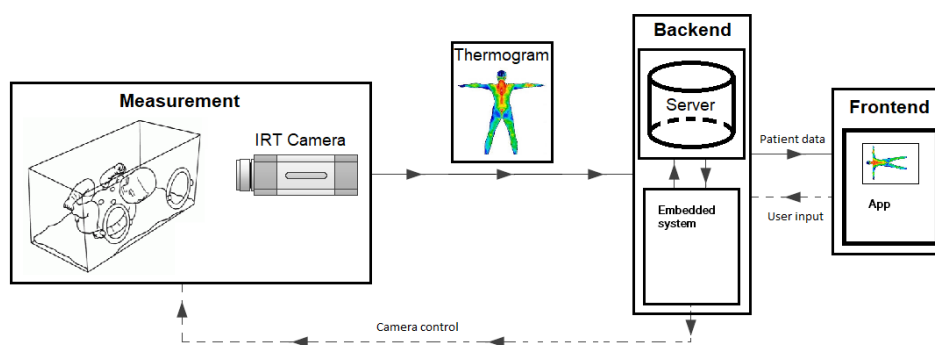


Figure 5.1: System block diagram.

The development of the mobile app of the front-end module and the server from the back-end module are not within the scope of this thesis. Software will be written that will have to run on the embedded system of the back-end module. This embedded system runs *Lubuntu 18.04.02 LTS* [129]. The server is run using *InfluxDB* [130], as designed by [151].

From Fig. 5.1 we can see that thermograms and the back-end are at the center of the system. The measurement module produces a thermogram that is sent to the back-end module, the embedded system then runs the written software (e.g. prediction algorithm, communication between server and/or front-end), and finally the front-end module displays the selected patient data on the mobile app. From the front-end module

runs an arrow back to the embedded system, as user input (e.g. nurse/pediatrician) determines the behavior of the embedded system with the server and measurement module. Similarly an arrow runs from the back-end module to the measurement module. This is due to the fact that user can choose certain settings that could affect the camera. Such a camera command by the user has to be sent to the back-end module so that it can be translated into a command that the camera actually understands.

5.1. Minimum System Requirements

The requirements that have been set up have been done so for the measurement module and the embedded system software. The other modules will not be developed in this thesis.

- The system must be cheap such that hospitals in less endowed countries can also use this system, preferably < 1000€. However, capability is more important than affordability.
- The system must be mobile, i.e. easily transportable and easy to set up.
- Data acquisition should *not* be through an app or program from the brand of the camera. Data must be accessible without it being modified/encrypted before access.
- The framerate, or frames-per-second (fps), must be such that any changes in the human body can be noticed.
- The camera must have a resolution such that changes in the human body can be noticed.
- The camera must have a sensitivity such that small changes can be noticed.
- The system should be simple. Hospital staff should be able to use and understand it without needing elaborate instructions.
- The system should operate in real time, such that hospital staff can intervene at the moment an event is occurring.
- The system must be safe and pose no harm to the patient and must not disturb other vital hospital equipment.

5.2. Measurement Module

The measurement module consists of the neonate to be recorded, and the IRT camera. This module produces thermograms, i.e. the data with which the back-end module will be working.

Having discussed multiple possible measurement errors, a measurement setup has to be decided upon that will be able to minimise, or preferably even completely render a measurement error source null. All possible setups require an opening to be created in the hood of the incubator, as plexiglas does not transmit any IR.

5.2.1. Placing the Camera in Front of an Open Porthole

The most simple and straightforward solution is to place the camera at a distance from the incubator in front of an open porthole of an incubator. This situation is depicted in Fig. 5.2. This creates two environments with each their own atmosphere.

This situation is advantageous for it needs no alterations to the incubator.

However, with this singular advantage come quite some disadvantages:

1. One valve of the incubator always needs to be open. This comes with two additional disadvantages:
 - (a) The neonate can fall out of the incubator.
 - (b) This creates an air flow for which the incubator will have to compensate. The effect on opening portholes has been elaborated in Sec. 3.5.2.
2. The camera will have to stand on a tripod in front of the chosen porthole. The chosen porthole severely impacts the area of skin that is visible.

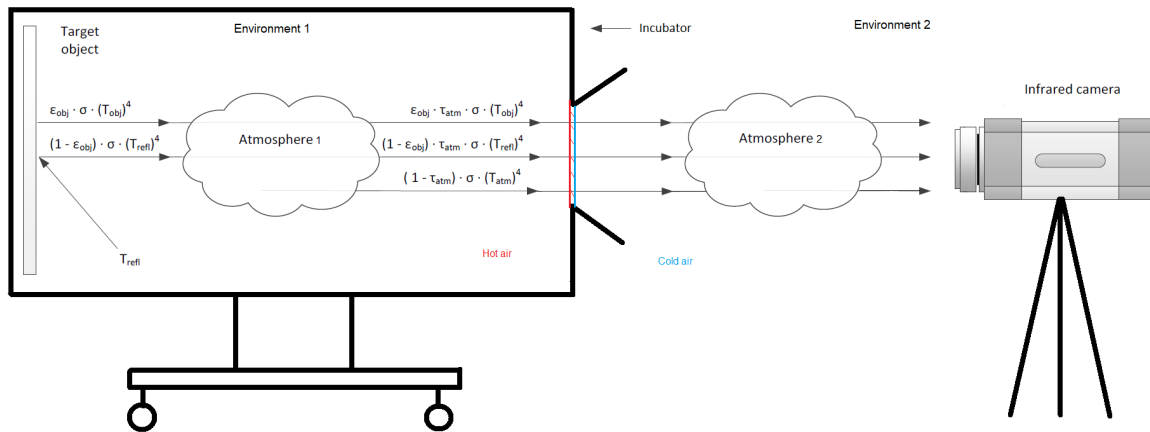


Figure 5.2: The situation in which an IRT camera would be placed in a tightly fit gap. *Original image taken from [139]*

3. Calculations of the radiation on the lens are quite complex. Cold air will flow into the incubator through the lower part of the open porthole, whereas warm air will flow out of the incubator from the upper part of the open porthole.

5.2.2. Placing the Camera in Front of an Open Porthole Sealed with IR Transmissive Material

Another possibility would be similar to the system described in Sec. 5.2.1, with the exception that some sort of LWIR transmissive material is used to seal the porthole, creating the situation as shown in Fig. 5.3. This creates two environments with each their own atmosphere.

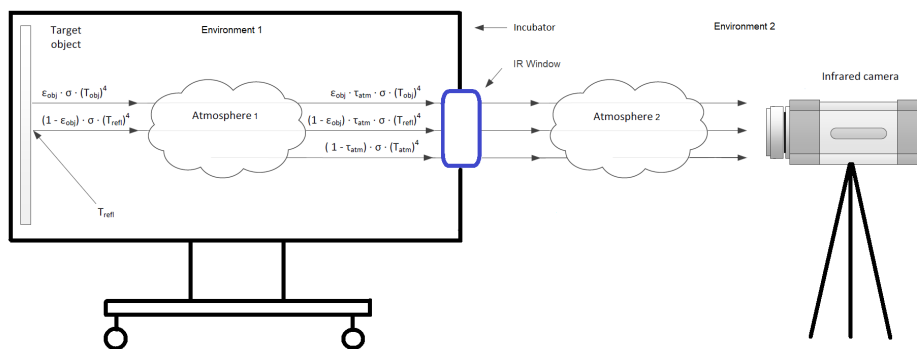


Figure 5.3: The situation in which an IRT camera would be placed above the hood of an incubator. *Image taken from [138]*

This setup has the advantages that:

1. The neonate will not be able to fall out.
2. It will minimize a temperature drop, as described in Sec. 3.5.2.
3. The camera is not in direct contact with the higher temperature and RH environment thus the lens will not be warmed, and no droplets will be formed on the lens which could influence measurements.
4. Radiation calculations are known.

However, a system is rarely ideal and will often have some drawbacks. This system is no exception:

1. Condensation can still form on the optical window in case of an increased RH, which will make focussing on the neonate difficult. Additionally, as described in Sec. 3.3, water absorbs IR radiation.

2. The camera will have to stand on a tripod in front of the chosen porthole. The chosen porthole severely impacts the area of skin that is visible.
3. Caretakers will have to perform an additional action: sealing the porthole.

Transmitted Radiant Flux

The total radiant flux can be calculated by summing all separate components. In this situation, six different components can be distinguished, under the assumption that an atmosphere does not reflect radiation and thus does not contribute another component.

1. The emitted radiation from the object (W_{obj}), through atmosphere one, through the window, and finally through atmosphere two.

$$W_{obj} = \epsilon \tau_1 \tau_w \tau_2 \sigma T_{obj}^4$$
2. The emitted radiation from the first environment reflecting on the object ($W_{refl,obj}$) through atmosphere one through the window, through atmosphere two.

$$W_{refl,obj} = (1 - \epsilon) \tau_1 \tau_w \tau_2 \sigma T_{refl,obj}^4$$
3. The emitted radiation from atmosphere one ($W_{atm,1}$) through the window, through atmosphere two.

$$W_{atm,1} = (1 - \tau_1) \tau_w \tau_2 \sigma T_{atm,1}^4$$
4. The emitted radiation from the window (W_w), through atmosphere two.

$$W_w = \epsilon_w \tau_2 \sigma T_w^4$$
5. The emitted radiation from the second environment reflecting on the window ($W_{refl,w}$) through atmosphere two.

$$W_{refl,w} = (1 - \epsilon_w) \tau_2 \sigma T_{refl,w}^4$$
6. The emitted radiation from atmosphere two ($W_{atm,2}$).

$$W_{atm,2} = (1 - \tau_2) \sigma T_{atm,2}^4$$

It is assumed that each atmosphere does not reflect radiation. The total radiation is all the components described above summed together, which yields Eq. (5.1).

$$W_{tot} = \epsilon \tau_1 \tau_w \tau_2 \sigma T_{obj}^4 + (1 - \epsilon) \tau_1 \tau_w \tau_2 \sigma T_{refl,obj}^4 + (1 - \tau_1) \tau_w \tau_2 \sigma T_{atm,1}^4 + \epsilon_w \tau_2 \sigma T_w^4 + (1 - \epsilon_w) \tau_2 \sigma T_{refl,w}^4 + (1 - \tau_2) \sigma T_{atm,2}^4 \quad (5.1)$$

5.2.3. Placing the Lens Inside a Tightly Fitting Gap

A final option would be to make a cut in the shape of the lens of the camera, so that the camera can be fitted tightly into created opening. Such a setup is depicted in Fig. 5.4.

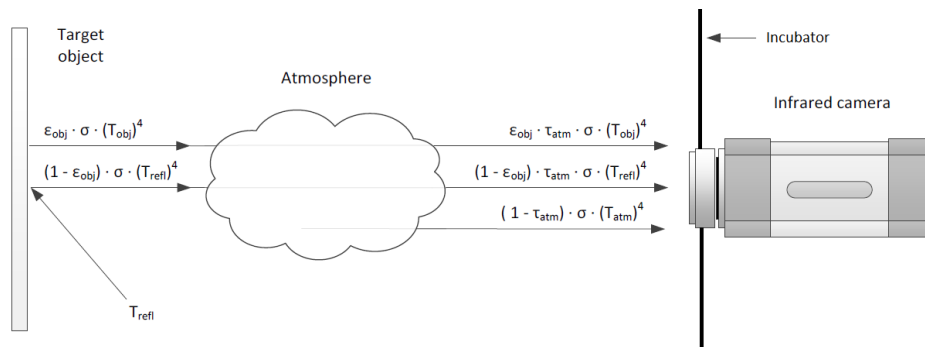


Figure 5.4: The situation in which an IRT camera would be placed in a tightly fit gap. *Image taken from [139]*

This method has a couple of advantages:

1. The TNE of the incubator would be disturbed as little as possible.

2. No foil has to be placed over the opening.

However, it once again has multiple disadvantages:

1. An opening has to be made in the material of the hood of the incubator. Once any adjustments are made to a tested and approved medical equipment/application, they have to be completely tested again. Additionally, the camera can then only be used on that location.
2. Droplets can form on the lens in case the RH is increased.
3. Due to the neonate now being closer, a lens could be required that has a FOV that can view the entire neonate.

Transmitted Radiant Flux

Calculation of the radiation entering the lens is relatively simple. These are the same as described in Eq. (3.5). Using similar subscripts as in Fig. 5.4, as follows:

$$W_{\text{tot}} = \epsilon_{\text{obj}} \tau_{\text{atm}} \sigma T_{\text{obj}}^4 + (1 - \epsilon_{\text{obj}}) \tau_{\text{atm}} \sigma T_{\text{refl}}^4 + (1 - \tau_{\text{atm}}) \sigma T_{\text{atm}}^4 \quad (5.2)$$

5.3. Back-end Module

The back-end module consists out of a server which is essentially data storage, and an embedded system which runs the data processing algorithms. The server is outside the scope of this thesis, however, certain design decision were made based on the communication with the server and will be elaborated in Sec. 7.

The embedded system is a microprocessor that runs *Lubuntu 18.04.02 LTS*. This system will process thermograms, manage communications with the server, front-end, and measurement module.

5.4. Front-end Module

The front-end module consists out of a mobile app that the user will use. This app will alert the user when certain events are triggered, e.g. a temperature sensor exceeds a certain limit value, or in case of thermograms, a suspected infection is found. The user also will have the ability to set certain variables, for instance what the limit for an alert should be, but the user will also be able to control the camera, e.g. use manual or autofocus. For this a Graphical User Interface (GUI) will be designed.

5.5. Conclusion

A number of (dis-)advantages have been discussed per measurement implementation. All that is left, is to choose a final implementation. The first described implementation is simply not an option, as it leaves an opening through which the neonate can fall. This adds a risk of injury through a fall. This will not be allowed by the hospital, but it also is not in accordance with the final system requirement.

The final implementation also leaves much to be desired, as drilling a hole in the hood of the incubator comes at a great cost, for the incubator will have to be tested again. Asking manufacturers to take this newly created system into account and create a new design of their incubator hood could be an option, but not one that is likely to succeed. Not only will manufacturers have to run rigorous tests again, the IRT camera can never be changed, as manufacturers would then have to go through the whole ordeal again.

This leaves the implementation described in Sec. 5.2.2. The camera will be placed in front of an open porthole that will be sealed with IR transmissive material. This setup prevents the neonate from falling out, will minimize temperature drop, will not warm the camera lens, and has known radiation calculations. However, condensation could form on the inside of the material which absorbs IR. Additionally it could be annoying for caretakers, as the camera tripod will be located somewhere in the camera, and one porthole will have to be manually sealed, and unavailable to enter the incubator.

6

Infrared Thermography Camera

In this chapter the IRT camera is the central topic. A selection of suitable IRT cameras for this project will be listed, based on the requirements given in Chapter 5. Then the camera will be analysed in depth, based on its internal parameters. A recreation of its internal model as developed by the manufacturer will be written using open-source software languages, and its result compared to the manufacturer's software.

In the search for the right IR camera, there are quite some consideration to take into account. What are the wavelengths in which the human, specifically neonates, emits radiation? From what distance will we be recording? What will the smallest anomaly or deviation be in size? And what is the smallest significant temperature deviation? Will we record from an angle, or from straight above? These are only a selection of the questions that will arise. This chapter will describe in detail the choices made in regards to equipment. Based on literature and given requirements and restraints an IRT camera was chosen.

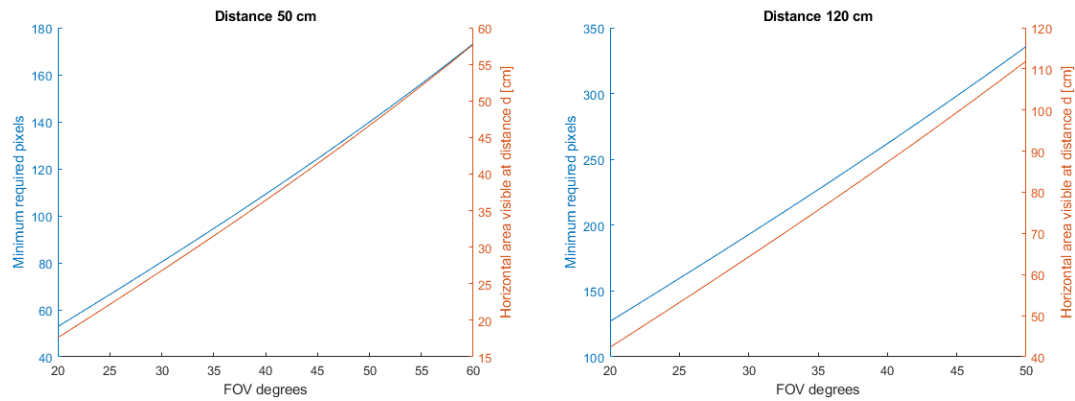
6.1. Selection

In order for a temperature deviation to be noticeable it should be measured by at least 3x3 pixels in the IRFPA [88]. Another variable to take into account is the Field-Of-View (FOV). This is specified in an angle, sometimes in a horizontal FOV (HFOV) and a vertical FOV (VFOV), but often it's just the HFOV that is given.

Suppose the distance from the camera to the baby in the incubator is considered to be 1.2m. The total visible area at 1.2m and with a HFOV of 32° is 68.8cm. Suppose a minimum size temperature deviation of 1cm² must be distinguished. The total amount of required pixels would thus be $3 \times 68.8^2 = 206.46^2$ which needs to be rounded up, so 207x207 pixels are required. Another option would be for the camera to be right on top of the hood of the incubator. Given the incubator dimensions in Sec. 3.5, a baby lies on a mattress in the baby compartment ~600mm from the top of the hood. A preterm baby is approximately 40cm tall, thus the camera would require such a HFOV that the visible area is at least 40cm, and preferably slightly more, should a neonate be taller. Assuming a distance of 50cm from the hood to the baby's body surface and a length of the baby of 50cm, the HFOV should at least be 52°.

In Fig. 6.1 two plots are visible at two different distances: $d = 50cm$, and $d = 120cm$ from the camera to the subject. The goal is always to distinguish a 1cm² anomaly and see the subject in its entirety. Assuming a tall baby of 55cm, it can be seen from Fig. 6.1a that at $d = 50cm$, a FOV of at least 58° is required, and a minimum amount of pixels to distinguish said anomaly would be 167x167. At $d = 120cm$ from Fig. 6.1b, to once again view 55cm of the subject, this would require a FOV of 27° and 167x167 pixels.

Affordability is a third soft requirement, i.e. preferably the IRT camera should be as inexpensive as possible, but capability to execute this project precedes affordability. Having decided upon a minimum resolution, and the spectral range, thermal cameras can be divided into three price-ranges: <1000€, 1000-10,000€, and >10,000€. The latter category contains military grade thermal cameras and are too expensive for the scope of this project. In the cheapest category are cameras with resolutions up to 320x240, that should be able to fulfil the requirements.



(a) At a distance $d = 50\text{ cm}$, the required minimum amount of pixels in one direction and the visible area are plotted against the FOV. (b) At a distance $d = 120\text{ cm}$, the required minimum amount of pixels in one direction and the visible area are plotted against the FOV.

Figure 6.1: Depending on the FOV and the distance to the subject, the minimum amount of pixels to distinguish an area of 1 cm^2 changes. Moreover, at a certain FOV and distance from the subject, the visible area is too small to see the entire subject. The minimum amount of pixels required to see an anomaly of 1 cm^2 is depicted on the left y-axis, the horizontal area which would be visible of the subject on the right y-axis, and the required FOV on the x-axis.





	Camera type	Resolution	NETD	FOV	FPS	Lifetime	SDK	Price
	Thermal Compact (Pro)	206x156 (320x240)	70mK	36° (32°)	<9Hz (>15Hz)	Uses 280mW. Based on 3000mAh phone battery, approximately 4 hours	No	\$249 (\$499)
	Thermal Imaging Reveal (Pro)	206x156 (320x240)	70mK	36° (32°)	<9Hz (>15Hz)	10 hours (4 hours)	No	\$399 (\$699)
	FLIR One Pro	160x120	70mK	55° x 43°	8.7Hz	45 min	Yes	478,80€
	FLIR SC305	320x240	50mK	25° x 18.8°	9Hz	Power outlet (12/24 VDC, 24 W absolute max)	Yes	8.229€

Table 6.1: Summary of potential IRT Cameras suitable for this project.

6.1.1. Seek Thermal

Seek Thermal has multiple types of IR cameras, the most notable being a USB camera that connects to a cellphone, e.g. an android or iPhone, sold as Thermal Compact, either basic edition, or pro. It uses the battery from the phone it is connected to. They also sell dedicated IR cameras which do not require a cellphone, known as the Thermal Imaging Reveal, also either basic or pro edition. Most important specifications can be seen in Table 6.1. Seek Thermal also sells thermal cameras dedicated to law enforcement, and firefighting. To use these cameras, the official Seek Thermal app/software is required.

6.1.2. FLIR

FLIR has also released an IRT camera that can be connected to a cellphone, be it android or iOS, via USB-C. Where the Thermal Compact uses the cellphone's battery, the FLIR One Pro comes with its own battery. For the FLIR One Pro an extensive SDK is available and they provide support for writing your own code to control the IRT camera.

6.1.3. Final Choice

Based on Table 6.1, the FLIR One Pro was chosen. Its resolution should suffice at distances smaller than 120cm, with a large enough FOV. Its FPS is slightly less than 9Hz, which should be more than sufficient. The price is well below 1000€, with a freely available SDK that can be used to create android applications.

FLIR A305sc

For this thesis however, the FLIR A305sc will be used. The Electronic Instrumentation department at the TU Delft has purchased this camera. It is available to us to use in this research. This model used to be the FLIR SC305, but has since been taken out of production and has been replaced and renamed to be the A3XX(sc) series, with the official name now being: FLIR A305sc. For this camera serial keys were purchased to use FLIR's software QuickPlot. IRT streams or snapshots created by this program create *.seq and *.img files respectively. This piece of software is elaborated on in Sec. 8.5.

The camera specifications can be seen in Fig. 6.2.

Imaging and optical data	
Field of view (FOV)	25° x 18.8°
Minimum focus distance	0.4 m (1.31ft.)
Focal Length	18 mm (0.7 in.)
Spatial resolution	1.36 mrad
Lens identification	Automatic
F-number	1.3
Thermal sensitivity / NETD	<0.05°C @ +30°C (+86°F) / 50 mK
Image frequency	9 Hz
Focus	Automatic or manual (built in motor)
Detector data	
Detector type	Focal Plane Array (FPA), uncooled microbolometer
Spectral range	7.5 - 13 μm
IR resolution	320 x 240 pixels
Detector pitch	25 μm
Detector time constant	Typical 12ms
Measurement	
Object temperature range	-20°C to +120°C 0 to +350°C
Accuracy	±2°C or ±2% of reading

Figure 6.2: Important specifications of the A305sc.

6.2. Noise Reduction

Every camera manufacturer performs some sort of image processing to create an even clearer image. FLIR is no exception. This is an option called *Noise Reduction*. This is something that should be disabled, so that an algorithm can be designed based on the raw output of the camera. This is preferred so that any algorithm that will be developed can work with any other camera that is based on an uncooled microbolometer. To further elaborate, when an existing noise reduction algorithm is in place, which is not used by a different IRT camera (manufacturer), any custom noise reduction algorithm that is based on the signal after this camera's noise reduction, will not yield the same result when used on a different camera's output that does not use this specific camera's noise reduction.

Disabling noise reduction is however not an option in the software we used to perform measurements: FLIR's own software, FLIR QuickPlot. This software will not be discussed in detail in this chapter, but in Sec. 8.5. The option for noise reduction was found after a trial period of a different version of FLIR's software, their premium model, namely *FLIR ResearchIR Max*.

After extensive email communication with FLIR's support desk, they sent test code in which the camera's parameters can be set. The GUI for this test code can be seen in Fig. 6.3. It is named *GEV DEMO* after

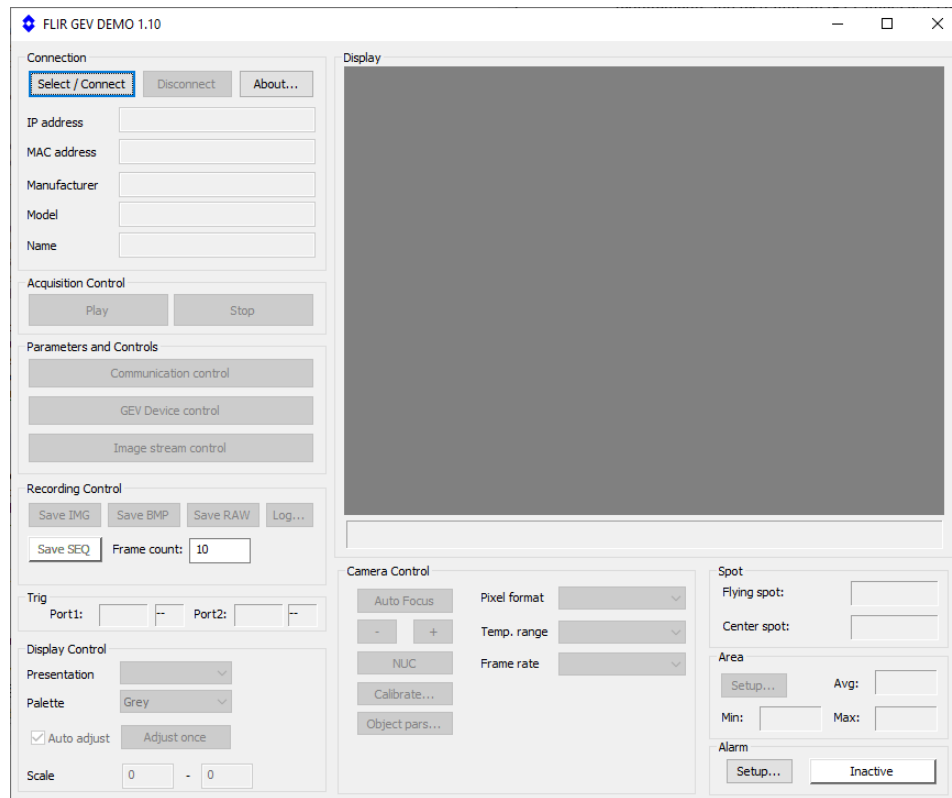


Figure 6.3: GEV Demo 1.10 received from FLIR support.

the protocol the camera runs on, namely *GigE Vision (GEV) Standard Compliant Protocol*. This program had multiple different options that software sold by FLIR does not possess. When a camera was connected it's parameters could be viewed/set and it could be controlled. This was done via the panel *Parameters and Control*. The option to enable/disable noise reduction was found under the *GEV Device Control* button. Noise reduction was re-enabled every time the camera had lost power and consequently regained power. FLIR's support additionally explained how this noise reduction was performed.

Noise Reduction is a temporal filter using consecutive frames with non constant weighing factors. This acts as a low pass filter which bandwidth makes it compatible with the time constant of the detector. It is normally activated by default. Normal streaming is obtained by deactivating it, with a resulting temporal noise increased by a factor of approximately 10.

(Raphael Danjoux - ATS Support, 21/06/2019)

What can be deduced from this explanation of the noise reduction used in camera is that it is designed to be used with the time constant of this specific camera, hence it is preferred to have to have this option disabled.

6.3. Internal Camera Parameters

Each FLIR camera requires extensive testing to determine the internal parameters used in calculating the final temperature. Each camera is calibrated using FLIR's exclusive 14-Point Inspection and Calibration program [131].

6.3.1. Temperature Parameters

These internal camera parameters stem from Planck's Law and its spectral radiance $I_\lambda(\lambda, T)$.

$$I_\lambda(\lambda, T) = \frac{2hc^2}{\lambda^5} \frac{1}{e^{\frac{hc}{\lambda k_B T}} - 1} [W \cdot sr^{-1} \cdot m^{-3}] \quad (6.1)$$

With:

- $I(\lambda, T)$: spectral radiance of a body I at unit wavelength λ and absolute temperature T ;
- h : Planck constant;
- c : speed of light in the medium;
- k_b : Boltzmann constant.

which can be rewritten as:

$$T = \frac{B}{\ln\left(\frac{R}{I} + 1\right)} \quad (6.2)$$

such that $R = \frac{2hc^2}{\lambda^5}$ and $B = \frac{hc}{k_B\lambda}$. I is proportional to FLIR A/D count S with an offset, so that:

$$I = R_2(S + O) \quad (6.3)$$

where R_2 is a constant factor, O is an offset, and $R = \frac{R_1}{R_2}$. Substituting in Eq. (6.2) yields the temperature equation FLIR uses in their cameras:

$$T = \frac{B}{\ln\left(\frac{R_1}{R_2(S+O)} + 1\right)} \quad (6.4)$$

Now taking into account emissivity and reflected apparent temperature, the total radiance S_{total} can be described as: $S_{total} = \epsilon S_{object} + (1 - \epsilon)S_{reflected}$ under the assumption that the radiance lost due to the contribution of the atmosphere is equal to 0, which it is essentially is at distances this thesis will be using and can be seen in Subsection 6.3.2. S_{total} can be rewritten as:

$$S_{object} = \frac{S_{total} - (1 - \epsilon)S_{reflected}}{\epsilon} \quad (6.5)$$

This yields a temperature of the object when S_{object} is substituted in Eq. (6.4) for S :

$$T_{object} = \frac{B}{\ln\left(\frac{R_1}{R_2(S_{object}+O)} + 1\right)} \quad (6.6)$$

FLIR has replaced the constant 1 in Planck's Law with F (range 0.5 - 2) and is found empirically during calibration. Eq (6.6) holds in case the emissivity of the object is equal to 1. This requires the object distance to be set to 0 and the external optics transmission to be set to 1 [133].

The different internal camera parameters can be found by using a tool, called ExifTool [132], on a file that was created by the camera, e.g. a *.img* or *.seq* file. By running this on such a file the following parameters were found:

- $R_1 = 14611.005$
- $B = 1390.5$
- $F = 1$
- $O = -5832$
- $R_2 = 0.010640447$

Using these parameters, a plot was made of the difference between a thermogram made by FLIR's Quick-Plot, and by using Eq. (6.6). This can be seen in Fig. 6.4. In this figure four plots can be seen. Top left depicts option 1, i.e. when using FLIR's software to create a thermograph, top right depicts option 2, i.e. when the models derived in this chapter are used to create a thermograph. Both bottom left and bottom right depict the difference between option 1 and option 2. Bottom left depicts this difference in a three dimensional graph for a more intuitive visualization.

From Fig. 6.4 it can be seen that the error is negligible, as the error is in the range of $1 \cdot 10^{-6}$.

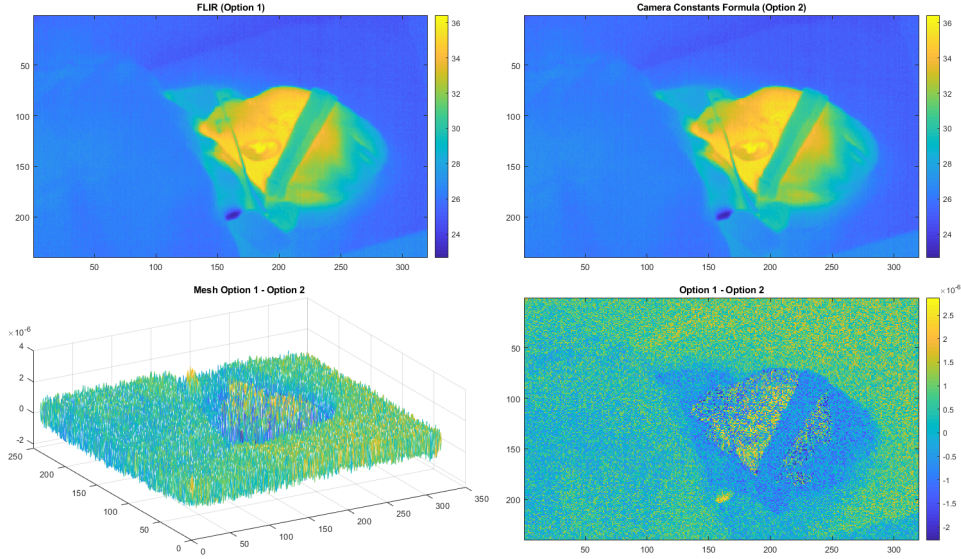


Figure 6.4: Thermogram's made by FLIR's QuickPlot (top left), and by the method described in 6.3 (top right) are depicted, together with the difference (bottom left and right). Bottom left depicts a 3D mesh to illustrate the difference more intuitively, whereas bottom right depicts the same difference in 2D.

6.3.2. Atmospheric Parameters

Additionally atmospheric losses can be calculated using the LOWTRAN 6 (1983) model which is shown in Eq. (6.7).

$$\tau_{atm}(d) = \exp \left[-\alpha \cdot \left(\sqrt{d} - \sqrt{d_{cal}} \right) - \beta \cdot (d - d_{cal}) \right] \quad (6.7)$$

It is known that a different type of infrared camera developed by FLIR uses the following equations, based on the LOWTRAN model, to calculate atmospheric transmissivity [13]:

$$\omega(RH, T_{atm}) = RH \cdot \exp \left(h_1 \cdot T_{atm}^3 + h_2 \cdot T_{atm}^2 + h_3 \cdot T_{atm} + h_4 \right) \quad (6.8)$$

$$\tau_{atm}(d, T_{atm}, \omega) = K_{atm} \cdot \exp \left[-\sqrt{d} \cdot (\alpha_1 + \beta_1 \cdot \sqrt{\omega}) \right] + (1 - K_{atm}) \cdot \exp \left[-\sqrt{d} \cdot (\alpha_2 + \beta_2 \cdot \sqrt{\omega}) \right] \quad (6.9)$$

$\omega(\omega\%, T_{atm})$ is the amount of water vapour in the atmosphere, h_{1-4} , $\alpha_{1,2}$, $\beta_{1,2}$ are camera parameters found experimentally, and K_{atm} is a scaling factor for the atmosphere damping. Using ExifTool, the internal parameters $\alpha_{1,2}$, $\beta_{1,2}$, and K_{atm} were found to be:

- $\alpha_1 = 0.006569$
- $\alpha_2 = 0.012620$
- $\beta_1 = -0.002276$
- $\beta_2 = -0.006670$
- $X = 1.900000$

h_{1-4} could not be found, so for the calculation of the atmospheric transmissivity, h_{1-4} from the *Therma-CAM PM 595 LW* were used [13]. The transmissivity was calculated from 0 to 2m for 23°C and 38°C, which are the minimum and maximum values respectively used in incubators. For each temperature the RH was changed from 0.4 to 0.8 with 0.1 incremental steps. The resulting graphs can be seen in Fig. 6.5.

From Fig. 6.5 it can be seen that at the largest distance that could possibly be used in the hospital, namely 2m, it can be seen that atmospheric losses under the worst condition, namely a RH of 0.8 and a temperature of 38°C, the transmissivity is still 0.984.

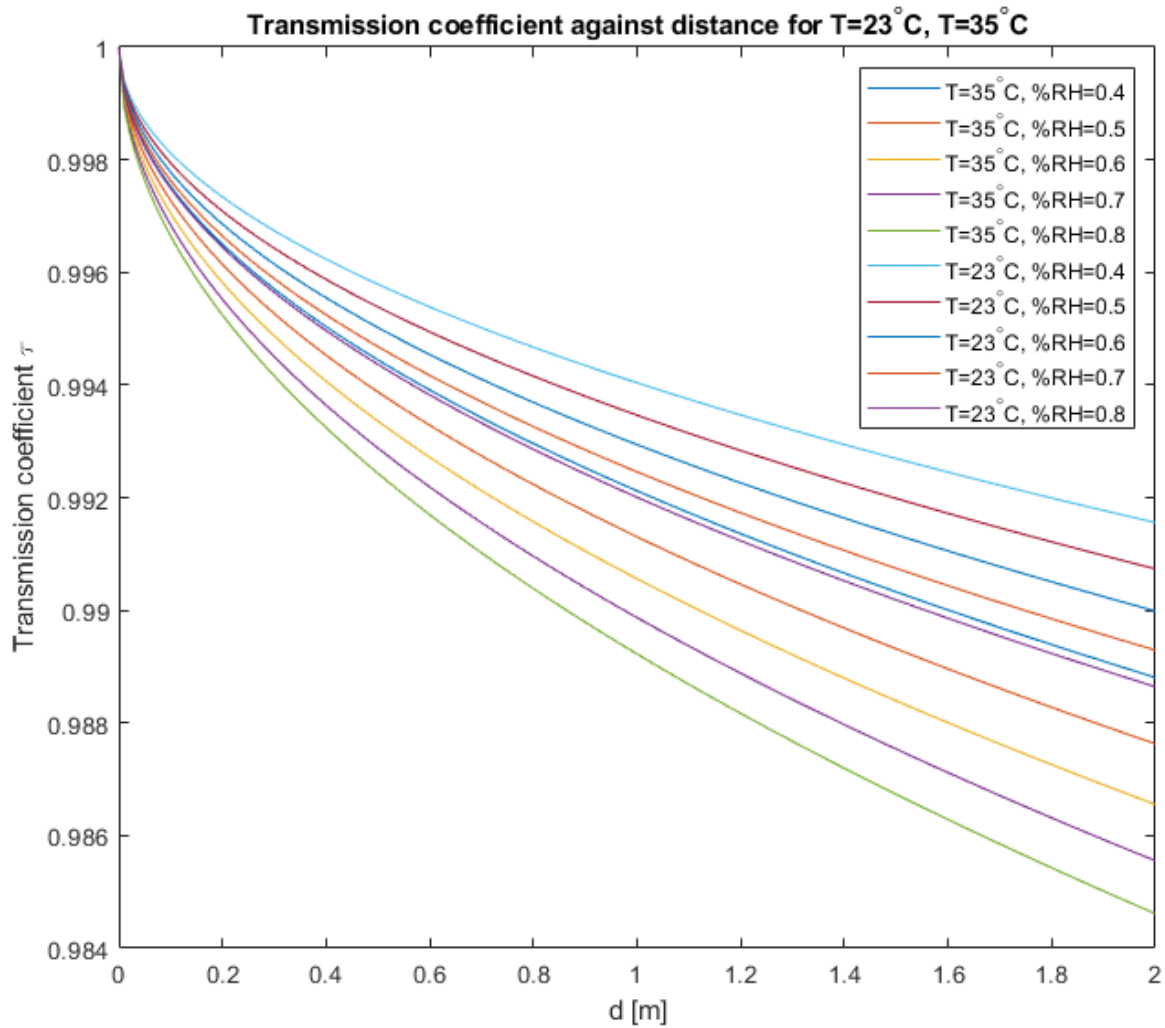


Figure 6.5: The transmissivity of the atmosphere using FLIR's model from 0 to 2 meter.

6.4. Conclusion

The minimum resolution has been determined, along with the minimum FOV. Based on this a selection of suitable cameras has been made, and a final choice was made. The FLIR One Pro seems to be the best camera for this specific application, mainly because of the availability of a (free) SDK. The internal camera parameters and settings have been explained, and a model based on these parameters was recreated in open-source software and compared to the manufacturer's software. Additionally, the LOWTRAN 6 model was used to determine the atmospheric losses up to 2m to determine whether atmospheric losses can be neglected.

7

Software

This chapter will describe the software that was written for this thesis. A pre-processing block diagram will give a high level (without going into detail of implementations) overview of the steps required from image acquisition to prediction algorithm (which will not be covered by this thesis). This will be followed by a list that selects several open-source GenICam tools to communicate with the camera. This is followed by an in-depth elaboration of the communication per incubator type, and how finally these two communications were combined into one application.

Per the described system in Chap. 5, both the measurement module, and the back-end module require that software is written for it to perform the functions this specific system requires. The measurement module requires software that, a.o., is able to read out incubator sensor values, whereas the back-end module requires software for the embedded system to control its communication. This chapter will describe the aforementioned software written for this project.

7.1. Pre-Processing Block Diagram

Before attempting to develop an algorithm that is able to predict infections, acquired data has to be pre-processed. This requires several steps to acquire the cleanest data to actually work with. A block diagram has been created that shows all steps required to create clean data. This block diagram can be seen in Fig. 7.1.

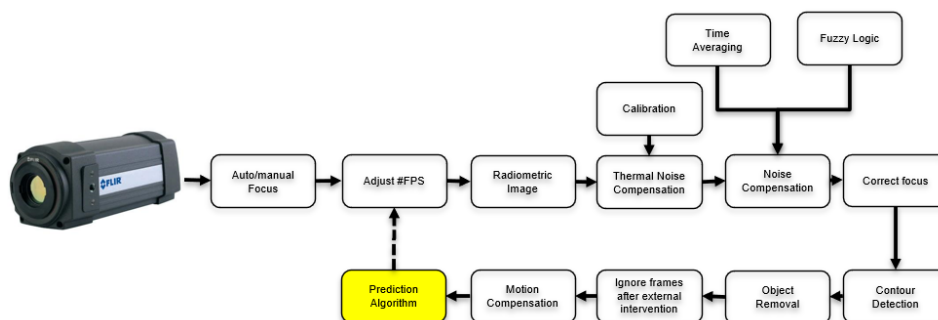


Figure 7.1: Pre-processing block diagram.

Starting from the camera on the left side, the following steps will have to be taken:

1. **Auto/Manual focus:** Acquiring a sharp image of the subject provides measurements that are more accurate.
2. **Adjust frames-per-second (FPS):** The FPS determines how smooth a temperature deviation will be, i.e. a higher FPS will allow for a smoother temperature increase/decrease, but comes at the cost of more data to be stored.
3. **Radiometric image:** Acquiring the data image in terms of ADC output count, rather than temperature.

4. **Thermal Noise Compensation:** Each incubator brand performs differently. The thermal aspects of a specific type of incubator can influence a measurement, and should be compensated for. This can be done by properly calibrating the measurement setup before a measurement.
5. **Noise compensation:** All data is inherently noisy due to non-ideal circuitry, and as such should be attempted to be made less so. The different types of noise are discussed in Sec. 3.3 and potential noise compensation methods (e.g. Time Averaging, or Fuzzy Logic) in Chap. 4.
6. **Correct focus:** If after the noise compensation it turns out, the subject is not correctly in focus, the focus should be adjusted through software.
7. **Contour Detection:** Only the neonate in question is of interest, which means contour detection will allow the elimination of areas that are not important.
8. **Object removal:** Subjects often have cables running over them, or clothes through which no temperature can be measured. These should not be taken into account for the final algorithm and should thus be ignored.
9. **Ignore frames after external intervention:** When a nurse or parent has reached into the incubator they disturb the internal system. Additionally they have more than likely touched the neonate and warmed/cooled it at that area. It will take some time before the system has returned to its original state, and thus based on these frames no conclusion should be made.
10. **Motion compensation:** Suppose the neonate's nose is at location $x = \{150, 151, \dots, 159, 160\}$, $y = \{110, 111, \dots, 119, 120\}$ and is of interest. If the neonate moves such that its nose ends up at $x = \{120, 121, \dots, 129, 130\}$, $y = \{110, 111, \dots, 119, 120\}$, the original coordinates no longer represent its nose. However if the prediction algorithm now tracks the original location, but a different body part is now at the original location, the prediction would base its prediction no longer on the nose.
11. **Prediction algorithm:** The actual algorithm which will predict whether a neonate is becoming ill. A dotted line trails back to the second block, *Adjust #FPS*, because as soon as the prediction algorithm senses an upcoming infection/illness, potentially more data should become available. However, on the contrary, when there is no reason to suspect an illness yet, the FPS can be lowered to save bandwidth.

7.2. Open Source GenICam Tools

One of the requirements is that the system should not rely on the (expensive) software created by the camera's manufacturers. Luckily, the camera can be controlled using a standard, namely the GenICam standard (which stands for Generic Interface for Cameras). Such a camera is completely described by an XML file. Such an XML provides a machine readable version of the camera's manual [26]. All a camera's features are mapped to registers in this file. This allows the user to write generic code that is compatible with different types of GenICam cameras. For instance, when trying to set the gain, this xml file will contain the corresponding register to set. This will then also work on a different camera that contains such an xml file, as this will contain the gain register for that specific camera.

Because the embedded system runs on Linux, it is imperative that the language used to program the camera is supported by Linux. Table 7.1 lists a number of possible tools to use the GenICam standard.

Table 7.1 lists multiple tools that can work with the GenICam standard. However when looking at the system requirements, some options are no longer a valid choice. By looking at the price requirement, the *Image Acquisition Toolbox* by Matlab, the *Atlas SDK for Matlab* by FLIR, and the *Ebus SDK* by Pleora Technologies are eliminated, due to the high price. A request for a quote was sent to National Instruments for their *Measurement and Automation Explorer (MAX)*, and to Stemmer Imaging for their Common Vision Blox software, but no response was received, hence the question mark in the price category. However, a request for a quote will more often than not yield a considerable price to pay and therefore these two options were also eliminated. Additionally, the *Atlas SDK* and *Spinnaker SDK* by FLIR are designed by the camera's brand, and preferably this should be avoided. Moreover, the Spinnaker SDK is not compatible with IRT cameras, even IRT cameras by FLIR itself.

This leaves the **Aravis Open Source Project**. It satisfies all requirements, i.e. it is free, open-source and thus not owned by a camera brand, and is developed in C which works on Linux.

Name & Manufacturer	OS	Language	Price	Notes
Image Acquisition Toolbox by MATLAB	Windows/Linux	MATLAB	€1250,-	<ul style="list-style-type: none"> Requires MATLAB license for €2650,-. Free for students.
Atlas SDK by FLIR	Windows	.NET encapsulated in MATLAB	–	<ul style="list-style-type: none"> Can read .seq files. Requires MATLAB license for €2650,-. Free for students.
Atlas SDK by FLIR	Windows	C#/.NET	–	<ul style="list-style-type: none"> Can read .seq files. Creating GUIs also simple in Visual C#.
Spinnaker SDK by FLIR	Windows/Linux	C/C++	–	Not compatible with IR cameras, only machine vision.
Measurement and Automation Explorer (MAX) by National Instruments	Windows	LabVIEW	?	Seems outdated and cumbersome.
Ebus SDK by Pleora Technologies	Windows/Linux/Mac	C++/.NET	\$500,-	Requires yearly subscription of \$2500,-.
Common Vision Blox by Stemmer Imaging	Windows/Linux/ARM/Linux	VB/VB.NET/ C#/Visual C++/Intel C++/ Delphi	?	–
Aravis Open Source Project	Linux	C/Python	–	–

Table 7.1: Different methods to program the camera using the GenICam standard.

7.2.1. Aravis Open Source Project

Aravis is a glib/gobject based library to acquire videos with cameras that are based on the GenICam standard [27]. To use Aravis, the following packages are required:

- libc6 (>= 2.29)
- libglib2.0-0 (>= 2.37.3)
- libgstreamer1.0-0 (>= 1.4.0)
- libusb-1.0-0 (>= 2:1.0.9)
- libxml2 (>= 2.7.4)
- zlib1g (>= 1:1.1.4)

The minimum required version is stated after the name of the package, as: (>=x.y), which is to be read as: to function, Aravis minimally requires version x.y of the stated package.

Aravis can also be run in Python [28]. To do so, an additional package is required, namely: **gir1.2-aravis-0.6 (0.6.0-3)**. The code that was developed to control the camera was written in python using these packages. Using aravis it is possible to extract the xml file which fully describes the camera.

7.3. Incubator Communication

A connection must be made with an incubator to read out certain values, e.g. the temperature probes' values, the alarm settings, the user-set temperature, etc. Most importantly for this thesis is the ability to read out sensor values, and one in particular: temperature. Both the Dräger Caleo[®] and the GE Giraffe[™] Omnibed

can be interfaced with using an RS-232 connection. Sadly, equipping an incubator with such an option vastly increases the price of one, i.e. adding an RS-232 connection can cost several thousands of dollars/euros. In the JKZ they chose to add this option, thus all Dräger Caleo[®] incubators were equipped with an RS-232 connection. Sadly, the RDGG chose not to add this option. The researcher and his then-supervisor requested the RDGG to purchase at least one such an incubator so tests could be performed. After long back and forth communication between the RDGG and GE, finally one such incubator was to come to the hospital, however this would not be suited to actually have neonates in it. This incubator was purely to be used for measurements.

In order to connect to an incubator, several parameters have to be set to create an RS-232 connection. These parameters only vary in baudrate per incubator. Table 7.2 lists these parameters. GE requires the cable to be shielded and have a capacitance less than 1500pF [31]. Draeger states no such requirement, but suggests a cable of their own, namely the *Medi-Cable 83 06 488* [32]. The connector used for both incubators is a female, nine pin, d-type connector.

Variable	Dräger Caleo [®]	GE Giraffe [™] Omnibed
Baudrate	9600	19200
Databits	8	8
Startbits	1	1
Stopbits	1	1
Parity	none	none
Pin 1	Housing	–
Pin 2	Receive Data (RX)	RX
Pin 3	Transmit Data (TX)	TX
Pin 5	Ground	Ground

Table 7.2: RS-232 parameters used in each incubator.

For each incubator an individual program was written, both for use with Windows and with Linux. Eventually both programs were combined (in Linux) into one, that could automatically detect which incubator had been connected. This was done by creating an abstract class called: “Incubator”

7.3.1. GE Giraffe[™] Omnibed

The GE Giraffe[™] Omnibed sends a string containing product information, sensor and alarm values, and system states every 2 seconds. Such a string is in ASCII format and is formatted as follows:

AAA_B.BB,CCCC,DDDD,EEEE,FFFF,GGGG,HHH,J,K,L,MM,NNN,P,Q,RRRRR,SSSS,TT,UU,VVV,WWW,XX,00
 The string is comma delimited, which means that each sub-string corresponds with a different parameter. For instance, *AAA* is defined as the product type, where *B.BB* is the main application number. Not every individual parameter is of interest for this thesis, but for completeness, a table defining each parameter can be found in Appendix G.

In practice, the communication did not completely follow the documentation. The complete string would be sent in two separate strings. The first part would consist out of the substring “*AAA,...,WWW*”, which is mostly sensor values. Two seconds later the last part would be transmitted, namely: “*XX,00*”. In case of an alarm, or multiple, they are placed in the *XX* substring. As can be seen in Appendix G, the alarm list can become quite long, and perhaps this change was made because of it. The alarm list substring would then be appended to the sensor values substring to create the original string. Consequently, the string was searched for the word *OPEN*, which was a placeholder in case of a missing sensor value, to remove it. Finally the string would be prepared in such a manner that it could be sent to the influxdb database.

7.3.2. Dräger Caleo[®]

Communication with the Dräger Caleo[®] requires the user to send commands to the incubator and respond to “questions” asked by the incubator. This all follows the Medibus protocol.

Medibus Protocol

MEDIBUS is a software protocol intended to be used for exchanging data between a Dräger medical device and external medical or non-medical devices via RS 232 interfaces [32]. This protocol consists of two different types of messages: *commands*, and *responses*. A command is a request to acquire data from a device, or to control its function. A response is sent upon receiving a command.

Command A command is a string of ASCII characters. The structure of a command can be seen in Fig. 7.2.

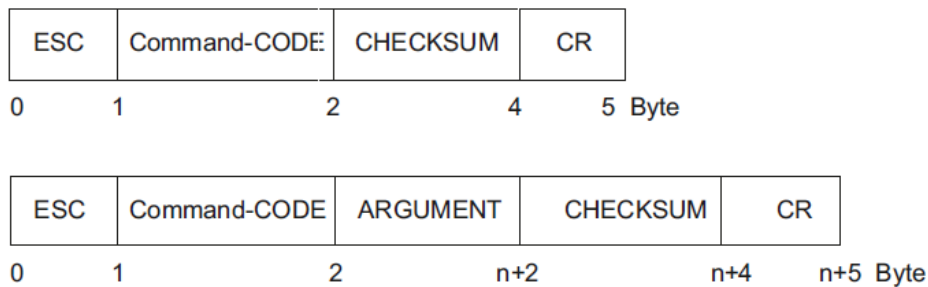


Figure 7.2: Medibus command structure. *Figure taken from [32]*

From Fig. 7.2 it can be seen that every command is started with an Escape (ESC) character and ended with a Carriage Return (CR). All ASCII characters can be written in one byte (8 bits) and can thus be written by values in the hexadecimal system, with $FF = 255$ being the maximum. The (hexa-)decimal value of each ASCII character can be found in any ASCII table online. The (hexa-)decimal values of ESC and CR are $1B_{hex}/027_{dec}$, and $0D_{hex}/013_{dec}$ respectively, where XX_{hex} denotes a hexadecimal value and XX_{dec} denotes a decimal value. In between these characters the actual command is written. Such a command consists of a decoded message, for instance an initialize communications command (ICC) is decoded as 51_{hex} . Several commands can require an argument. In such a case this argument would be placed immediately behind the command-code byte, and is of variable length, but can not exceed 251 bytes. Lastly a checksum has to be sent. This will be elaborated later.

Response Similar to a command, a response always starts and ends with the same character, namely a Start Of Header (SOH) with ASCII code $01_{hex}/001_{dec}$, and a CR. After the SOH an echo of the received command is sent. It is only after this that the actual response will be sent. This response block is also of variable length, but can be at most 3845 bytes. A response must be sent within 10 seconds, otherwise a communications time-out will occur. The response structure can be seen in Fig. 7.3.

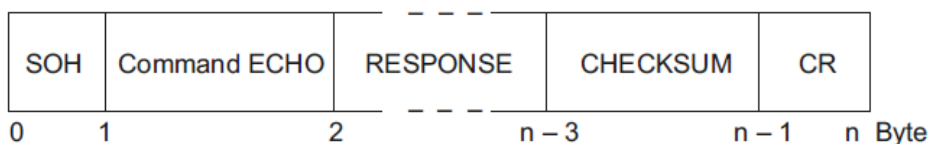


Figure 7.3: Medibus response structure. *Figure taken from [32]*

Two particular situations can arise: a response to an unknown command, or a corrupt command. In the former case the response structure is as follows: |SOH|Command-Echo|Check|sum|CR|, and |SOH|NAK|Check|sum|CR| for the latter. Each string between |...| represents a character.

Checksum Both the command and response messages require a checksum to be sent with it. This checksum is defined as: the least significant 8-bit sum of all preceding bytes beginning with "ESC" in ASCII hexadecimal format. This sum is then translated to hex and "split down the middle". Each half is then rewritten to hexadecimal. An example can be seen in Fig. 7.4.

A function has been written to automate the calculation of this checksum.

Decimal	=> HEX(H)	=> ASCII HEX Representation	
58	=> 3AH	ASCII "3" (33H)	ASCII "A" (41H)

Figure 7.4: Checksum calculation example. *Original figure taken from [32]*

Medibus Life-Cycle The medibus life-cycle consists out of 3 steps.

1. A Dräger device sends out an *initialize communications command* (ICC) approximately every three seconds or every 10 seconds if a non-complete response was received.
 - (a) When this ICC command is responded to by the other device, a “Request Device Identification” command is sent by the Dräger device. Upon a correct response, the device is now ready to receive commands.
2. If no communication had taken place for three seconds, the communication is assumed to be broken, and the device is set back to step 1 in the life-cycle. To prevent this from happening, a No Operation (NOP) command can be sent.
3. To stop communication a STOP command must be sent to the Dräger device.

Implementation

When the connection is started, an ICC command is received every two seconds from the Dräger Caleo[®]. A quite elaborate handshaking protocol is then be initiated, longer than described in the medibus life-cycle. This handshake proceeds as follows:

1. A response ICC message is sent according to the protocol.
2. The device sends an identification command, which is responded to in kind.
3. An identification command is requested from the device, to which a respond is to be received from the device.
4. Finally the date and time are requested.

The device would only be in a state ready to start providing sensor data after this handshake. Of highest interest are the temperature sensor values. Air temperature (TA), temperature probe 1 (T1), and temperature probe 2 (T2) are decoded as 6D_{hex}, C3_{hex}, and BE_{hex} respectively. All other decoded product information, sensor and alarm values, and system states are found in Appendix H. To request the measured data the command 24_{hex}/036_{dec} is sent. According to the Medibus protocol, only sensor values are transmitted of sensors that are actually connected. Suppose the temperature sensor probes and the inspiratory unit are not connected, the following communication occurs:

$$\text{TX} = |1\text{B}|24|33|46|0\text{D}|$$

$$\text{RX} = |01|24|36|43|20|31|39|20|36|44|33|33|2\text{E}|30|38|36|0\text{D}|$$

The received message is translated to hex and stored as a string to be able to process it, which yields:

$$\text{TX} = [\text{SOH}]\$6\text{C } 19 \text{ 6D}33.086[\text{CR}]$$

[SOH] and [CR] are non-printable characters, but are denoted between brackets for visualisation purposes. This string gives RH and air temperature values, 19% and 33.0°C respectively. A function was written to search through this string for decoded character combinations that correspond with a sensor.

Similarly a different command must be sent for subset 1 of the alarms, subset 2 of the alarms, and the device settings. When all these strings are received and decoded, the values are reordered to a format that so that the string can be sent to the influxdb database.

7.3.3. Combining Both Incubator Types

An implementation was written in which the incubator type, i.e. GE Giraffe™ Omnibed or Dräger Caleo®, is detected automatically. The UML-class diagram can be seen in Fig. 7.5.

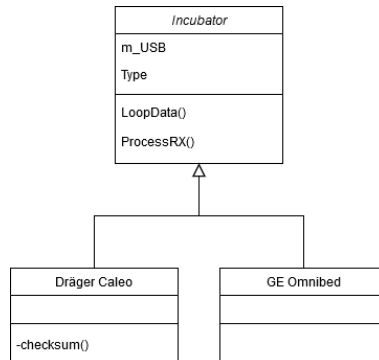


Figure 7.5: UML-diagram of the automatic incubator detection algorithm.

An abstract class was created that had two properties:

- *int* m_USB : flag whether rs-232 connection was set up properly.
- *string* Type : current type of incubator.

and two methods:

- *void* LoopData() : Loop that receives the data.
- *string* ProcessRX() : Manipulate the received data to a format that can be sent to the influxdb database.

The Dräger Caleo® also required a checksum in its messages, as was described earlier. This was implemented as a private function.

Unfortunately, both incubators have a different baud rate. An algorithm would start attempting an RS-232 connection at the lowest baudrate of the two: 9600. In the case that a GE Giraffe™ Omnibed incubator was connected, nonsensical data would be received. In the case of a Dräger Caleo® incubator, the known ICC command would be received. Based upon this, the algorithm as described in Sec. 7.3.2 would be initiated. However, a device that is attempting to send data through the wrong baud rate generates gibberish, but “data” is received nonetheless. To prevent accidental identification of the wrong incubator, several integrity checks had to be performed to ensure the right incubator was detected.

7.3.4. Store Measurement in Influxdb Database

To upload measurements to the database on the server, Curl was installed [29]. Curl is an open source file-transfer protocol used in command lines or scripts. An intern during this project wrote the script that would initialize curl. However, influxdb requires a certain query to write data to the database. This query has to adhere to following format:

```
[measurement],tag_set|field_set|timestamp|
```

Each query requires the name of the measurement, an optional tag set, a mandatory field set, and an optional timestamp. For all measurements the tag set and the timestamp were left empty. The timestamp was added automatically based on the server’s local nanosecond timestamp in UTC [130]. Suppose the RH, air temperature, and probe 1 temperature are received, the query would then look as follows:

```
jkzA T1=36,TA=33,RH=20
```

From this we can see the name of the measurement to be *jkzA*, the value of the temperature probe to be 36°C, the air temperature to be 33°C, and the RH to be 20%.

7.4. Conclusion

This chapter described all software design choices and written software. A pre-processing block diagram was developed through which data acquired by the camera should flow. Before such a block diagram can be implemented, an open-source tool was chosen to implement camera communication. After camera communication had been established, incubator communication had to be established. Both incubator types handle communication differently. For the Dräger Caleo[®], its communication protocol, medibus, was implemented, and communications with the GE Giraffe[™] Omnibed was implemented by reading out periodically transmitted data via RS-232. Received data from both incubators were manipulated into a standard string format, which was easy to upload to a database. They were then combined into one application, together with an automatic incubator type detection.

8

Data Acquisition Preparation and System

This chapter will give a detailed description of the data acquired during the study, along with information about patient selection, study protocol, study set-up, and the needed preprocessing processes that were required before they could be analysed.

In recent years, privacy has become a controversial topic. In order to maintain privacy of the individual, the general data protection regulation (GDPR) has come into existence. This regulation requires informed consent to be acquired when human research will be performed. In this case (premature) neonates are not capable of being properly informed and are unable to give their consent. The legal guardians of this population are allowed to give consent for them.

8.1. Human Research

Most research performed at the TU Delft is based on material properties and utilises physics to push the boundaries of science. Such research does not involve human test subjects. This thesis does require human test subjects, e.g. (preterm) neonates, who have rights, which are defended by committees that oversee the ethical impact of human research. Both the TU Delft and hospitals have their own Human Research Ethics Committees (HREC). Gaining approval from these committees is mandatory before human research can be performed. All HRECs use a checklist to determine whether the proposed research poses more than a minimal risk. Minimal risk is defined as every-day risks we face in daily life.

8.1.1. HREC TU Delft

Determining which documents are required for the HREC of the TU Delft is performed via a checklist. This checklist will determine the risk of the proposed research. This checklist will be reviewed by the secretary and the chair of the HREC and will take approximately two weeks.

It should be noted that the HREC of the TU Delft is not a medical ethics committee. In the case of research involving medical care or device, approval from a medical ethics committee is required.

HREC TU Delft Checklist

This checklist requires a summary of the research and risk assessment. This is followed by 13 questions which can be answered by yes or no. The first 10 questions inquire about the vulnerability of the test subjects, their privacy, and whether bodily test samples will be taken. Should any of these questions be answered with “yes”, a full proposal has to be submitted. Question 11 inquires about the privacy of the test subjects: whether videos, images, or other identifiable data be stored. If this is answered with “yes” an informed consent form has to be written. Question 12 determines whether a device that is not CE certified will be used in the research. If so, a device report has to be added. Finally they inquire whether a proposal of the research will be sent to a research ethics committee other than the HREC of the TU Delft. In this case the approval of the other HREC committee has to be added. This form can be seen in Appendix B.

Full Proposal

For this study the first question of the checklist has been answered with “yes”, i.e. a full proposal has to be written. For this full proposal a short summary has to be written. Afterwards three sections are required to be

filled in. The section “Research” and “Participants” are essentially a more detailed questionnaire compared to the first 10 questions of the checklist but are straightforward to answer. The minimum and maximum amount of participants is required, which could require sample size calculations (but these are not required for this document). The “Privacy” section requires information on how patient data will be made anonymous (if possible) and stored. The filled in proposal can be seen in Appendix C.

Informed Consent

Thermography requires videos or images to be captured, thus the answer to checklist question 11 is also “yes”. Thus an informed consent form has to be written. An informed consent form also requires an information leaflet, so that caretakers know what they are agreeing to. This leaflet entails the following information:

- An introduction.
- The research goal, background, and procedure.
- Possible risks and benefits to participating in this research.
- Confidentiality and sensitive information.
- Participating and quitting.
- Compensation for participation in this research.
- Contact information.
- Written consent form.

As the study was performed in The Netherlands, this leaflet and the form are written in Dutch and can be found in Appendix D.

Approval Other HREC

Finally an approval of the submission to a different HREC is required. How to acquire this will be elaborated upon in Sec. 8.1.2.

8.1.2. HREC Southwest Holland

The forms and checklists described above are those required for the HREC of the TU Delft. For the HREC of a hospital, different forms are required. They require a submission letter, checklist to determine whether the research falls under the law Medical-Scientific Research with People (Wet Medisch-Wetenschappelijk Onderzoek met Mensen (WMO)), a research protocol, questionnaires (if the research involves handing out questionnaires to participants), and an information leaflet with written consent form (which has been described in Sec. 8.1.1).

WMO Checklist

When doing research on people, laws have been created to protect the rights, safety, and privacy of participants. If the research involves the participant to perform certain actions, or (sensitive) personal information will be acquired, or the participant will be exposed to pain, or the participant is unable to give informed consent, different measures have to be taken. Luckily, this research does not fall under this law, and thus no extra legal measures have to be taken. This checklist can be found in Appendix E.

Research Protocol

The research protocol is perhaps the most important document for the HREC. The Hagaziekenhuis provides a template for such a protocol. This protocol requires elaborate explanation of

- The research:
An introduction and rationale that explains why this research is beneficial.
- The objectives:
Describes the primary and secondary objectives of the research.

- Study design:
A description of the population, and when a participant is eligible to be included, and when they must be excluded, sample size calculation of this population, study parameters/endpoints of the primary and secondary objectives, study procedures, materials.
- Statistical Analysis

8.1.3. Board of Directors

Not only do these forms have to be submitted to an independent HREC, some of these forms and extra have to be submitted to the board of directors of the corresponding hospital. These extras require a signature from the researcher from the hospital. The documents the board of directors requires are as follows:

- Signed non-WMO (nWMO) form from the independent HREC as described in 8.1.2.
- Research protocol as described in Sec. 8.1.2.
- Information leaflet and written consent form:
Described in 8.1.1.
- Research declaration:
Whether or not the research is feasible at the department. Signed by an authorized person of the department.
- Declaration of the involved departments:
Requires the names and signatures of involved department heads. Signed by the local researcher.
- Copy of a valid Good Clinical Practices (GCP) or “Basiscursus Regelgeving en Organisatie voor Klinisch” (BROK). Provided by the local researcher.
- (If relevant) Budget:
Signed by the authorized person from the department.
- CV:
CV of the local researcher, signed.

8.1.4. Flowchart of Forms and Proposals for HREC

Finding all these forms and templates can be quite confusing and intimidating. A flowchart that is intended to follow so that submitting a proposal to a HREC can become easier can be found in Appendix F.

8.2. Patients

For this thesis, 26 patients were included from February 2019 up to and including June 2019 which has led to roughly 30 hours of infrared film material. Initially neonates were eligible to be included for this research if they were born prematurely, both ill and healthy. However, due to the low number of premature children of which the guardians had given consent, the inclusion criteria was expanded to also include term neonates.

To increase the number of eligible neonates, this research was introduced in both the RDGG and JKZ. Both agreed to participate. In Fig. 8.1 the total number of children included per hospital can be seen. From Fig. 8.1a it can be seen that a total of 11 neonates were included in the JKZ and from Fig. 8.1b it can be seen that a total of 15 neonates were included in the RDGG.

Subjects *jkzJ*, *rdggA*, *rdggK*, *rdggL*, and *rdggN* were filmed twice. For subject *rdggA* the reason was that it was feared that not enough subjects would be found during the planned course of this master thesis and thus an insufficient amount of data would be recorded. In the end, this master thesis got prolonged and more neonates were included.

Subjects *jkzA*, *rdggK*, and *rdggN* were said to be ill, or suspected to be ill and therefore they were recorded once daily in two consecutive days, in the hope that they would show progress towards a healthy condition and that it would be visible in an IRT recording. This was done with consent from the guardians of the neonate and from the hospital.

For subjects *jkzE*, *rdggM*, *rdggN*, and *rdggO*, their age wasn't recorded.

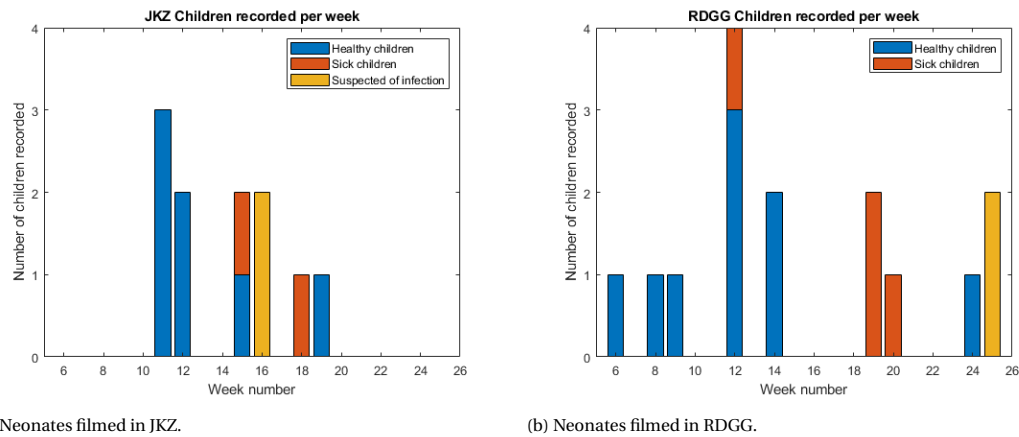


Figure 8.1: Number of included children in both the JKZ and RDGG. Blue bars depict healthy children, red depict sick children, orange depict children who are suspected to have an infection.

Table 8.1: Neonates filmed in JKZ.

Date Recorded	Patient	Aog	Age	Condition
15-03-2019	jkzA	33.1	2.4	Healthy
15-03-2019	jkzB	31.5	2.5	Healthy
15-03-2019	jkzC	31.1	2.5	Healthy
20-03-2019	jkzD	37.6	4.6	Healthy
20-03-2019	jkzE	27.0	–	Healthy
11-04-2019	jkzF	32.4	2.2	Healthy
11-04-2019	jkzG	28.6	2.6	Ill
17-04-2019	jkzH	37.4	0.2	Suspected illness
17-04-2019	jkzI	28.3	4.6	Suspected illness
02-05-2019	jkzJ	42.0	0.1	Ill
03-05-2019	jkzJ		0.2	Ill
05-05-2019	jkzK	26.3	8.2	Healthy

aog: age of gestation

Table 8.2: Neonates filmed in RDGG.

Date Recorded	Patient	Aog	Age	Condition
05-02-2019	rdggA	32.2	2.4	Healthy
08-02-2019	rdggA		3.0	Healthy
19-02-2019	rdggB	37.4	0.5	Healthy
01-03-2019	rdggC	36.3	0.5	Healthy
01-03-2019	rdggD	33.6	0.2	Healthy
18-03-2019	rdggE	33.2	0.5	Healthy
19-03-2019	rdggF	40.1	0.5	Healthy
22-03-2019	rdggG	34.4	0.4	Healthy
22-03-2019	rdggH	42.1	0.3	Ill
02-04-2019	rdggI	35.2	0.4	Healthy
03-04-2019	rdggJ	30.6	0.6	Healthy
07-05-2019	rdggK	40.2	0.4	Ill
08-05-2019	rdggK		0.5	Ill
10-05-2019	rdggL	39.0	0.1	Ill
13-05-2019	rdggL		0.4	Ill
13-06-2019	rdggM	–	–	Ill
20-06-2019	rdggN	35.2	–	Suspected illness
21-06-2019	rdggN		–	Suspected illness
21-06-2019	rdggO	38.6	–	Suspected illness

Table 8.3: Neonate included per hospital, including their age of gestation, age at moment of filming, and their condition. Both aog and age are written as x,y , where x = weeks, y = days.

8.3. Study Protocol

Before recording a neonate, informed consent was required from the legal guardian(s). The researcher does not have a degree in care and it was thus decided that nurses and paediatricians would acquire written informed consent. Moreover, the researcher worked on this master thesis at the TU Delft in Building 36 on the 15th floor which brought along logistical impracticalities of acquiring informed consent personally. The protocol was designed as follows:

1. Acquire written informed consent.
2. Set up measurement setup.
3. Have nurse place temperature sensor.

4. Start measurement for 30 minutes.
5. Adjust setup after 30 minutes.
6. End measurement after additional 30 minutes and remove setup.

The recording itself requires nothing from the neonate or its guardian(s). The researcher would set up the measurement setup after informed consent was acquired. In order to do so, he brought a laptop, ethernet cable, IRT camera and tripod. Additionally, a nurse was asked to place a skin temperature sensor. The measurement was started, after which the researcher would leave the room for privacy of the subjects and their guardians. The measurement would run for 30 minutes, after which the researcher would come in to check the measurement setup and make changes if that was warranted. Guardians and/or nurses could stay in the room and continue their business as usual. It was not required for anyone to be in the room during the measurement.

For 5 subjects it was requested that the researcher did not come in after 30 minutes due to personal reasons. For these subjects the camera was left to record for one hour straight.

After all results were ready, data was properly anonymised in order to be analysed by the researcher.

8.4. Experimental Settings

Due to the way the study is set up, two different measurements would rarely be exactly the same with respect to the way the tools were set up. A neonate was assigned a room where it would stay for an allotted amount of time. In this room the measurement setup would be set up. In Fig. 8.2 two possible setups per hospital are depicted. Fig. 8.2a shows a measurement setup in the JKZ, where Fig. 8.2b shows a measurement setup at the RDGG.



(a) Measurement setup in JKZ.

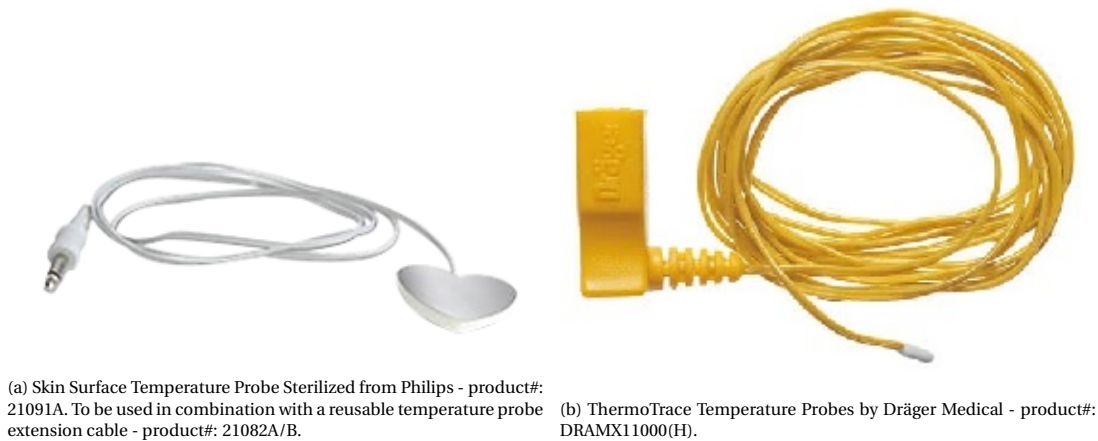
(b) Measurement setup in RDGG.

Figure 8.2: Measurement setup per hospital.

Due to privacy concerns no pictures were made with the neonate in the incubator. From Fig. 8.2 it can already be seen that there are numerous differences: a different incubator, different room and layout and thus a different distance from camera to incubator, etc. The fundamentals of the measurement setup were the same for each recording (as discussed in Chapter 5), however if a neonate was positioned so that no skin was visible, the camera was placed at an angle, or heightened, or both. Similarly, if the nurse could not reach the child with the camera at a certain position, it would also be displaced so that this was no longer an issue. Additionally, not each subject would lie in an incubator, but instead would be lying in a cradle, on a mattress during jaundice treatment, or in an incubator during jaundice treatment. All such variables were measured and written down, both regarding the subject, and the measurement setup. Recorded variables include: health condition (healthy, ill, suspected illness), camera angle and distance, through which porthole was recorded, rectal-, skin-, and room temperature, birth weight, and finally weight during filming. For most neonates administered medicine was also written down. It was attempted to keep most variables the same across measurements.

8.4.1. Temperature Sensors

Currently measurements of the skin temperature are performed by using thermistors and are considered the gold standard, hence these sensors are chosen to perform these measurements. A GE Giraffe™ Omnibed incubator requires a skin temperature sensor that is different from the one required in a Dräger Caleo® incubator. Each skin temperature sensor can be seen in Fig. 8.3a and Fig. 8.3b respectively.



The incubator is not heated uniformly due to a fan blowing hot air into the compartment [63]. This yields varying temperatures at different locations in the compartment. To study the functioning of an incubator, an object was chosen that did not produce any heat on its own but would adopt the temperature at a specific location. For this, a paperboard box was chosen. A thin piece of paperboard can adopt its temperature environment rather quickly. Heat patterns can be created of the incubator for different incubator temperatures. An added benefit is that these boxes are readily available in the hospital in the form of glove storage boxes. It is important to note that there are multiple manners of applying a temperature sensor. These methods can be seen in Fig. 8.4. The adhesive that was used to stick the sensor to the surface of the object, is the same that is used by the nurses to place a temperature sensor on the skin surface.

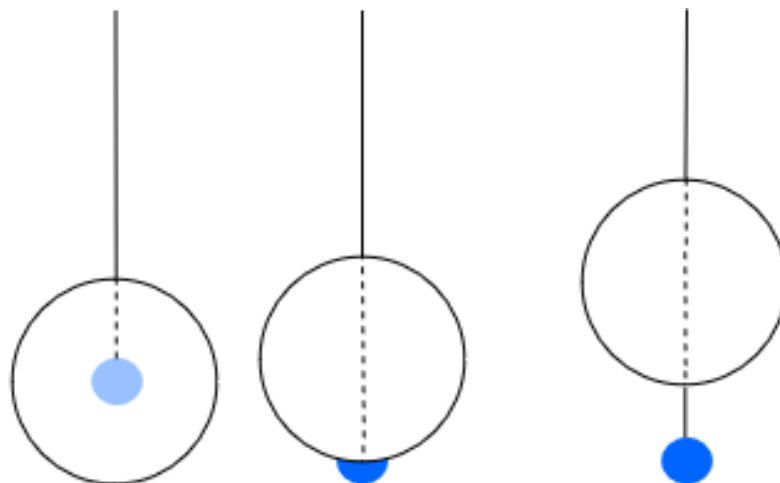


Figure 8.4: Different methods of applying a temperature surface to a surface. The blue circle represents the temperature sensor, whereas the black circle represents the that adhesive.

Additionally, for specific measurements, a rectangular and a cylindrical aluminium block were used. The emissivity is less at surface curves flowing away from the camera [40], whereas a completely flat surface, i.e. the rectangular block, does not have this problem. Moreover, aluminium blocks can be warmed uniformly. Unfortunately, the reflectivity of aluminium is very high [2], which would yield unusable measurements with an IRT camera, as the measurement would represent the surrounding environment temperature rather than the actual temperature of the aluminium block. To counteract this, black electrical tape, or insulating tape, can be taped to it [123].

These aluminium blocks will eventually assume the environment temperature. Perhaps a preterm neonate will behave similarly, if left unchecked, but this would impose a health risk. This is due to the fact that preterm neonates have little temperature regulating abilities. This is confirmed by the nurses and physicians who have told the researcher that current practice is to higher/lower T_{set} when they conclude that the neonate's temperature is too low/high respectively. In this sense these aluminium blocks represent a neonate fairly well.

Additionally aluminium transfers heat at a similar rate as the outer layer of the human skin: thermal conductivity of aluminium is 205 W/m.K [16], whereas the epidermal layer in human skin was found to be 209 W/m.K [17].

8.5. IRT Camera Data Acquisition

Before custom software was written that would be able to record without having to use expensive software developed by the camera manufacturer, FLIR's own measurement software was used: *FLIR QuickPlot*. The GUI can be seen in Fig. 8.5. It was installed on the researcher's laptop.

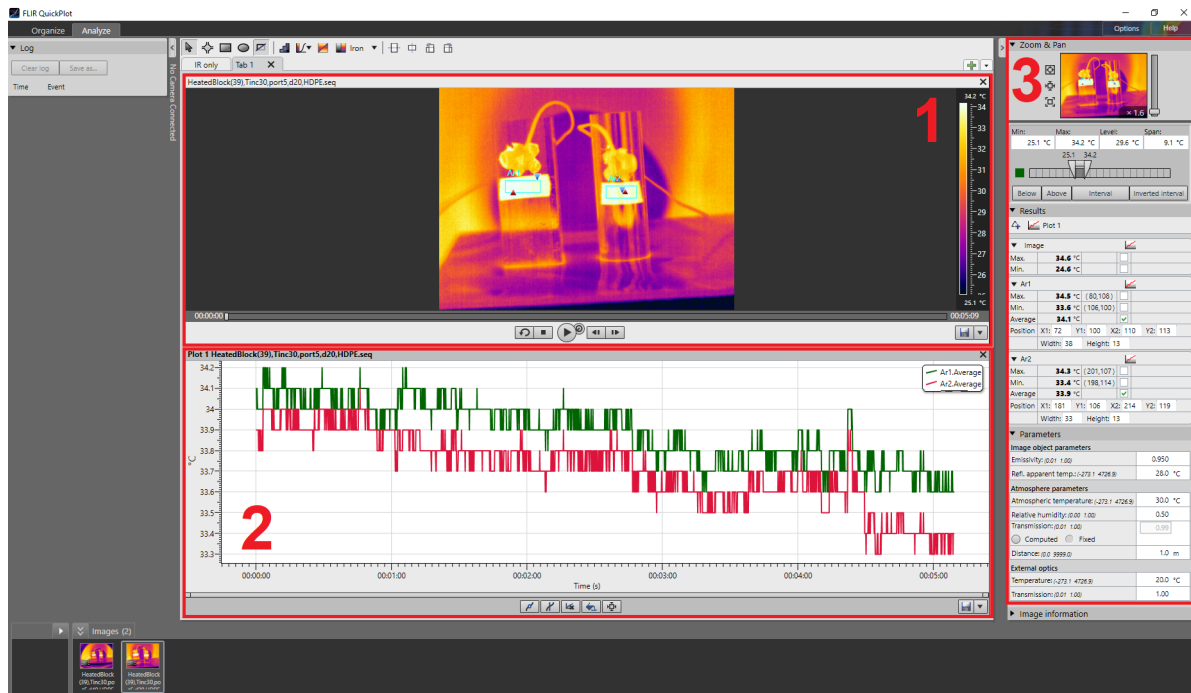


Figure 8.5: FLIR QuickPlot.

In Fig. 8.5 three panels have been numbered. Each panel requires some explaining:

1. **Image Viewer:** In this panel the live stream from the camera can be displayed, or a previously recorded item. A live stream written to disk creates a file with a .seq extension. If a snapshot is created, a .img file is created.

Using items from the toolbar above this panel, a measurement point, rectangle, or ellipse can be placed in the image viewer. The play control buttons underneath the image function as any other play control buttons. In Fig. 8.5 two rectangular measurements have been placed, named *Ar1*, and *Ar2*.

2. **Plot Control:** In this panel graphs from the image viewer can be displayed. By right-clicking a measurement point, rectangle, or ellipse, the maximum, minimum, or average can be displayed. In the current figure, both the average for *Ar1* and *Ar2* are displayed. The software rounds measurements up or down to 1 decimal values. Bottom right displays the *Save* icon. By clicking this, the graph can be exported to a .PNG file, or a .CSV file.
3. **Image Properties:** This panel displays properties of the image in Panel 1. Zoom & pan can be adjusted, a checkbox can be checked to display the minimum, maximum, and/or the average of set measurements from Panel 1 in Panel 2, and most importantly, the image object parameters (emissivity, reflected apparent temperature), atmosphere parameters (atmospheric temperature, RH, transmission, distance), and the external optics parameters (temperature, transmission) can be set.

8.6. Conclusion

This chapter has explained in detail how permission was granted to perform n-WMO research on neonates as part of a master's thesis, and which steps were taken to acquire this permission. The number and type of patient was elaborated, along with the study protocol, experimental setting, and data acquisition software.

9

Measurements

In this chapter only an explanation of the measurements and the resulting graphs will be discussed. For a discussion of the results, see Chapter 10.

Equipped with software that can log incubator sensor values, actual measurements can be performed. Two different types of measurements are made: measurements that do not record neonates inside an incubator, and measurements that do. The former is done to create an understanding of the incubator, the thermodynamics at play, and the effects on IRT, whereas the latter has been performed to acquire data that will be used to implement the block diagram as described in Sec. 7.1. However, before any of this can be performed, several parameters will be determined which are used in the temperature calculations.

9.1. Missing Data

Unforeseen circumstances have led to the researcher parting ways with his previous supervisor. Per agreement with the previous supervisor, all research material was to be returned or destroyed. During the process of returning or destroying data acquired during the research, prof. dr. ir. W. A. Serdijn was found willing to take over supervision of the researcher. Most data had already been lost to the researcher. This included: rights to access the cloud service used by the company of the previous supervisor, IRT recordings of the incubator measurements, IRT of the neonatal measurements, physical research notes, keycards with access to the neonatal ward in both hospitals, and a virtual machine running the embedded system. The researcher had saved one electronic folder containing submitted reports, but that had not been graded, as a form of backup. Within this folder were found draft versions of the final report. Figures included in this thesis were either drawn later or found in the literature study and/or final report drafts. Graphs included in this thesis are screenshots made of graphs created during the thesis. Gaps in certain measurements will be present.

9.2. Quantifying Interaction Between IRT and Incubator

Measurements that would give insight into the workings of an incubator were performed by applying a temperature sensor on an object and filming said object with the IR camera. Due to non-uniform heating of the compartment, the placement of the object is of importance and should be kept track of. Potential opened portholes can influence the environment inside the compartment and should thus also be taken into consideration. In order to keep track of the procedure a measurement was performed in, the portholes have been numbered. The numbering of the portholes can be seen in Fig. 9.1. The green numbers represent the portholes, whereas the blue numbers represent the sides. Porthole 3 and 6 are not always present, in such an event, the numbering will continue as if they had been, thus portholes 5 and 4 will always be on the opposite side of porthole 1 and 2 respectively. When viewing the incubator from above, the location of the “Display” is used as position reference. By going clockwise from the display, each present porthole increases the porthole numbering by one. The infant is always positioned with its head towards the display.

As the camera cannot measure through the material of the canopy, at least one porthole will have to be opened. This should not affect the temperature in the compartment, but in reality the temperature will drop [10],[11].

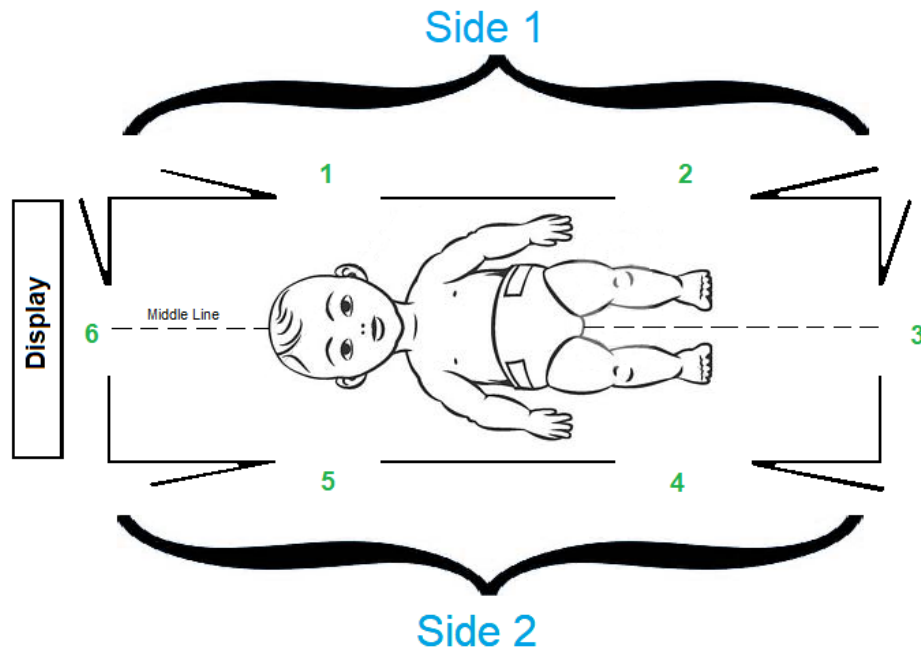


Figure 9.1: Numbering of the portholes of an incubator.

During the measurements on these sensors, the IRT also measured the paperboard box inside the incubator, either through an unsealed porthole, or sealed. To acquire proper temperature values from the IRT camera, certain parameters need to be determined. These include the following:

- Emissivity of the object (ϵ_{obj}).
- Reflected Apparent Temperature (RAT).
- Atmospheric temperature (T_{atm}).
- Relative humidity (RH).
- Atmospheric transmission coefficient (τ_{atm}).
- Distance from camera to object.

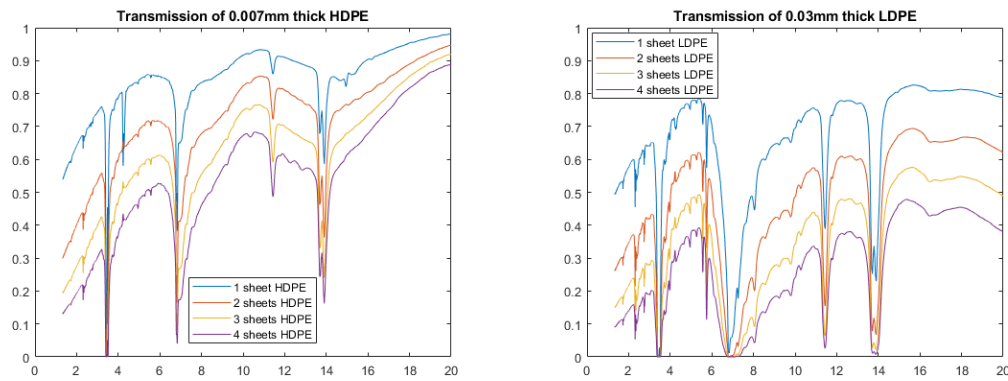
And in case of an external optic window:

- Temperature of the optic (T_{opt}).
- Transmission coefficient of the optic (τ_{opt}).

Luckily most of these can be determined fairly easily. Emissivity of objects has been determined thoroughly and can be found in plenty of tables [2][4][5]. For the paperboard box which has a glossy surface, an emissivity of $\epsilon = 0.88 - 0.9$ is found [2]. For the RAT see Sec. 9.2.2. The atmospheric temperature can be read from the thermostat, and relative humidity indoors is generally around 50%. The atmospheric transmission coefficient can be set to 1 for small distances [12]. The distance from camera to object can easily be measured.

9.2.1. External Optic Window

In the event of an external optic window, e.g. (low/high density) polyethylene (LDPE/HDPE) foil, the transmission coefficient was determined using Fourier-transform infrared (FTIR) spectroscopy with a resolution of 4cm^{-1} with 16 scan time for both sample and background for wavelengths ranging from $1\mu\text{m}$ to $20\mu\text{m}$ and can be seen in Fig. 9.2a, 9.2b respectively. HPDE was 0.007mm thick, whereas LDPE was 0.03mm thick. First a background measurement was performed. This included no foil. Afterwards the same measurement was performed with the foil so that the difference between the two would yield the transmittance.

(a) Transmission of HDPE for $0 < \lambda < 20\mu\text{m}$.(b) Transmission of LDPE for $0 < \lambda < 20\mu\text{m}$.

The percentage of the total spectral energy per wavelength from $7.5\mu\text{m}$ to $13\mu\text{m}$ with $0.1\mu\text{m}$ step size using Planck's Law was determined, by dividing the spectral radiance per wavelength with the area under the line of only one sheet of foil in Fig. 9.2a, and 9.2b. The transmission per wavelength of LDPE/HDPE was multiplied with the spectral radiance per wavelength percentage and summed from $7.5\mu\text{m}$ to $13\mu\text{m}$, as this is the range of the IRT camera. This way the average transmittance can be calculated. This leads to: $\tau_{HDPE} = 0.88$ and $\tau_{LDPE} = 0.64$.

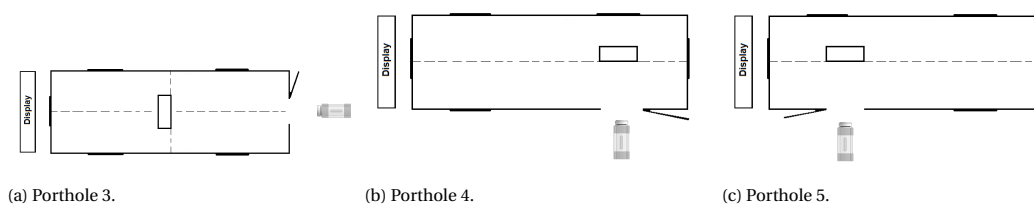
9.2.2. Reflected Apparent Temperature (RAT)

In order to make accurate measurements, it is important to determine the emissivity of the object under consideration and the RAT. The RAT takes into consideration all potential heat sources that could reflect upon the object, and thus add an error to the measurement, as described in Sec. 3.1. Determining the RAT can be difficult, yet is important to acquire a close approximation as the RAT and the atmospheric temperature constitute approximately 25% of the total temperature reading at an emissivity of $\epsilon = 0.8$ and a temperature between 20 and 50°C [1]. Luckily by using a piece of aluminium foil, which is highly reflective of infrared radiation, it can be determined [1]:

1. Crumble a piece of aluminium foil.
2. Uncrumble the foil.
3. Place it on a flat object in front of the object (at a short distance) under consideration, e.g. a piece of cardboard, with the aluminium foil facing the camera.
4. Set the emissivity to 1.
5. Measure the apparent temperature of the aluminium foil using an average over a region of interest on the foil and average over time. The resulting value is the RAT.

All steps were followed for both the GE GiraffeTM Omnibed and Dräger Caleo[®] incubator. When the aluminium was viewed through one porthole, the others were closed. This was done at temperatures ranging from $29\text{--}35^\circ\text{C}$. Similar to what can be seen in Fig. 8.5, a measurement rectangle was drawn over the entire surface of the aluminium foil on the box in FLIR QuickPlot. From this rectangle the average was taken.

The measurement setup can be seen, per porthole, in Fig. 9.3.



(a) Porthole 3.

(b) Porthole 4.

(c) Porthole 5.

Figure 9.3: Measurement setups used to determine the RAT per porthole.

The measurement has been performed for portholes 3, 4, and 5, under the assumption that the RAT would be the same for porthole 1 and 5, as well as for porthole 2 and 4. This allowed for a mapping of the RAT per porthole per set temperature setting. The results of this can be seen in Tables 9.1, and 9.2. Additionally the RAT at room temperature was measured using the same method, and was found to be: 23.87°C.

Porthole		RAT [°C]		
		3	2/4	1/5
Set incubator temperature [°C]	29	28.25	28.11	27.81
	30	29.01	28.32	28.08
	31	29.90	29.32	28.74
	32	30.36	30.14	30.10
	33	30.79	30.30	30.24
	34	32.12	31.27	30.78
	35	32.37	31.83	31.47

Table 9.1: RAT determined per porthole for temperature settings ranging from 29-35°C for the GE Giraffe™ Omnibed incubator.

Porthole		RAT[°C]	
		2/4	1/5
Set incubator temperature [°C]	29	26.86	27.25
	30	27.47	27.70
	31	28.08	28.43
	32	28.66	29.09
	33	29.30	29.84
	34	29.70	30.07
	35	30.49	30.59

Table 9.2: RAT determined per porthole for temperature settings ranging from 29-35°C for the Dräger Caleo® incubator.

9.2.3. Accuracy GE Temperature Sensor

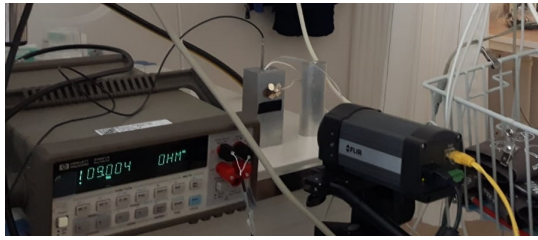
A measurement was performed to check the accuracy of both the temperature sensors that are used in the hospitals, and the IRT camera under assumption that all parameters are set correctly. In preparation for this, two cylindrical cavities were drilled into the blocks to the centre. Such a cavity allows for a calibrated Pt-100 temperature sensor to be placed in it, and a GE temperature sensor in the other. This was done so that the temperature sensors are surrounded by the aluminium block and are influenced as little as possible by external temperatures. Another GE temperature sensor was placed on the outside of the aluminium block using the same hospital adhesive pad that was used in the other measurements. Finally, a piece of electrical tape, or insulating tape, was placed on the aluminium block next to the GE temperature sensor on the surface so that the IRT camera could perform measurements, as explained in Sec. 8.4.1. The Pt-100 sensor had to be read out using a digital multimeter and logged manually. The aluminium blocks were positioned 30cm from the camera on a desk. The measurement setup can be seen in Fig. 9.4a. The resulting temperatures can be seen in Fig. 9.4b.

9.2.4. Changing the Distance from Camera to Incubator

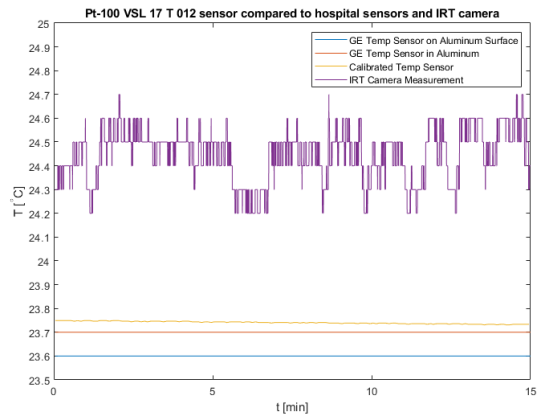
As was discussed in Sec. 6.3.2, the atmospheric transmission for temperatures of importance to this thesis, i.e. [20..38]°C, should not be significant enough to consider. This measurement is done to make sure this is actually the case. To do so, aluminium blocks were heated, taped with electrical tape, and temperature sensors were attached using a sticker that is also used to attach the sensor to the skin of neonates.

For this measurement, 4 different situations were used:

1. The aluminium blocks were heated in the incubator at $T_{\text{inc}} = 38^\circ\text{C}$ for the entire night. The next day the measurement was made through porthole 4 with $T_{\text{inc}} = 38^\circ\text{C}$.
2. The aluminium blocks were heated in the incubator at $T_{\text{inc}} = 38^\circ\text{C}$ for the entire night. The next day the measurement was made through porthole 5 with $T_{\text{inc}} = 38^\circ\text{C}$.



(a) Measurement setup used to measure using a calibrated Pt-100 temperature sensor.



(b) Temperature of the Pt-100 sensor, camera, and the GE temperature sensors.

3. The aluminium blocks were heated in a different incubator at $T = 39^{\circ}\text{C}$ for the entire night. The following day they were placed inside an incubator pre-heated at $T_{\text{inc}} = 30^{\circ}\text{C}$ and the measurement was made through port 5.
4. The aluminium blocks were heated in the incubator at $T_{\text{inc}} = 30^{\circ}\text{C}$ for the entire night. The next day the measurement was made through porthole 5 with $T_{\text{inc}} = 30^{\circ}\text{C}$.

The camera was placed at an initial distance of $d = 20\text{cm}$, measured from the lens of the camera to the porthole through which was filmed, and set to record for 5 minutes at 9Hz. Simultaneously, the incubator sensor readout was logged. Afterwards the data was synchronized. These measurements were performed using the GE Giraffe™ Omnibed incubator, hence the sensor readout was done at 0.5Hz. The measurement was stopped after 5 minutes and the camera was moved 20cm backwards. This was repeated up to $d = 120\text{cm}$. All four different measurements were made once with HDPE covering the porthole through which was filmed, once with LDPE, and once without any foil covering the porthole through which was filmed.

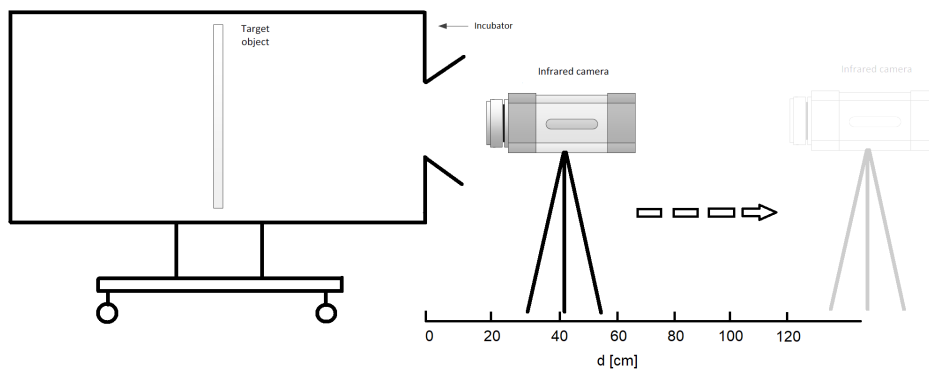
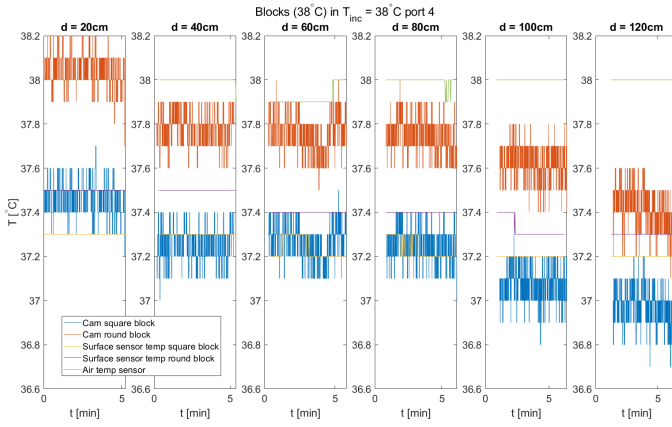
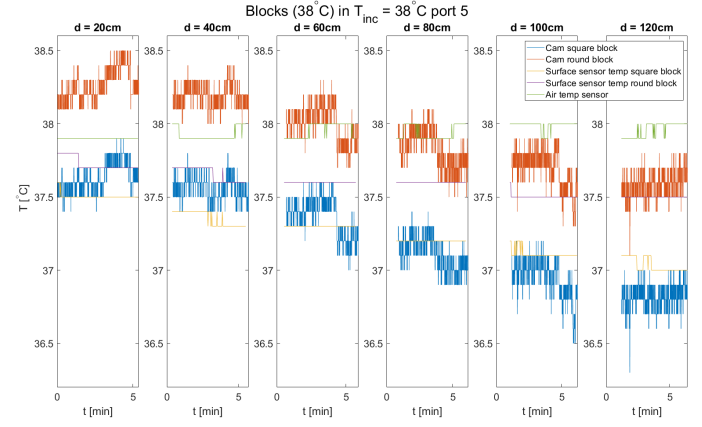
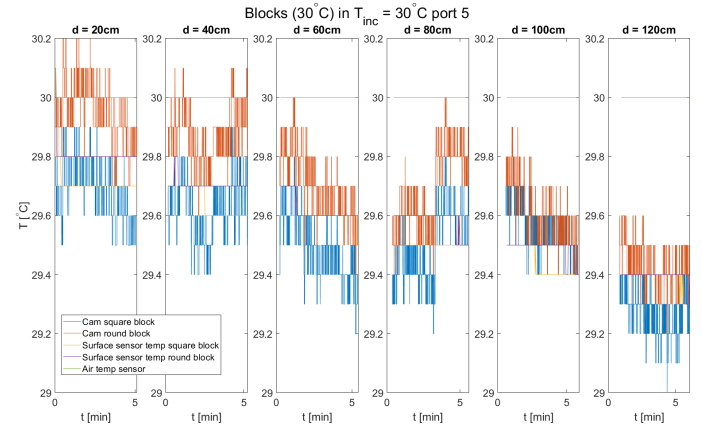


Figure 9.5: Measurement setup to measure the effect of the distance on measured temperature.

In Fig. 9.6 four figures of six graphs each can be seen. They correspond with the 4 different scenarios described above, i.e. Fig. 9.6a corresponds with scenario 1, Fig. 9.6b, data was no longer available for Fig. 9.6c, and Fig. 9.6d with scenario 4. Each graph in the figure corresponds to 5 minutes of measuring per distance. These measurements were also performed by covering the porthole through which was filmed with HDPE or LDPE. These graphs can be found in App. J.1 and J.2, respectively.

(a) Blocks (38°C) in $T_{inc} = 38^\circ\text{C}$ filmed through port 4.(b) Blocks (38°C) in $T_{inc} = 38^\circ\text{C}$ filmed through port 5.

(c) Missing data.

(d) Blocks (30°C) in $T_{inc} = 30^\circ\text{C}$ filmed through port 5.

Figure 9.6: Each set of four graphs depict the measurement difference between the camera and the temperature sensor per situation described above.

9.2.5. Opening Portholes

Opening portholes can disturb the internal thermodynamics of the closed compartment. The goal of this measurement was to gain an understanding of the effects such an event can have on the temperature measured by the camera. The camera was placed at $d = 30\text{cm}$ in front of a porthole, because this distance is equal to the distance most often used when filming neonates. One paperboard box was placed inside the incubator in front of porthole five and another similarly in front of porthole four with their bottoms facing the opened porthole. Similarly to Sec. 9.2.4, a temperature sensor was placed on the box using the hospital adhesive, and electrical tape was taped to the box, very close to the place where the temperature sensor was placed. In FLIR's QuickPlot, a measurement rectangle was drawn over the electrical tape, what can also be seen in Fig. 8.5. This similar practice was used in all measurements that follow.

The sensor on the box in front of porthole 5 was named *Sensor 1*, and the sensor on the box in front of porthole 4 was named *Sensor 2*. The measurement setup can be seen in Fig. 9.7.

This measurement was performed only without sealing the porthole with foil and for porthole 4 and 5, in contrast to the measurement where the porthole has been sealed with HD/LDPE. During the measurement the following procedure was followed:

1. Leave the incubator off for an entire night so that it is at room temperature.
2. Place the camera in front of the porthole through which will be recorded at $d = 30\text{cm}$ and open said porthole.
3. Turn on the incubator and set it to 28°C and start the recording.
4. After 15 minutes start logging the incubator sensor readout.



Figure 9.7: Measurement setup in RDGG during the measurement *Opening Portholes*. The box on the left was named Sensor 1, with the right box being named Sensor 2.

5. Open portholes 1 and 2.
6. After 15 minutes open the porthole next to the porthole through which the measurement is made. At this point 4 portholes are opened.
7. Stop the camera measurement, close all the portholes, and increase the incubator temperature by one degree celsius.
8. After 15 minutes open the porthole in front of which the camera is positioned and start recording with the camera again.
9. Repeat from step 5 up to and including $T_{inc} = 33$.

The result of such a measurement can be seen in Fig. 9.8. Fig. 9.8 requires some additional information. In this graph, three sensor values can be seen, the temperature from the IRT camera, and vertical lines indicating an event has taken place, i.e. a porthole was opened or closed. By looking at Fig. 9.8, it can be seen that the first 15 minutes depict step 3 in the measurement. After 15 minutes a green vertical line can be seen. This indicates step 4 and 5. Then 15 minutes later step 6, 15 minutes later step 7, etc., etc.

Additionally the percentage of power the heater was running at can be seen in Fig. 9.9. The red vertical lines indicate the same event as was described for Fig. 9.8. Similar graphs were created for porthole 4 and can be seen in App. I.



Figure 9.8: Visualisation of the effect of opening additional portholes on the temperature as measured by multiple sensors. The blue line depicts the temperature as measured by the IRT camera, the red and yellow line depict the values measured by the temperature sensors that are stuck to the paperboard boxes through hospital adhesives. The purple line represents the air temperature sensor, and the green vertical lines indicate an event.

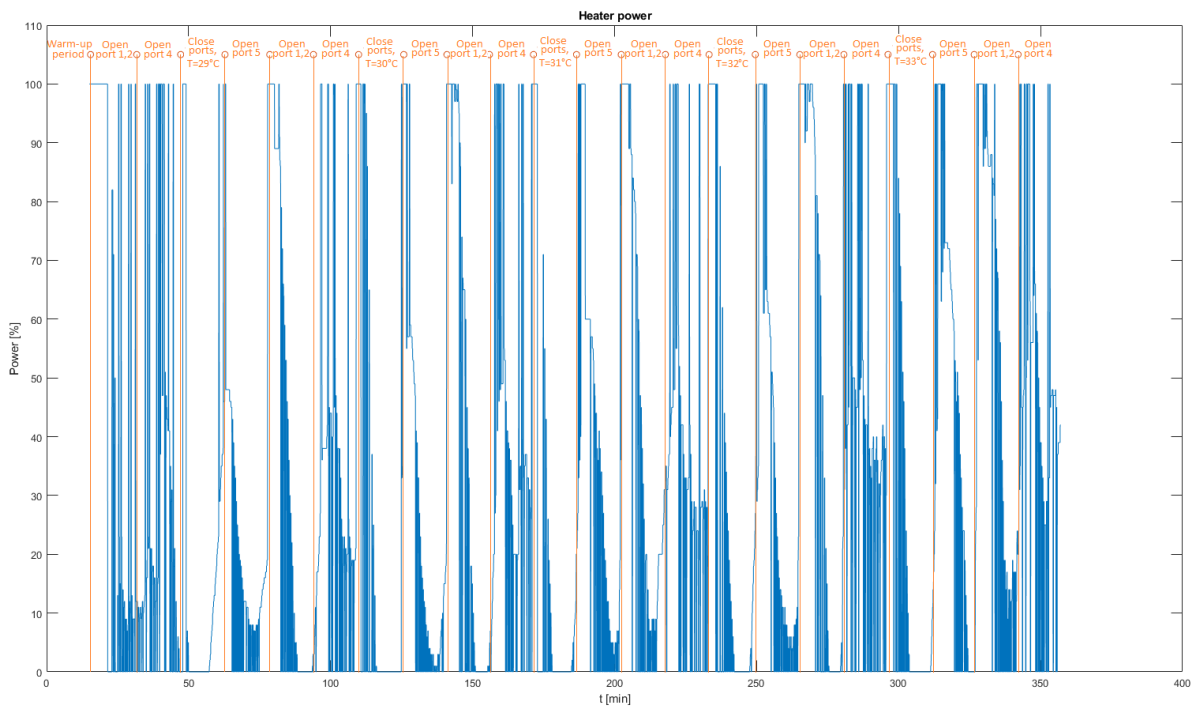


Figure 9.9: Heater power percentage during the *Opening Portholes* measurement. Blue line depicts the power percentage of the heater during the measurement. The red lines indicate the same event.

9.2.6. Airboost

The GE Giraffe™ Omnibed incubator has the option to enable a certain setting called *Airboost*. This is a setting in which warm air is blown from under the mattress at sides 1 and 2. This decreases the rate at which

the compartment cools down and prevents particles from coming in. The effect is called an *air curtain* [47] and is mainly intended to be used when the entire sides are open. This air curtain can have an effect on the temperature measured by the camera. Therefore a similar measurement as in Sec. 9.2.5 was performed.

This particular measurement was performed using the following procedure:

1. Leave the incubator off for an entire night so that it is at room temperature.
2. Place the camera in front of the porthole through which will be recorded at $d = 30\text{cm}$.
3. Turn on the incubator and set it to 28°C .
4. Wait 30 minutes for the incubator to warm up.
5. Start the airboost.
6. Open the porthole, start the recording and log the sensor readout.
7. After 15 minutes, open side side 1.
8. After 15 minutes, open side 2 too.
9. After 15 minutes close both sides, but leave the porthole open, and increase T_{inc} by 1 degree celsius.
10. Repeat steps 7 through 9 up to and including $T_{\text{inc}} = 33$

The airboost setting requires a lot of power and is therefore automatically disabled after 5 minutes. It was re-enabled every 5 minutes. If these steps are followed, a similar graph as in Fig. 9.8 is then created, and can be seen in Fig. 9.10. Similarly the heater power during airboost can be seen in Fig. 9.11.

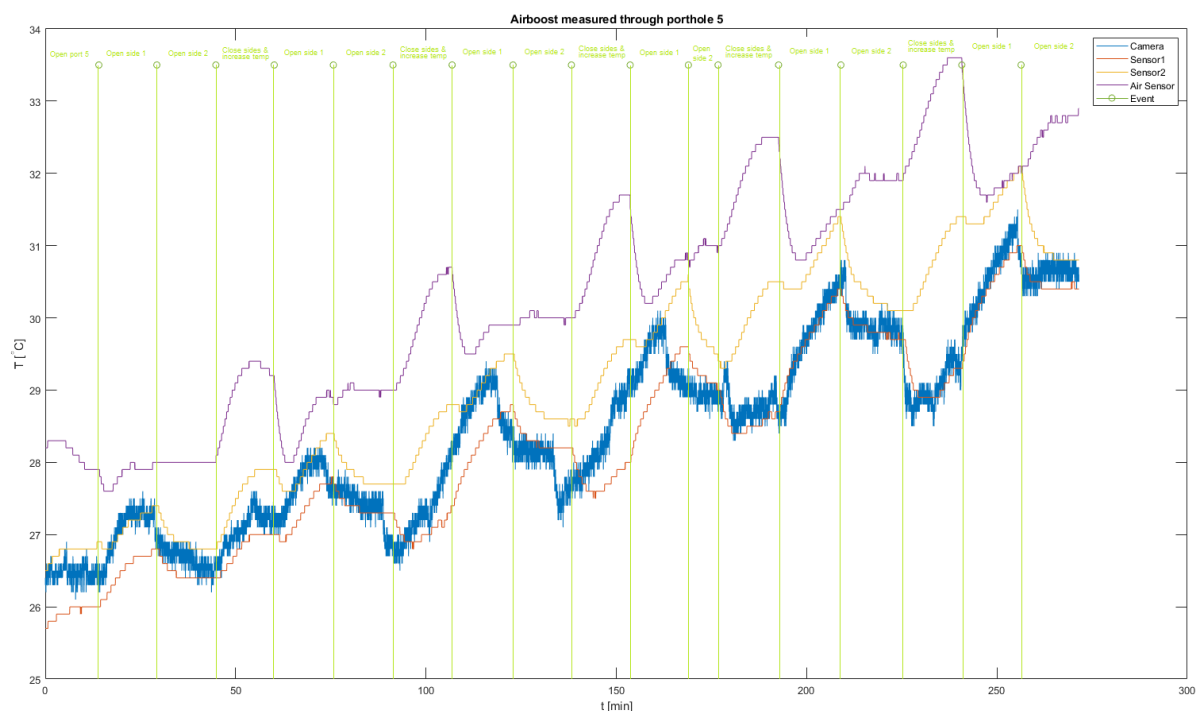


Figure 9.10: Visualisation of the effect of opening the entire sides during the airboost setting

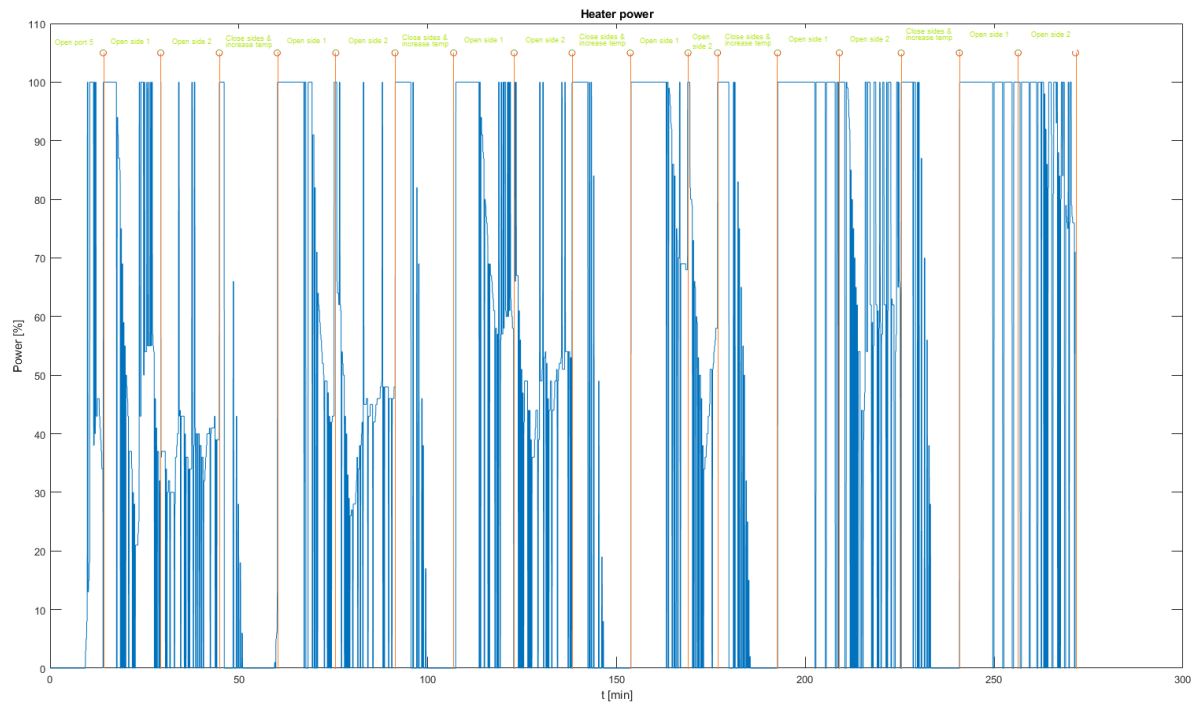


Figure 9.11: Heater power percentage during the *Airboost* measurement. Blue line depicts the power percentage of the heater during the measurement. The red lines indicate the same event.

9.2.7. Testo 890

A different IRT camera was borrowed from Dr. R. Delfos who is part of the Process and Energy department at the TU Delft. The camera in question was the *Testo 890*. This camera was used to compare at least two different brands of IRT cameras. This is necessary as each brand of IRT camera manufacturers implements their own model and equation to determine the temperature. Moreover, this camera has a resolution of 640x480, which is 4 times larger than the FLIR A305sc. A similar measurement as in Sec. 9.2.5 was performed, however rather than studying the camera's temperature from $T_{\text{inc}} = 28$ up to $T_{\text{inc}} = 33$, only one part of this range was recorded. The incubator had been warmed to $T_{\text{inc}} = 28$ for 90 minutes, starting from room temperature, and was then increased to $T_{\text{inc}} = 29$. At this point the recording was started, which can be seen in the graph. The camera was placed in front of porthole 5 without foil covering it, and the distance was $d = 30\text{cm}$. The resulting graph can be seen in Fig. 9.12.

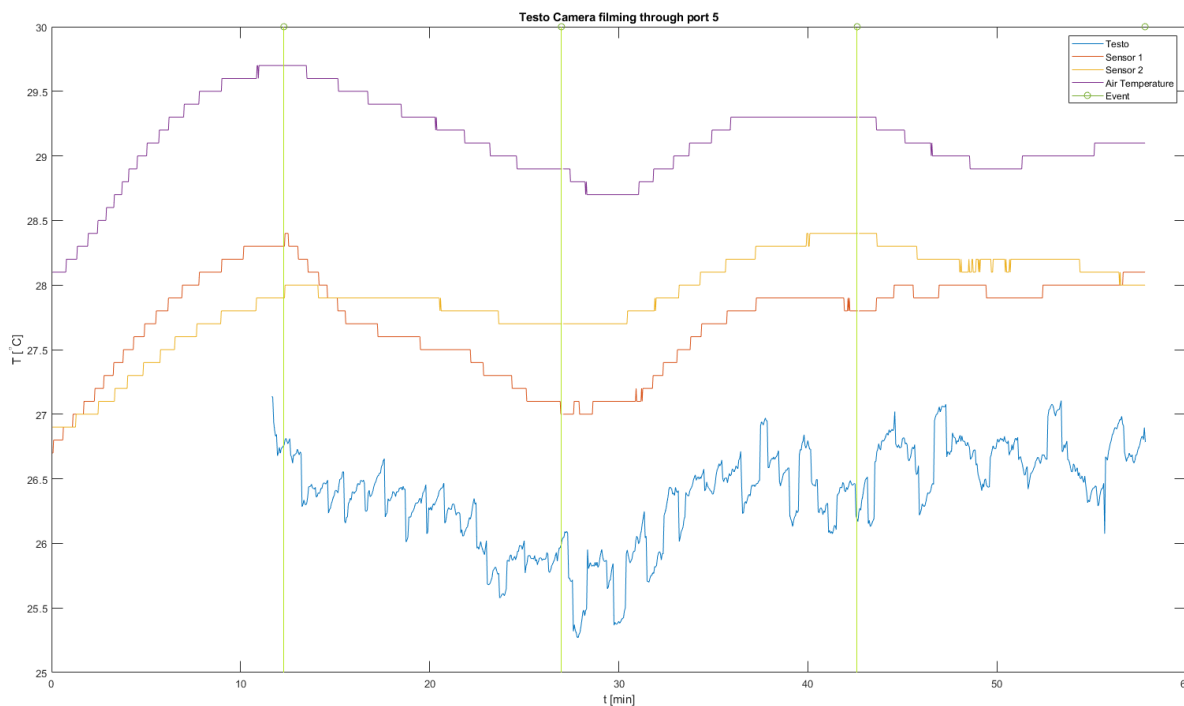


Figure 9.12: Temperature from the Testo 890 camera together with the temperature from the sensors on the paperboard boxes.

9.3. Neonatal Measurements

Recordings were also made on neonates. How the recording material, e.g. a laptop and camera, was set up can be read in Sec. 8.3. One frame from an IRT recording from two different neonates can be seen in Fig. 9.13.

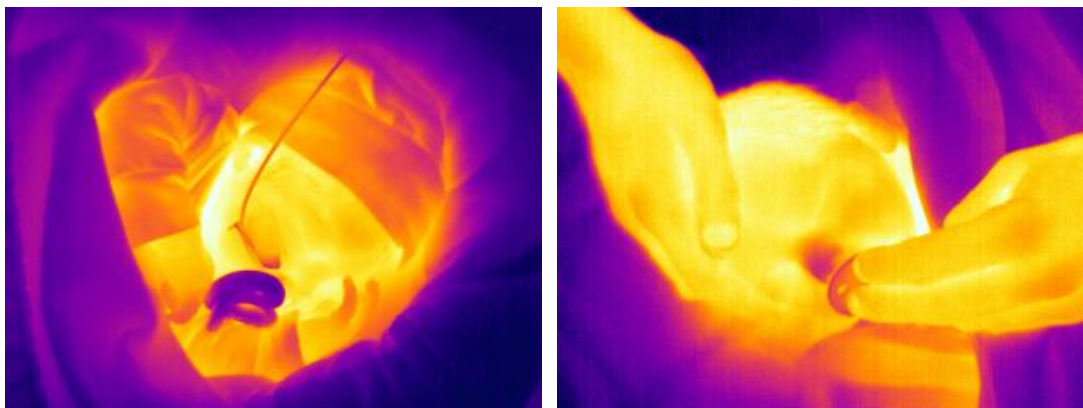


Figure 9.13: Two thermograms of two different neonates that were filmed.

Unfortunately, the IRT recordings were part of the material that the researcher no longer is able to access. However, the skin temperature sensor was also logged during these measurements. The graphs that were made of this sensor readout can be seen in Fig. 9.14.

As described in Sec. 9.2, there are at least two different methods to place a temperature sensor on a neonate's skin. Multiple neonates were measured with two different methods of adhesion to determine whether the method of adhesion influences skin temperature measurements. These temperature sensor values yield a reference value for the IRT camera. The sensor was placed on the body part where nurses are used to place the sensor, i.e. above the hip on the stomach under the diaper. After consulting with the nurse assigned to a neonate, they agreed to place a temperature sensor on the neonate such that the sensor was partially covered. After half an hour the sensor adhesive was changed to be fully covered. All these neonates were fully dressed. For one neonate (jkzD) the location of the temperature sensor was changed due to their

clothing, where it was placed on the groin.

Additionally a measurement was performed on a neonate that had received a temperature sensor from a caregiver on the side it was lying on. After half an hour it was moved to the side it was not lying on. This can be seen in Fig. 9.14h. As expected, the temperature is higher when the neonate is lying on top of the sensor.

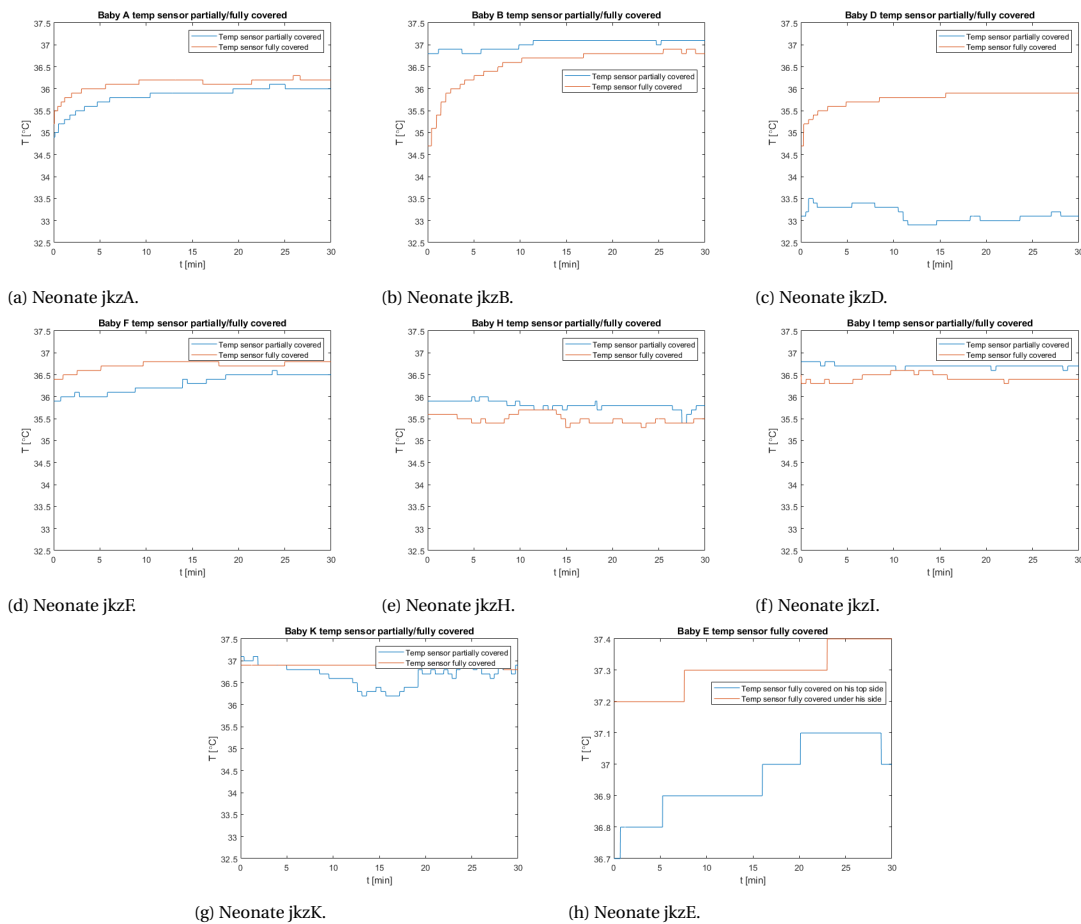


Figure 9.14: Temperature per neonate measured by the temperature sensor.

9.4. Conclusion

Several different parameters, e.g. the RAT and τ_{opt} , were determined that are used to perform accurate measurements. Once these parameters were established, the IRT and thermistor measurements were compared against a calibrated Pt-100 temperature sensor. A measurement was performed to determine whether the atmospheric losses determined in Chapter 6 are actually negligible. Finally a multitude of experiments were conducted using IRT which simulated the real life scenarios in which an incubator could be used. These include placing two pieces of aluminium inside the incubator, measuring their temperature using IRT, and using an NTC taped to each of the aluminium pieces. This was repeated at two different different temperatures ($T = 30^\circ\text{C}$, $T = 38^\circ\text{C}$) at several distances, through different portholes. Another measurement a cardboard box that was placed inside the incubator, and its temperature was measured through one porthole, both via IRT and a NTC thermometer. Over the course of three hours, the temperature was raised from $T = 28^\circ\text{C}$ to $T = 33^\circ\text{C}$, and several portholes were opened to see the effect of this on the measured temperature.

10

Result Interpretation & Discussion

This chapter will discuss the results that were obtained in Chap. 9. Per experiment the results will be discussed in detail, along with potential improvements that could have been performed.

10.1. IRT Behaviour During Incubator Measurements

10.1.1. External Optic Window

Any material that can seal the incubator and pass through IR radiation can be used to create an external optic window. Polyethylene was chosen because a study found that neonates wrapped in PE experienced reduced heat loss [108]. Another added bonus is that PE can easily be purchased at construction stores, or online. For this thesis, two rolls of foil were purchased: HDPE roll 2x100m (200m²) for €8,32, and LDPE roll 50mx2m (100m²) for €14,12. The surface area that had to be cut out to fully cover a porthole would approximate 20x15cm (0.03m²), which means that one such piece of HDPE would cost approximately €0.0012. For LDPE this amounts to €0.0042. It should be noted that this roll of LDPE was 4.28 times thicker and thus more expensive. After normalising this to the same thickness as HDPE, it would cost €0.00099 per piece of 0.03m².

Transmissivity

FTIR was used to determine the transmissivity of both HDPE and LDPE. These measurements were performed using 1 sheet and multiple sheets placed on top of each other. This was done in case the nurses/physicians of the hospital would not agree that an opened porthole was sealed with foil less than a millimeter thick.

In Sec. 3.5.3, the transmissivity and reflectivity of HDPE were given, and the transmissivity of LDPE. In Fig. 9.2a a strong resemblance in the range of 7.5-13 μ m can be found. However, a peak with decreased transmissivity is found at approximately 11.5 μ m, which is not found in literature. Additional steep peaks with decreased transmissivity around 3.5 μ m and 7 μ m correspond to the literature. For $\lambda < 7.5\mu$ m, a lower transmissivity is found, whereas for $\lambda > 17\mu$ m a transmissivity higher than in the literature is found.

For LDPE, wider peaks can be seen around 3.5, 7, and 14 μ m. Luckily these lie outside the range in which the camera functions. However, a peak found at 11.5 μ m is not visible in the literature. Moreover, the highest value the measured transmissivity reaches is $\tau = 0.8$. In the literature it hovers around $\tau = 0.9$.

Discussion

These two types of foil are designed to be used at construction sites and to be handled roughly. It does not matter if this material is not pure H/LDPE, as long as it is able to fulfil its designed task, which is to cover construction material. Perhaps it has been contaminated by different molecules which block IR radiation. Another explanation could be that the material had to be handled, (cut out, placed on the setup, etc.) by the researcher prior to a measurement, which means finger prints could have stained the material. By placing more sheets on top of each other, a similar curve is created for both HDPE and LDPE, albeit attenuated.

10.1.2. RAT

Two tables have been filled with RAT values per temperature and per porthole of the incubator. In Fig. 10.1a and 10.1b the RAT per incubator has been visualised. In each graph a smoothing curve through the points was

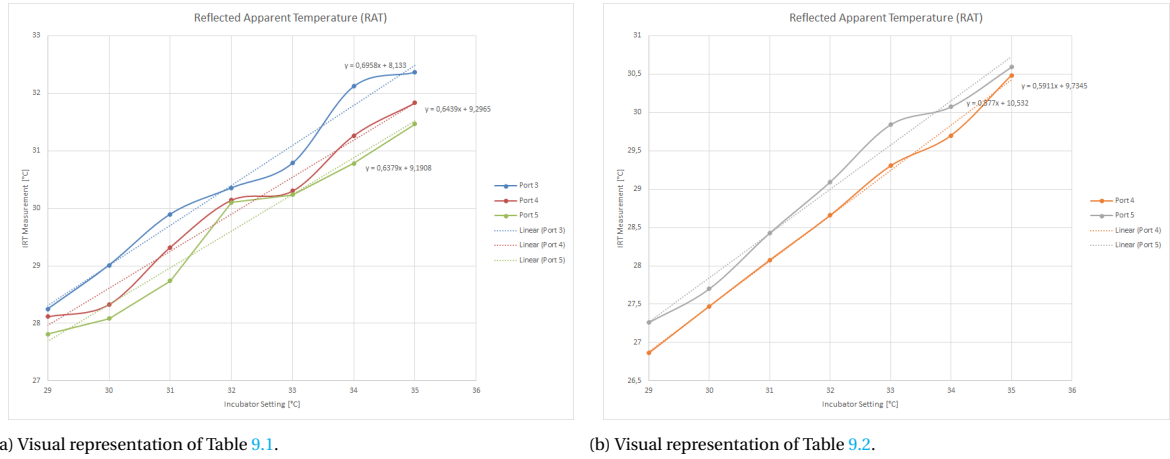


Figure 10.1: The RAT per incubator type per porthole.

added and a linearisation of the points. Each measured temperature point per will be denoted as: $T_{RAT,inc,n}$, inc : incubator type (GE/Caleo), n : porthole through which was measured.

Fig. 10.1a contains an extra curve as the GE GiraffeTM Omnibed contains porthole 3, whereas the Dräger Caleo[®] does not. In essence, the RAT is the summed reflecting radiation upon the object in question. This means that an increase in temperature in sources that contribute to the RAT, will yield an increase in the RAT. Analogous to this is, an increase in surface area will increase the RAT. A combination of these two factors will increase the RAT even further. Fig. 10.2 shows the surfaces that reflect upon the piece of aluminium during the measurement. This is a top-down view, which does not show the top of the canopy.

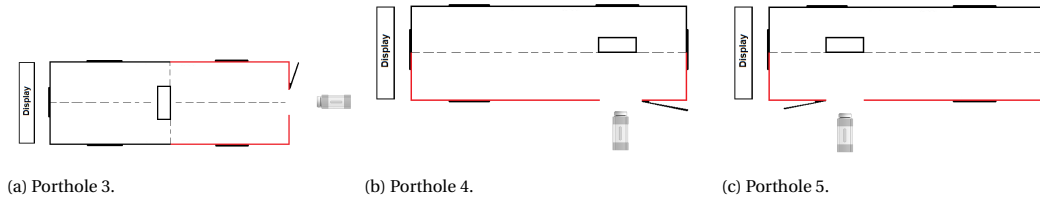


Figure 10.2: Surfaces that affect the RAT. The red lines depict sources that contribute to the RAT for the respective camera position.

Fig. 10.3 depicts the difference of the RAT per incubator, i.e. $RAT_{GE} - RAT_{Caleo}$. Similarly a smoothing curve was plotted through the measurement points and a linearisation was added.

From Fig. 10.1a and 10.1b, it can be seen that $T_{RAT,inc,3} > T_{RAT,inc,4} > T_{RAT,inc,5}$.

Dimensions of the incubators can be found in Sec. 3.5. No dimensions of the canopy were measured, thus an approximation will be made based on the dimensions of the mattress inside. This can be found in the user manual: 64.5x50cm [35]. The heights of the canopy are not given in the user manuals hence no accurate area calculation can be made, but based on these approximations, the total surface area of the reflection radiating sources will be approximately equal. For porthole 3 this amounts to: $2 \cdot (\frac{1}{2} \cdot 64.5) \cdot h + (50 - 20) \cdot h = 94.5 \cdot h$ versus $2 \cdot (\frac{1}{2} \cdot 50) \cdot h + (64.5 - 20) \cdot h = 94.5 \cdot h$ for porthole 4 and 5, where h is the canopy height, and 20 is subtracted due to the open porthole.

A possible explanation of why $T_{RAT,GE,3}$ is consequently higher could be due the fact that, when looking at the distance from the middle of the box to the canopy wall, the box sees contributing reflection sources more closely for the larger part, than for $T_{RAT,GE,4}$ and $T_{RAT,GE,5}$. In other words, canopy walls to the side of the box are overall closer to it for $T_{RAT,GE,3}$ than for $T_{RAT,GE,4}$ and $T_{RAT,GE,5}$. Seeing how temperature decays exponentially, this could explain why $T_{RAT,GE,3}$ is consistently larger. Additionally, $T_{RAT,GE,4} > T_{RAT,GE,5}$. In these two situations, the contributing radiating reflection sources are at equal distances. The only difference is the material. In Fig. 3.8a and 3.8b, it can clearly be seen that the canopy of the GE GiraffeTM Omnibed is not uniformly made of the same material. However, the entire canopy of the Dräger Caleo[®] is uniformly made of the same material, yet still $T_{RAT,Caleo,4} > T_{RAT,Caleo,5}$. By looking at Fig. 10.3, it can be seen $T_{RAT,GE,n} > T_{RAT,Caleo,n}$. An explanation could be that between the two types of incubators, the air temperature sensor differs in quality. Another explanation could be that the airflow is different for each incubator.

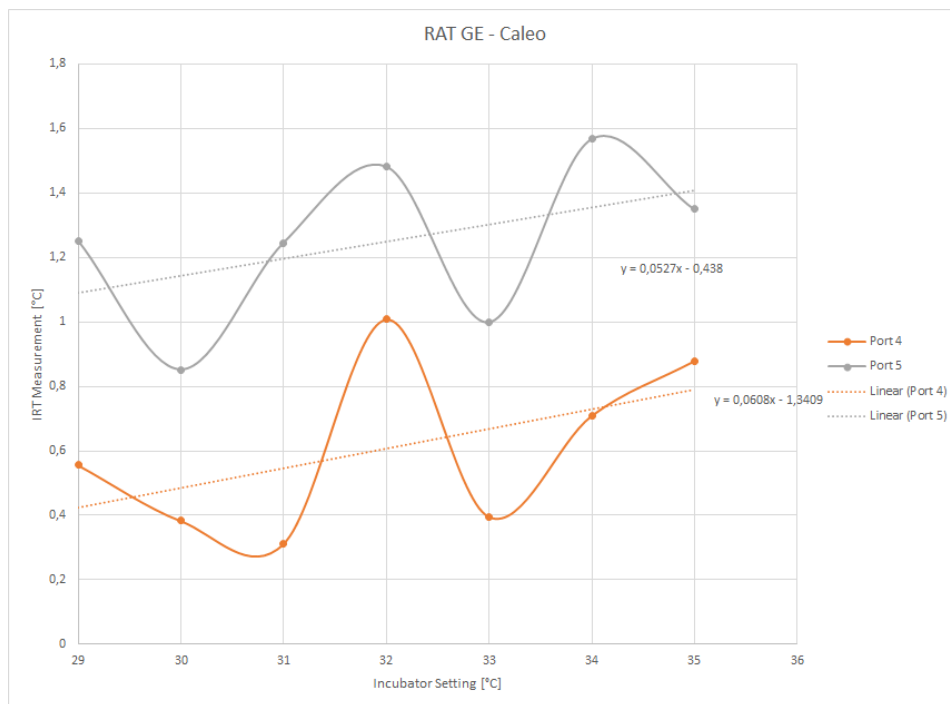


Figure 10.3: GE - Caleo RAT.

Discussion

The boxes were placed on the perpendicular line to the camera, in the middle of the incubator, behind the open porthole. They could perhaps have been placed in such a position that it would correspond with the location of a body part of a neonate. This means placing the boxes more forward, backward, left, or right. It was chosen to take the middle position so that the average RAT is determined. A follow up measurement could be to do these measurements again, but by placing the boxes at different locations through the incubator. This would change the surfaces that radiate upon the object, and thus change the RAT.

A different piece of crumpled and uncrumpled aluminium paper was used for each incubator RAT measurement. This piece of aluminium paper will never uncrumple equally, thus the piece is different per measurement and could influence the amount of reflected radiation. An average was already taken over the surface, which should counteract this effect.

As the task turned out to be very time consuming, this measurement was only performed once. To reduce the variation, multiple measurements can be performed and averaged.

10.1.3. Accuracy GE Temperature Sensor

In order to determine the accuracy of the temperature sensors used in the hospital, a calibrated Pt-100 temperature sensor was used from manufacturer Thermo Electra. Its certificate of calibration can be found in App. K. The type of multimeter that was used can no longer be traced back, but it was borrowed from the microelectronics department of the TU Delft. A 4-wire resistance measurement was performed.

Four different temperatures were measured, namely the temperature of the Pt-100 (as calculated by the relation in App. K) inside the aluminium block, a GE Giraffe™ Omnibed temperature sensor inside the aluminium block and one on the surface (stuck to it using the same adhesive that is used to keep the sensor on the neonate), and the IRT camera temperature.

In Fig. 9.4b, it can be seen that the GE sensor placed in the aluminium measures 27.1°C consistently for 15 minutes. The Pt-100 hovers slightly above that. Such thermistors have an accuracy of $\pm 0.1^\circ\text{C}$, which means that the GE sensors measures a correct value. The GE sensor on the surface of the aluminium measures a slightly lower temperature, which corresponds to the situation when comparing core temperature and skin temperature.

As for the camera, it averages approximately 24.4°C, which is 0.8°C degrees higher than the GE sensor on the surface of the aluminium.

Discussion

A slightly declining line of the Pt-100 sensor can be witnessed. This could be because a different measurement was performed prior to this. However, an hour passed before this measurement was done, which should have been adequate to cool the aluminium to room temperature. It could be said that if longer was waited, the measured temperature would have kept declining to a value $T < 23.6$. This would have yielded an error of the GE sensor larger than its standard deviation, namely $\pm 0.1^\circ\text{C}$. This is highly unlikely, seeing the rate of the decline and the amount of time that had already passed.

Two things can be said by reading the certificate of calibration of the Pt-100 sensor. Firstly, the sensor has been calibrated in May 2017. The measurement was performed on 8-6-2019, more than two years later. This could have influenced the measurement. However, when comparing it to the GE sensor, it seems to have yielded appropriate results. Secondly, it is given that the immersion depth should be at least 25cm. This was not the case for this measurement. An aluminium block that size was not available. Additionally, making a hole for the sensor at the depth it was at currently already proved challenging, let alone drilling 25cm. However, not adhering to the requirements can negatively influence the measurement.

Lastly, a measurement where the temperature was varying could have given more insight.

10.1.4. Changing the Distance from Camera to Incubator

In Fig. 10.4, six sets of four plots can be seen, where each plot depicts the difference between the temperature sensor on an aluminium block and the temperature measured by the IRT camera, i.e. $T_{\text{sensor}} - T_{\text{camera}}$, on the y-axis, and the difference points per distance d on the x-axis. During the measurement, a recording was made that lasted 5 minutes. The camera recorded at 9Hz, which yielded $9 \cdot 60 \cdot 5 = 2700$ points. However, in Fig. 9.6, not each graph exactly starts at 0 minutes, or ends at 5. This is due to the researcher having to manually stop multiple active measure windows, which may have caused some misalignment. It was chosen to depict the start of all measurement signals at the first measurement point of the measurement signal that started recording last. Similarly, the end of all measurement signals has been synchronized to the measurement signal that was stopped first. This does mean that some data at the beginning and end of a signal have been cut off.

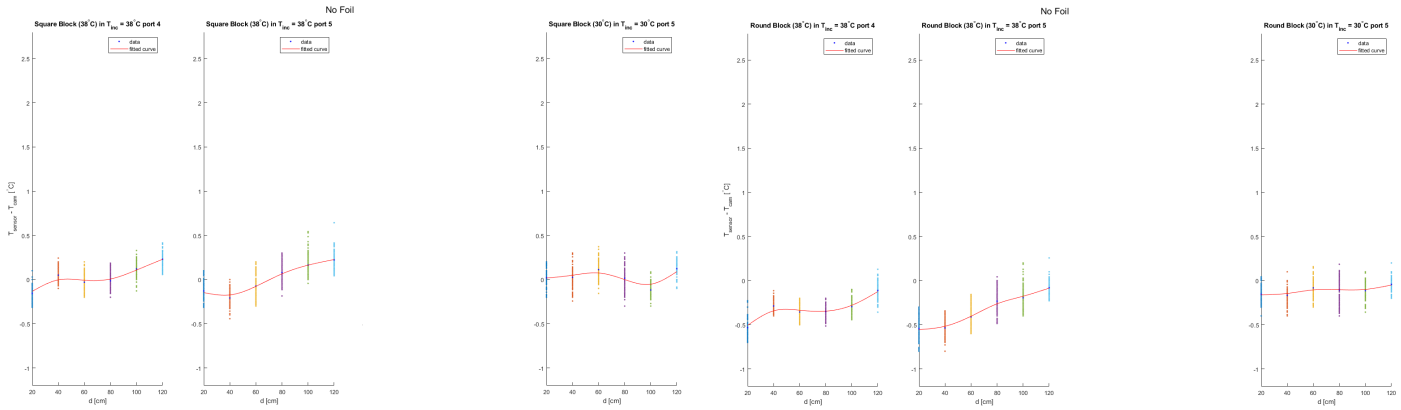
An analysis per scenario will be made. However, T_{atm} requires no analysis per scenario, as it can be seen that $T_{\text{atm}} = T_{\text{set}}$ within the specified tolerance, where T_{set} is the set incubator temperature.

1. The aluminium blocks have spent the entire night in the incubator at $T_{\text{set}} = 38^\circ\text{C}$ in the position the measurement will be performed. The sensors needed to be attached to each block on the next day, prior to the measurement, which has been the only outside interference these blocks experienced. For each distance $T_{\text{sensor}/\text{cam},\text{round}} > T_{\text{sensor}/\text{cam},\text{square}}$. Additionally a gradual decrease in $T_{\text{cam}/\text{sensor}}$ can be seen, i.e. $T_{\text{sensor}/\text{cam},d20} > T_{\text{sensor}/\text{cam},d120}$. T_{atm} is greater than all other signals for all d , except $d = 20$. At $d = 20\text{cm}$, $T_{\text{cam},\text{round}} > T_{\text{atm}}$.
2. The setup was prepared exactly as described in scenario 1. Nearly all signals behave identical to the previous scenario, except that $T_{\text{cam},\text{round}} \geq T_{\text{atm}}$ for $d = 20, 40, 60\text{cm}$.
3. The block was heated overnight in an incubator set to $T_{\text{set}} = 39^\circ\text{C}$. The incubator with which the measurement would be performed was turned on an hour prior to the measurement to heat the incubator to $T_{\text{set}} = 30^\circ\text{C}$. The aluminium blocks were transported in covers to prevent heat loss. They were placed in the same position as the previous scenarios. For each distance $T_{\text{cam},\text{square}} > T_{\text{cam},\text{round}}$ and $T_{\text{sensor},\text{square}} > T_{\text{sensor},\text{round}}$. Additionally a decrease in measured temperature for both the camera and the sensors can be seen, i.e. $T_{\text{sensor}/\text{cam},d20} > T_{\text{sensor}/\text{cam},d120}$. T_{atm} is smaller than all other signals.
4. The setup was prepared exactly as described in scenario 1, with $T_{\text{set}} = 30^\circ\text{C}$. A similar trend can be seen where T_{cam} and T_{sensor} decline as distance increases. $T_{\text{sensor},\text{round}} \geq T_{\text{sensor},\text{square}}$ with a decreased $T_{\text{sensor},\text{round}} - T_{\text{sensor},\text{square}}$ compared to scenario 1, 2, and 3. Similarly, $T_{\text{cam},\text{round}} \geq T_{\text{cam},\text{square}}$ with a decreased $T_{\text{cam},\text{round}} - T_{\text{cam},\text{square}}$ compared to scenario 1, 2, and 3. T_{atm} is greater than all other signals for all d except for $d = 20, 40\text{cm}$ where $T_{\text{cam},\text{round}} \geq T_{\text{atm}}$.

All scenarios follow the same pattern: a gradual decrease in measured temperature for both the camera and the sensors, i.e. $T_{\text{cam}/\text{sensor},d20} > T_{\text{cam}/\text{sensor},d120}$, in all scenarios, albeit not at equal pace. This is explained by the fact that warm air from inside the incubator will flow outside, and cold air from the outside environment ($T_{\text{room}} = 23$) will flow inside in an attempt to attain thermal equilibrium.

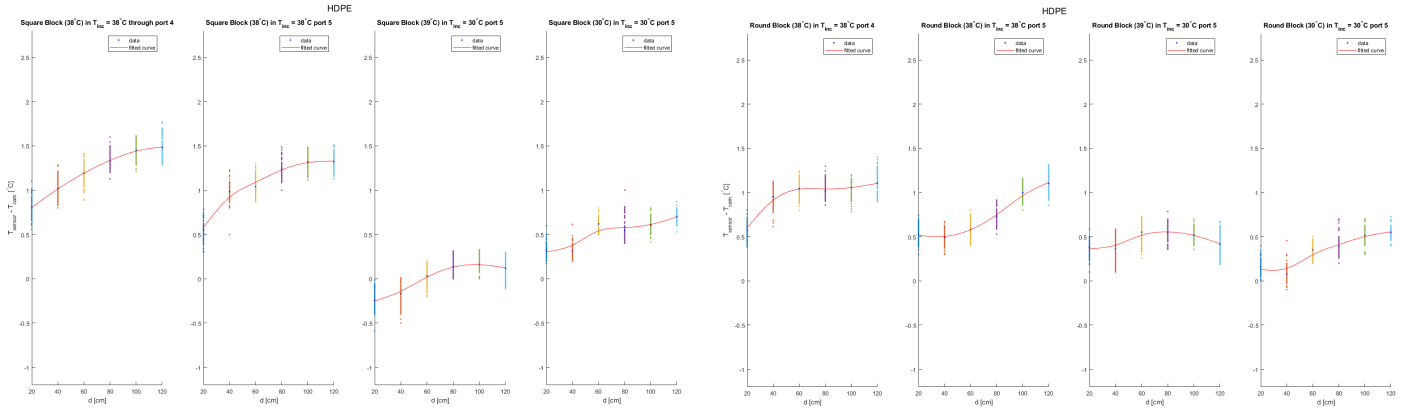
One odd interaction is scenario 3. In this scenario $T_{sensor/cam,square} > T_{sensor/cam,round}$, whereas in all other scenarios this is reversed.

Of interest is the difference in measured temperature from the camera and the thermistor, i.e. $T_{sensor} - T_{cam}$, also known as the error e . This has been plotted in Fig. 10.4. The average of 18 consecutive points measured by the camera was taken. This was done due to two different sampling frequencies: the sensors (0.5Hz) and camera (9Hz). Because per distance a period of time was recorded, multiple points per distance are created. The red curve is a smoothing spline which was run through the black points, i.e. the average of the points per distance d . Measurements 1 through 4 performed without foil using the square and cylindrical aluminium block can be seen in Fig. 10.4a, and 10.4b, respectively. The same was done using LDPE and HDPE and can be seen in Fig. 10.4c, 10.4d, 10.4e, and 10.4f, respectively. Due to the missing data in Sec. 9.2.4, four graphs will also be missing in this section.



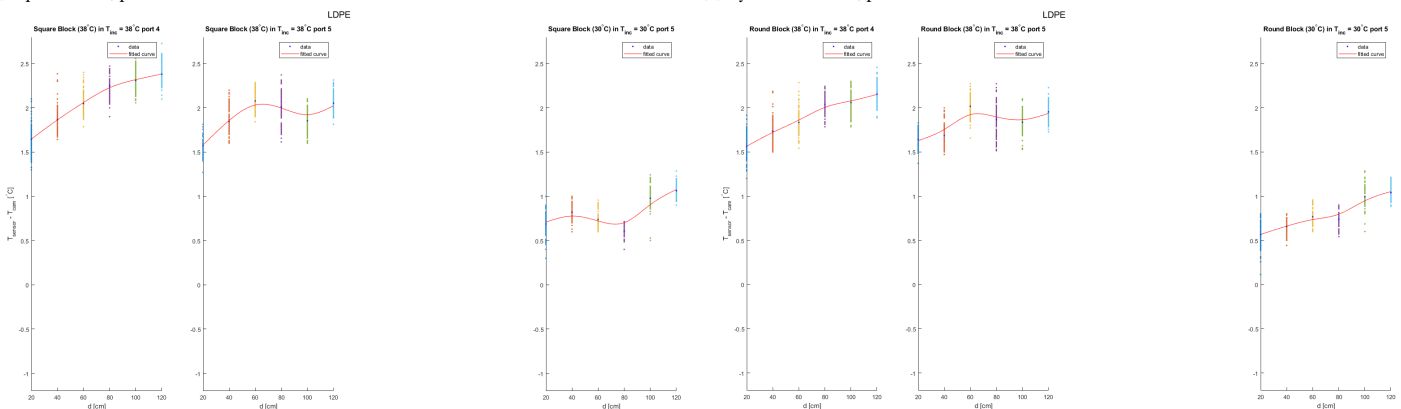
(a) Square block, porthole not covered with foil.

(b) Cylindrical block, porthole not covered with foil.



(c) Square block, porthole covered with HDPE.

(d) Cylindrical block, porthole covered with HDPE.



(e) Square block, porthole covered with LDPE.

(f) Cylindrical block, porthole covered with LDPE.

Figure 10.4: Each set of four graphs depicts the measurement difference between the camera and the temperature sensor per situation described above.

By looking at Fig. 10.4a and 10.4b, it can be seen that the average absolute error over a timespan of 5 minutes per distance fluctuates around 0, but is smaller than 0.6°C for scenarios 1, 2, and 4, i.e. $|e| < 0.6^{\circ}\text{C}$. After inspecting scenarios 1, 2, and 4, for both the square and round aluminium piece, it can be seen that scenario 1 follows the same curve, but at a lower value of e . This holds for scenario 2, 4, for both the square and round aluminium piece, as well. This means a larger difference between T_{sensor} and T_{cam} for the round block. According to literature this should be reversed, due to the loss of radiation because of the curved shape of the aluminium block. An explanation could be that the location of the round block is warmer than that of the square block. Perhaps colder air flows past the square block.

We will now consider the situation in which HDPE was used in Fig. 10.4c and 10.4d. An increase in absolute error is witnessed for scenarios 1, 2, and 4 square, compared to when no foil is used, i.e. $T_{\text{sensor}} > T_{\text{cam}}$. For scenarios 1, 2, and 4 round a similar increase in error can be seen, following the same relationship with the square block as described in the situation without foil. The error also has increased for scenario 3, with a decrease in absolute error for square, and similar absolute error for round, albeit that $T_{\text{cam}} < T_{\text{sensor}}$.

Finally, the situation in which LDPE was used in Fig. 10.4e and 10.4f. An increase in absolute error is witnessed for scenarios 1, 2, and 4 square, compared to when HDPE is used, i.e. $T_{\text{sensor}} > T_{\text{cam}}$. For scenarios 1, 2, and 4 round a similar increase in error can be seen, following the same relationship with the square block as described in the situation without foil.

Discussion

For the sake of confirming that the distance up to 1.2m does not influence the temperature measured by the camera, the performed experiments are inadequate. They can not distinguish between the reason a temperature dropped, i.e. opening a porthole lets in cold air, which cools the object, and simultaneously the camera was moved backwards. Both could have contributed to a decrease in temperature. A better approach would have been to place both aluminium blocks in the incubator at a temperature that is used most commonly for neonates, e.g. $28 \leq T_{\text{set}} \leq 33$, have it turned on at this temperature during the night with the porthole through which will be measured *open*. Keeping the porthole opened will eventually place the system in an equilibrium and radiation equal. By changing the distance at which is recorded will then provide a meaningful result. The last scenario could have been such a measurement, had the system been given time to reach an equilibrium. However, it should be noted that theoretically distance should not influence the measured temperature.

The RAT was determined up to 35°C in the corresponding experiment, but a linearisation was derived, which was used to derive the RAT for $T_{\text{set}} = 38^{\circ}\text{C}$.

What can be taken from this experiment is that, at higher temperatures of T_{set} , the difference between camera and sensor is increased when foil is used. Perhaps the transmissivity of the foil was not determined correctly, or the RAT could not be derived as was assumed, and should thus be determined experimentally.

A situation in which the target temperature is higher than its background, should yield lower absolute error values. This is in agreement in scenario 3 HDPE, which is in agreement with the literature. A comparison between the other two scenarios would have been preferred, but it can be assumed that the error for the situation without foil will be lower, which would have resulted in a lower absolute error, whereas in the situation with LDPE the error would probably have been higher, with a corresponding higher absolute error. This is due to imperfect determination of the transmissivity of the optic window. Another confirmation is that the absolute error increased for situation 1, 2, and 4 without foil, with HDPE, and with LDPE respectively.

Ultimately, the camera measures within its specified accuracy. According to the datasheet, the accuracy of the camera is $\pm 2^{\circ}\text{C}$ or $\pm 2\%$ of reading, whichever is largest. In the situation without foil, this is never exceeded. It is, however, exceeded in the situation with LDPE, which could indicate a wrongfully determined transmissivity.

10.1.5. Opening Portholes

Opening portholes is something that occurs every time a physician or nurse has to provide care to a neonate. As such it is important to determine the effects of opening portholes. In Fig. 9.8, this is visualized, with the heater power percentage in Fig. 9.9. Globally, four phases can be distinguished:

1. Opening port 5.
2. Opening port 1 and 2.
3. Opening port 4.

4. Closing all ports and increasing the temperature.

For $0 \leq t < 15$, the incubator was allowed a warm-up period, during which the sensors were not yet read out. During this time porthole 5 was kept open and is seen as phase 1.

Phase 2 starts at $t = 15$, portholes 1,2 are opened, and logging of the sensors started. T_{atm} shows a steep decline, indicating it had reached a temperature $T_{atm} > 28^\circ\text{C}$. During this phase, the heater power is at 100%, to counteract this sudden drop in temperature. $T_{sensor1,2}$ show a short moment of plateauing, after which they, and T_{atm} , increase to $T_{set} = 28^\circ\text{C}$. This corresponds to the heater turning off, only to be turned on to 80% shortly after. To maintain $T_{atm} = T_{set}$, the heater alternates between 100% and 10% for the rest of this phase. $T_{sensor1,2}$ surpass T_{set} , whereas T_{atm} plateaus at T_{set} . Meanwhile, T_{cam} shows similar behaviour to $T_{sensor1,2}$, albeit $T_{cam} = T_{sensor1,2} + a$, with a being an offset. This would suggest little influence of opening port 1 and 2, which can be explained by the fact that they are on the other side of the box.

Finally, porthole 4 is opened and phase 3 is started. For the first two thirds of this section, all sensors follow a similar temperature decreasing pattern, with $T_{cam} = T_{sensor1,2} + a$ only to increase for the final part. The heater power follows a similar alternating pattern as for the previous phase. This can be explained by the fact that $T_{atm} \approx T_{set}$, which does not require full power to maintain.

At $t = 45$ phase 4 started. All ports were closed and T_{set} increased so that $T_{set} = 29^\circ\text{C}$. This meant no logging of T_{cam} . A near vertical incline is visible in T_{atm} and overshoots $T_{set} = 29^\circ\text{C}$. This corresponds with the heater power providing 100% power up until the point where $T_{atm} > T_{set}$, after which the heater power switches off, to ramp up to 100% over the course of minutes once T_{atm} starts dropping. $T_{sensor1,2}$ increase at a slower rate, and start decreasing once T_{atm} starts decreasing.

At this point, one complete cycle had been measured, and phase 1 of a new cycle is started. Port 5 was opened and T_{cam} could be logged again. T_{atm} and $T_{sensor2}$ follow a similar pattern. They show a slight increase up until half of this phase, and then show a decrease to their value at the start of this phase. This can be seen by a U-shaped power curve. 100% power enables T_{atm} to increase, but decreases when the power is at its minimum, to which the power reacts by gradually providing more power. This would suggest that both T_{atm} and $T_{sensor2}$ experience little change by opening porthole 5 at this temperature. T_{cam} and $T_{sensor1}$ show a steep decline over the first few minutes, with a continuous less steep decrease over the remainder of this phase.

Once more port 1 and 2 were opened. All temperatures increase, except for an initial drop in T_{atm} , which is counteracted by the heater providing 100% power. Once T_{atm} starts increasing, the heater power gradually declines. This does seem to confirm the hypothesis that opening portholes 1 and 2 has little to no effect on $T_{cam,sensors1,2}$, due to the position of these sensors with respect to portholes 1 and 2.

To conclude this phase, port 4 is opened. A slight drop is seen in T_{atm} , and an even smaller drop in $T_{sensor2}$. This is corrected by the heater by providing a similar heater power pattern as in the same phase one cycle earlier, i.e. when port 4 was opened during $T_{set} = 28^\circ\text{C}$. At this point all ports are opened, which presents an opportunity for an increase of in-flowing cold air. This can be seen in a drop in $T_{sensor1}$, which is not shared by T_{cam} .

Two phases of the graph have thus far been explained. The following phases follow a similar behaviour as was described for $T_{set} = 29^\circ\text{C}$, albeit slightly exaggerated per increase in T_{set} .

Overall, it can be seen that initially $T_{cam} > T_{sensor2}$ during $T_{set} = 28^\circ\text{C}$, or $T_{cam} - T_{sensor2} > 0$. The same holds for the second phase $T_{set} = 29^\circ\text{C}$, but during the second phase of $T_{set} = 30^\circ\text{C}$, i.e. when port 5 is opened $T_{cam} - T_{sensor2} < 0$. For $T_{set} = 31, 32, 33^\circ\text{C}$ the same holds, i.e. $T_{cam} - T_{sensor2} < 0$. Additionally, for each temperature increase, $T_{sensor1} - T_{sensor2}$ becomes smaller. One explanation could be at higher temperatures more hot air flows out, and more cold air flows in, due to a higher temperature difference. The zeroth law of thermodynamics states that every system attempts to maintain thermal equilibrium, and at higher temperature differences, heat transfer is larger than at lower temperature differences. This increase in cold air flowing in corresponds with an increasingly deep drop once portholes 5 and 4 are opened. The decrease in $T_{sensor1} - T_{sensor2}$ would suggest that most cold air flows in through porthole 5.

Another notable feat is how $T_{cam,sensor1}$ is approximately the same during the opening of porthole 5 at the new increased temperature, as it is during the last phase of the previous cycle, i.e. when port 4 was opened during $T_{set} = (T_{set} - 1)^\circ\text{C}$. This does not hold for first phase and could be explained by a differently behaving warm-up period.

Discussion

By comparing Fig. 9.8 and Fig. 9.9, it would seem that the heater power reacts to the value of T_{atm} compared to T_{set} . The heater power was automatically logged during the temperature sensor readout, but it could have its use in correcting IRT temperatures. When the heater provides power, warm air flows into the incubator. This could have an effect on the error, i.e. $T_{sensor} - T_{cam}$ instantly, but also later when the sensor measures a warmer object, but the heater no longer blows in hot air.

Increasing temperature was performed with the porthole closed. Perhaps another measurement should be performed with the porthole opened at all times, as this will more than likely be the real life scenario. It does not mean that this experiment is not valuable. Suppose a child suddenly experiences a rapid drop in temperature, all portholes should be closed to prevent any cooler room air flow from going into the incubator. This also aids in a quicker increase in the compartment temperature. Then when the incubator has reached $T_{set,new}$, the porthole through which the IRT camera was recording can be opened again. This latter reasoning is captured within this experiment.

10.1.6. Airboost

Four curves can be seen in Fig. 9.10: T_{cam} , $T_{sensor1}$, $T_{sensor2}$, and T_a . Whenever the temperature is increased, a large spike in T_{atm} can be seen. Both sensors and the camera follow a similar pattern, albeit slightly attenuated. It can be seen that through the entire experiment the sensor in front of the open porthole measures a lower temperature than the other sensor, i.e. $T_{sensor2} > T_{sensor1} \forall t$. This can be explained by that fact that sensor 1 was in front of an open porthole at all times, whereas sensor 2 was not. Both the sensors and the camera follow a similar pattern. This is perhaps best explained by “walking” through the graph and following all curves.

The graph starts by opening porthole 5, which is indicated by a drop in T_{atm} . Both the sensors and the camera plateau during these 15 minutes. This can be explained by the fact that when a porthole opens, cold air flows in. However, the walls of the canopy are still heated and keep giving off heat, which is why the temperatures don't immediately drop. In the heater graph it can be seen that once T_{atm} drops to 28°C, the heater turns on to 100%. After a few minutes its power drops to 40-50%.

Next, side 1 is opened. T_{atm} experiences a slight drop during 5-6 minutes, but then plateaus at 28°C. Sensor 1 and the camera increase immediately after side 1 has been opened, with sensor 2 following with a slight delay. The reason that the sensors and the camera keep increasing the measured temperature is because side 1 is on the backside of the sensors on the box. This means heat is still given off by the side that is still closed. Similarly this is why T_{atm} is able to reach 28°C degrees once more. The heater graph shows full power as long as T_{atm} does not increase. When it has almost reached 28°C, its power gradually drops to 30%. To keep the temperature at 28°C, it spikes to 100% multiple times.

Then side 2 is opened too. T_{atm} steadily remains at 28°C. The heater manages this by varying between 20 and 40% with an occasional spike to 100%. T_{cam} and $T_{sensor1,2}$ immediately drop once this side is opened. No more heat is received by the walls, and thus all the objects are now fully exposed to room temperature.

Now that all sides have been opened, and measurements made with the airboost setting, all sides were then closed again, so that T_{set} could be increased to 29°C. Porthole 5 was left open so that the IRT could keep recording. T_{atm} starts a steep incline past 29°C. The heater power is at 100% for a few seconds, and only provides little power by spiking to 65%, 40%, 30%, 20% and 5% for a matter of seconds once $T_{atm} = 29^\circ\text{C}$ has been reached. $T_{sensor1,2}$ and T_{cam} immediately start climbing, but plateau at a value lower than 28°C.

Side 1 is opened again. T_{atm} takes a large fall down to $T_{atm} = 28^\circ\text{C}$, but manages to climb up to $T_{atm} = 29^\circ\text{C}$ in approximately 10 minutes. The heater power is at 100% until $T_{atm} = 29^\circ\text{C}$. The heater gradually provides less power as the environment stabilises. $T_{sensor1,2}$, T_{cam} , and the heater power follow a similar pattern as previously described when side 1 opened.

All consecutive events (opening sides and increasing temperature whilst closing sides) follow the same structure as described above.

Discussion

Comparing energy percentage of the heater to T_{atm} indicates that each time T_{set} was increased by 1°C, the heater turns off halfway when it has reached 7.5 minutes, i.e. half of the period in which the temperature is allowed to increase. As described in the experiment, the sides were closed, except for the porthole through which was measured, during a temperature increase. This would indicate the canopy walls contained enough

stored heat for the system to turn off its own heater. Comparing this to when a side is open, the heater is continuously providing power, albeit not to its full capacity.

Two additional measurements should have been performed to compare the effects of the airboost setting against. These two measurements would have been to 1) recreate the “Opening Portholes” measurement with the airboost setting turned on, and 2) recreate this same measurement but without the airboost setting on. By comparing all these measurements an objective statement could have been made about the consequences of this setting.

10.1.7. Testo 890

To see whether T_{cam} is independent of camera type/brand, a different type of IRT camera was used to perform the same measurement as in Sec. 9.2.5. A similar graph was made using the Testo 890 and can be seen in Fig. 9.12. All parameters were set to be equal to those used in the measurements with the A305sc. This graph should have similar characteristics as Fig. 9.8 for $45 \leq t < 105$. For an elaboration of this graph, see Sec. 10.1.5. By comparing both Fig. 9.12 and its corresponding interval in Fig. 9.8, it is clear these two do not show the similarities that were expected. Where the A305sc yields temperatures larger than the temperature sensor it measured next to, the Testo 890 consistently measures lower temperatures than both sensors.

Discussion

As was stated in this thesis, every IRT camera manufacturer uses its own model to determine the temperature. This thesis determined the model used in the A305sc. A brief search for such a model used by Testo yielded no results. This result means that a calibration measurement should be performed when a different type/brand of camera is used in combination with the prediction algorithm.

The Testo 890 has similar specifications as the A305sc, i.e.

- Thermal sensitivity: $< 0.040^{\circ}\text{C} + 30^{\circ}\text{C}$.
- Accuracy: $\pm 2^{\circ}\text{C}$ or $\pm 2\%$ of reading.
- Refresh Rate: 33Hz.

It should be noted that no parameters could be set for an external optic. However, the measurement that was performed, was done without foil and should thus have no effect on the measurement. Additionally, the software did neither allow for creation of multiple measurement rectangles, nor did it allow for customisation. For this measurement a measurement point was made and placed in the middle of the electrical tape. The camera also did not support creating videos from which data could be extracted. It was therefore chosen to physically tape the "Take photo button" on top of the camera in such a way that photos would be taken continuously. This meant no control was possible over the frame rate. A total of 925 images were taken over 60 minutes, which yields a refresh rate of 0.25Hz, or an FPS of 0.25.

10.2. Neonatal Measurements

Unfortunately, the IRT recordings itself are no longer available to the researcher. In the case that these would have been available, the next step would have been to implement the pre-processing block diagram of Fig. 7.1.

In Fig. 9.14, three very different results can be seen. In Fig. 9.14a it can be seen that when the temperature sensor is fully covered by the adhesive, the measured temperature is higher at every point in time. However, after 20 minutes, when both sensors have acquired their steady-state temperature, they only differ 0.2°C . This can be considered noise, as the temperature sensors have an accuracy of $\pm 0.1^{\circ}\text{C}$. In Fig. 9.14b, the situation is completely reversed, however there is still only a 0.2°C difference as they reach steady-state. In Fig. 9.14c, an adhesive has become loose which led to poor measurements.

Fig. 9.14h depicts the situation when the neonate is laying on its side, so that the sensor is either on the neonates free side, or between the neonate and the mattress. Up to $t = 20$ the difference is larger than twice the standard deviation, i.e. $2 \cdot \pm 0.1^{\circ}\text{C}$, which could indicate a difference in measured temperature due to the measurement setup. However, more measurements would have to be performed to make a statement whether this was a coincidence or not.

10.3. Conclusion

An in-depth interpretation of the results acquired in Chapter 9 has been given. Overall, the IRT camera measures a higher temperature than the thermistor sensors, but follows the thermistor sensors' pattern.

11

Conclusions and Recommendations for Future Work

This chapter will provide a conclusion to the initial research question and its sub-questions that were defined in Sec. 1.1. The scientific contributions will be discussed, and finally this chapter will end with recommendation for future work.

11.1. Conclusions

The initial goal of this thesis was to develop an algorithm able to predict disease in (pre)term neonates, which was formulated as follows:

“Can we predict disease in (pre)term neonates by using pattern recognition on early onset heat patterns using infrared thermography?”

However, it was decided that this thesis would focus on a smaller part of this research question. This thesis has provided a building block to aid in answering this question. It has done so by quantifying the interaction between IRT and a neonatal incubator. This corresponds to the following research question.

“Can we quantify the interaction between IRT and a neonatal incubator (with and without a neonate in it)?”

From this research question, several sub-questions arose that are required to form a substantiated answer. Answering these required setting up requirements for an IRT camera suitable to be used in a hospital setting, deciding upon an IRT camera, developing an open-source application to communicate with the camera, determining a measurement setup, developing an application to read out incubator sensor values, gaining permission to perform IRT measurements with neonates in an incubator, and finally quantifying the interaction between IRT and an incubator under different circumstances. Over the course of this thesis, all goals have been covered.

A list of requirements for the IRT camera has been set up. This included researching technical parameters, e.g. FPS, resolution, and sensitivity. An FPS larger than 5 was found not to be necessary due to the speed of visible physiological changes for IRT. Additionally, when FPS is increased, data storage quickly becomes an issue. In order to witness a change as small as 1cm^2 at a distance of 120cm, a FOV of 27° would be required, with a minimum of 167x167 pixels. A sensitivity of 0.1°C was considered adequate. Cost was to be kept at a minimum so that it would be available for less wealthy hospitals and was determined to be $<1000\text{€}$. An open-source application should be written for the camera, which limited the choice to the FLIR One Pro. However, due to limited budget, the FLIR A305sc was used in this thesis.

For the camera that was used in this thesis, a list of open-source GenICam tools was created. From this list an option was chosen that adhered to all additional requirements set to this open-source communication, i.e. it should be free, and is compatible with Linux. This has led to the choice of using Aravis Open Source

Project to communicate with the FLIR A305sc.

Due to the opaque property of the incubator hood material for IR, a measurement setup was created that circumvented this problem. Three different setups were discussed, and one was chosen. With the possibility of a neonate falling out, only one option was deemed feasible. This option entailed to seal an opened porthole with HDPE or LDPE and place the camera on a tripod in front of this sealed porthole.

To quantify the behaviour of IRT in combination with an incubator, the current golden standard was used to compare against the IRT measurements. This required reading out the incubator sensor values. For this, an application in C/C++ was written that could automatically detect between two types of incubator, and read out and subsequently log all its available sensor data, and store it in a standard format that would allow for easy integration to upload it to a database.

Whilst working on the previous goals, a measurement protocol was devised that was accepted by the HREC of two hospitals: the JKZ in The Hague, and the RDGG in Delft. Due to its non-invasive nature, i.e. a neonate is not required to perform any action, take any drugs, this research could be marked as n-WMO. It also had to be evaluated by the TU Delft's HREC. Eventually permission was granted and a combined total of 25 neonates were included in this study.

Measurements were performed with and without neonates and compared against the current golden standard, i.e. thermistors. To adhere to the n-WMO status of this thesis, different circumstances were modelled using inanimate objects inside the incubator, rather than performing these on an actual neonate. Measurements were performed to determine the accuracy of IRT and thermistors, the effects of distance on the IRT temperature, portholes were opened during the measurement, during a setting on the incubator which was designed to prevent warm air from flowing out, and this specific type of IRT camera was compared to a Testo 890.

11.1.1. Limitations

In this thesis an IRT camera was chosen that should have been used in this thesis. However, to save expenses, a camera that was already available at the TU Delft was used.

11.2. Thesis' Contributions to Science

This thesis has yielded several contributions to the scientific and engineering community that are as follows:

11.2.1. Open-Source IRT Camera Recording Application

By combining an open-source project available for Linux and reverse engineered camera settings/models, an application was written that is independent of the software developed by the camera manufacturer. This application yields more transparency into the inner functioning of an IRT camera, whilst simultaneously providing an open-source way to perform measurements.

11.2.2. Incubator Detection and Logging Application

An application was written that can automatically detect a certain type of incubator and log its sensor values. Each brand of incubator uses its own method to transmit its sensor values. Dräger requires active handshaking with its device and communicates via a protocol called "Medibus". GE transmits its data regardless of whether communication is established. These two types of communication have been brought together and manipulated into a data format that it is easy to upload to a database. Logging takes place by uploading each received string into the database. Additionally, this application was written in such a manner that a base class *incubator* was developed, such that each different type of incubator subclass could inherit from this class.

11.2.3. Quantification of the Interaction Between IRT and Incubator

This thesis has quantified IRT interactions with an incubator under different circumstances that simulate real-life scenarios. These include changing the distance between camera and incubator, opening 1 or more portholes, a setting that prevents warm air from flowing out, whilst using different types of sealing foil. Additionally a different brand of IRT camera was used and one such measurement was performed to study the differences.

Reflected Apparent Temperature

The RAT has not been determined in such a manner before, let alone for two different types of incubator. An incorrect value of the RAT can yield large errors in IRT measurements, and is therefore crucial to determine. In this thesis, the RAT was determined for the temperature range of 28° to 33°C, for each possible porthole through which can be recorded.

11.2.4. Data Collection

A foot in the door has been made for follow-up research in this area. Both the JKZ in The Hague and the RDGG in Delft are now familiar with this kind of research, and have seen that it does not hinder or restrain nurses/physicians in their daily work. With their help, a database with recordings of 25 neonates has been accumulated with a total of 25 hours of video material.

11.3. Recommendations for Future Work

As progress was made, alteration or recommendations for future work became evident during result analysis. This section will describe recommendations and improvements for future work expanding on this work, based on the achieved measurements and results.

11.3.1. Combining IRT Camera Recording Application with Incubator Detection Application

Two separate applications were created that both served an independent purpose. Currently these would have to be run separately, which could create some misalignment in the data. Combining these two applications into one will eliminate this misalignment. Additionally, a GUI can be created that translates the current separate source codes into an application that allows a user to easily connect to a camera and read out its recordings, whilst simultaneously displaying a graph of the temperature measured by the incubator temperature sensors.

Within this GUI, different sections can be created. One major section can display, in real-time, the cameras recordings based on the reverse engineered model described in this thesis. This model requires many internal parameters to be set correctly. A section that allows for easy manipulation of these parameters will increase user ease of access.

Another recommended GUI section is a graph of the incubator sensors data, possibly with an option which sensor graph to display. The section can also contain an alarm that goes off when a certain sensor crosses a set threshold value. Finally, the written software that automatically detects the connected incubator could support more types of commonly used neonatal incubators. Their data then must be translated into the current string format for easy uploading to the database.

Finally, another GUI section can be created to display previously stored recordings/graphs by downloading them from the database by providing a time period and/or patient.

11.3.2. Quantifying Interaction Between IRT and Incubator

While experiments have been performed that simulate real-life scenarios, the following recommended scenarios also include an outside actor to interfere with the internal environment. For instance, an experiment can be performed that opens portholes and has a warm object enter through one or more portholes. This warm object will then interact with the (already warmed) object under consideration.

All of the measurements should be performed using a sealing foil as this is basically the only suitable safe option. An additional improvement on this can be to perform these measurements again, but now with a 3D printed piece of properly fitting/sealing PE, rather than a piece of cut of foil. That way the porthole will be closed properly and there will be less danger of the neonate rolling out.

RAT

The RAT measurement was performed at three fixed locations. These locations can be adjusted such that they correspond with the locations of relevant body parts of a neonate. This means placing the boxes more forward, backward, left, or right. Additionally, this measurement can be performed multiple times so that an average and a value that approaches the mean can be derived.

11.3.3. Data Collection

In order to record an unhealthy child, the researcher had to bring his gear and set it up prior to performing a measurement. On top of that, the researcher was only available during the day. The ideal situation would be that the measurement setup is always ready to record as soon as a child becomes sick and the presence of the researcher to start recording would not have been necessary. Perhaps the nurses can execute this data collection.

11.3.4. Future Work

A database has been developed of 25 IRT recordings of mostly healthy neonates. This research can be expanded by researching/developing heat patterns that correspond with a certain infection/disease. However, as was an issue with this thesis, once a neonate becomes ill, it is past the initial symptoms when it is diagnosed. Yet these initial symptoms are important. Additionally, it is, unfortunately, not always clear what illness had befallen a neonate before they get better. This makes it impossible to classify measured heat patterns, which complicates developing heat patterns.

In the event that these heat patterns can be successfully developed, the actual prediction algorithm has to be developed. Chapter 4 describes methods to perform noise reduction and deep learning on these heat patterns with classified and unclassified data.

This thesis was granted permission to record neonates due to its n-WMO nature. A future study can perhaps be set up in such a manner that neonates are filmed in a standard position. This way, a database of the same recorded location, under fixed conditions, of different neonates can be established. By minimising the amount of variables, a more objective database can be established.

A

Neutral Thermal Environmental Temperatures

The temperature range that a neonate should be warmed at differs greatly depending on weight, age of gestation, and age of life. A table with neutral thermal environmental temperatures per age and weight is shown in this appendix.

Table 15.1 Neutral Thermal Environmental Temperatures		
Age and weight	Temperature*	
	At start (°C)	Range (°C)
0–6 h		
Under 1,200 g	35.0	34.0–35.4
1,200–1,500 g	34.1	33.9–34.4
1,501–2,500 g	33.4	32.8–33.8
Over 2,500 g (and >36 weeks' gestation)	32.9	32.0–33.8
6–12 h		
Under 1,200 g	35.0	34.0–35.4
1,200–1,500 g	34.0	33.5–34.4
1,501–2,500 g	33.1	32.2–33.8
Over 2,500 g (and >36 weeks' gestation)	32.8	31.4–33.8
12–24 h		
Under 1,200 g	34.0	34.0–35.4
1,200–1,500 g	33.8	33.3–34.3
1,501–2,500 g	32.8	31.8–33.8
Over 2,500 g (and >36 weeks' gestation)	32.4	31.0–33.7
24–36 h		
Under 1,200 g	34.0	34.0–35.0
1,200–1,500 g	33.6	33.1–34.2
1,501–2,500 g	32.6	31.6–33.6
Over 2,500 g (and >36 weeks' gestation)	32.1	30.7–33.5
(continued)		

Table 15.1 (Continued)

Age and weight	Temperature*	
	At start (°C)	Range (°C)
36–48 h		
Under 1,200 g	34.0	34.0–35.0
1,200–1,500 g	33.5	33.0–34.1
1,501–2,500 g	32.5	31.4–33.5
Over 2,500 g (and >36 weeks' gestation)	31.9	30.5–33.3
48–72 h		
Under 1,200 g	34.0	34.0–35.0
1,200–1,500 g	33.5	33.0–34.0
1,501–2,500 g	32.3	31.2–33.4
Over 2,500 g (and >36 weeks' gestation)	31.7	30.1–33.2
72–96 h		
Under 1,200 g	34.0	34.0–35.0
1,200–1,500 g	33.5	33.0–34.0
1,501–2,500 g	32.2	31.1–33.2
Over 2,500 g (and >36 weeks' gestation)	31.3	29.8–32.8
4–12 d		
Under 1,500 g	33.5	33.0–34.0
1,501–2,500 g	32.1	31.0–33.2
Over 2,500 g (and >36 weeks' gestation)	—	—
4–5 d	31.0	29.5–32.6
<i>(continued)</i>		

Table 15.1 Neutral Thermal Environmental Temperatures (*Continued*)

Age and weight	Temperature*	
	At start (°C)	Range (°C)
5–6 d	30.9	29.4–32.3
6–8 d	30.6	29.0–32.2
8–10 d	30.3	29.0–31.8
10–12 d	30.1	29.0–31.4
12–14 d		
Under 1,500 g	33.5	32.6–34.0
1,501–2,500 g	32.1	31.0–33.2
Over 2,500 g (and >36 weeks' gestation)	29.8	29.0–30.8
2–3 wk		
Under 1,500 g	33.1	32.2–34.0
1,501–2,500 g	31.7	30.5–33.0
3–4 wk		
Under 1,500 g	32.6	31.6–33.6
1,501–2,500 g	31.4	30.0–32.7
4–5 wk		
Under 1,500 g	32.0	31.2–33.0
1,501–2,500 g	30.9	29.5–35.2
5–6 wk		
Under 1,500 g	31.4	30.6–32.3
1,501–2,500 g	30.4	29.0–31.8

*Generally speaking, the smaller infants in each weight group will require a temperature in the higher portion of the temperature range. Within each time range, the younger infants require the higher temperatures.

Source: Klaus MH, Fanaroff AA. The physical environment. In: *Care of the high risk neonate*. 5th ed. Philadelphia: WB Saunders; 2001.

B

Checklist HREC TU Delft

Delft University of Technology
ETHICS REVIEW CHECKLIST FOR HUMAN RESEARCH
 (Version 10.10.2017)

This checklist should be completed for every research study that involves human participants and should be submitted before potential participants are approached to take part in your research study.

In this checklist we will ask for additional information if need be. Please attach this as an Annex to the application.

Please upload the documents (go to [this page](#) for instructions).

Thank you and please check our [website](#) for guidelines, forms, best practices, meeting dates of the HREC, etc.

I. Basic Data

Project title:	ThermocamPro
Name(s) of researcher(s):	Bas Bosma
Research period (planning)	10 weeks
E-mail contact person	K.Rassels@tudelft.nl or B.Bosma@Student.tudelft.nl
Faculty/Dept.	3mE
Position researcher(s):¹	Master graduation student
Name of supervisor (if applicable):	Kianoush Rassels, Paddy French, Pieter Jonker
Role of supervisor (if applicable):	Supervising

II. A) Summary Research

Neonates have an immature immune system, which makes them vulnerable to infections. In addition, both term and premature neonates are unable to communicate when they are ill or feel pain. An infection only becomes apparent by clinical signs and symptoms or by laboratory examinations. Infections can be cured with antibiotics, but in neonates it is difficult to determine which children need them. Current guidelines lead to overtreatment of neonates with antibiotics. Therefore, new methods are necessary to help clinicians to distinguish neonates with infections from children without infections.

This pilot study will focus on developing a non-invasive thermography technique to predict infection in (preterm) neonates. This technology could also be used to determine which children need antibiotic treatment and monitor the response to antibiotic treatment. The social and scientific relevance of this study are such that it could help to detect infections (and even prevent infection/disease) in neonates in the early stages of disease, so prompt treatment can be started, thereby preventing morbidity and mortality. On the other hand, it has the potential to prevent unnecessary antibiotic use in children without increased infection risk.

B) Risk assessment

Infrared thermography cameras use thermal imaging technology (remote sensing), which means it does not emit any radiation and is thus not harmful to the child in any way. Provided care by the doctors and nurses for the neonate will not be intervened with this research method and they can perform their task as usual. The measurement setup will be an infrared camera placed from 0.5m to 2m on a tripod from the neonate, connected via an Ethernet cable to a laptop. It does record a subject and stores the video and/or images for offline image processing. The recorded material will be treated confidentially. Any information that will be recorded will be stored in such a way that only the researchers will have access to it and will have a number instead of his/her name. The recorded material will be coloured in such a manner that the child is not identifiable or recognizable.

¹For example: student, PhD, post-doc

III. Checklist

Question	Yes	No
1. Does the study involve participants who are particularly vulnerable or unable to give informed consent? (e.g., children, people with learning difficulties, patients, people receiving counselling, people living in care or nursing homes, people recruited through self-help groups).	X	
2. Are the participants, outside the context of the research, in a dependent or subordinate position to the investigator (such as own children or own students)? ²		X
3. Will it be necessary for participants to take part in the study without their knowledge and consent at the time? (e.g., covert observation of people in non-public places).		X
4. Will the study involve actively deceiving the participants? (e.g., will participants be deliberately falsely informed, will information be withheld from them or will they be misled in such a way that they are likely to object or show unease when debriefed about the study).		X
5. Personal data <ul style="list-style-type: none"> • Will the study involve discussion or collection of personal data? (e.g., BSN number, location, sexual activity, drug use, mental health). Please check the following definition (here link to data stewards website). If yes': Did the data steward approve your data management plan? (Electronic Consent) 		X
6. Will drugs, placebos, or other substances (e.g., drinks, foods, food or drink constituents, dietary supplements) be administered to the study participants?		X
7. Will blood or tissue samples be obtained from participants?		X
8. Is pain or more than mild discomfort likely to result from the study?		X
9. Does the study risk causing psychological stress or anxiety or other harm or negative consequences beyond that normally encountered by the participants in their life outside research?		X
10. Will financial inducement (other than reasonable expenses and compensation for time) be offered to participants?		X
Important: if you answered 'yes' to any of the questions mentioned above, please submit a full application to HREC (see: website for forms or examples).		
11. Will the experiment collect and store videos, pictures, or other identifiable data of human subjects? ³	X	

²**Important note concerning questions 1 and 2.** Some intended studies involve research subjects who are particularly vulnerable or unable to give informed consent. Research involving participants who are in a dependent or unequal relationship with the researcher or research supervisor (e.g., the researcher's or research supervisor's students or staff) may also be regarded as a vulnerable group. If your study involves such participants, it is essential that you safeguard against possible adverse consequences of this situation (e.g., allowing a student's failure to complete their participation to your satisfaction to affect your evaluation of their coursework). This can be achieved by ensuring that participants remain anonymous to the individuals concerned (e.g., you do not seek names of students taking part in your study). If such safeguards are in place, or the research does not involve other potentially vulnerable groups or individuals unable to give informed consent, it is appropriate to check the NO box for questions 1 and 2. Please describe corresponding safeguards in the summary field.

³ Note: you have to ensure that collected data is safeguarded physically and will not be accessible to anyone outside the study. Furthermore, the data has to be de-identified if possible and has to be destroyed after a

Question	Yes	No
<p>If "yes", please fill in Annex 1 and make you sure you follow all requirements of the applicable data protection legislation.</p> <p>In addition, please provide proof by sending us a copy of the informed consent form.</p>		
<p>12. Will the experiment involve the use of devices that are not 'CE' certified?</p> <p><i>Only, if 'yes': continue with the following questions:</i></p>		X
<p>➤ Was the device built in-house?</p>		
<p>➤ Was it inspected by a safety expert at TU Delft? <i>(Please provide device report, see: HREC website)</i></p>		
<p>➤ If it was not built in house and not CE-certified, was it inspected by some other, qualified authority in safety and approved? <i>(Please provide records of the inspection).</i></p>		
<p>13. Has or will this research be submitted to a research ethics committee other than this one? <i>(if so, please provide details and a copy of the approval or submission).</i></p>	X	

IV. Enclosures (tick if applicable)

- Full proposal (if 'yes' to any of the questions 1 until 10)
- Informed consent form (if 'yes' to question 11)
- Device report (if 'yes' to question 12)
- Approval other HREC-committee (if 'yes' to question 13)
- Any other information which might be relevant for decision making by HREC
- Data management plan approved by a data steward (if yes to question 5B)

V. Signature(s)

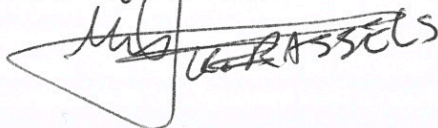
Signature(s) of researcher(s)

Date: 17-10-18

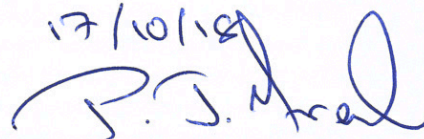


Signature (or upload Electronic Consent) research supervisor (if applicable)

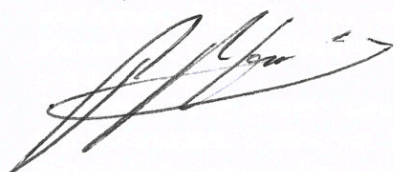
Date: 17-10-2018



17/10/18



17-10-2018



pub. de. in P. J. M. ... (3ME)

Appendix 1: Privacy and data protection

Please fill this in if you have answered 'yes' to question 11 in the checklist

- a. Will the participants have access to their own data? If no, please explain.
No, the data will be stored on a computer where image processing will be performed.

- b. Will covert methods be used? (*e.g. participants are filmed without them knowing*)
No.

- c. Will any human tissue and/or biological samples be collected? (*e.g. urine*)
No.

C

Ethics Application Full Proposal

Research Ethics Application

Please fill in the checklist first if you have not done so already. Please complete this form digitally and send it the Ethics Committee.

Date of Submission:2-11-2018

Project Title:ThermocamPro

Name(s) of researcher(s):Bas Bosma

Name of supervisor (if applicable):Kianoush Rassels, Paddy French, Pieter Jonker

Contact Information

Department:3mE

Telephone number:0648280924

E-mail address:B.Bosma@Student.tudelft.nl

Contact information of external partners (if applicable):K.Rassels@tudelft.nl

Summary

Please provide a brief summary of the research.

Neonates have an immature immune system, which makes them vulnerable to infections. In addition, both term and premature neonates are unable to communicate when they are ill or feel pain. An infection only becomes apparent by clinical signs and symptoms or by laboratory examinations. Infections can be cured with antibiotics, but in neonates it is difficult to determine which children need them. Current guidelines lead to overtreatment of neonates with antibiotics. Therefore, new methods are necessary to help clinicians to distinguish neonates with infections from children without infections.

This pilot study will focus on developing a non-invasive thermography technique to predict infection in (preterm) neonates. This technology could also be used to determine which children need antibiotic treatment and monitor the response to antibiotic treatment. The social and scientific relevance of this study are such that it could help to detect infections (and even prevent infection/disease) in neonates in the early stages of disease, so prompt treatment can be started, thereby preventing morbidity and mortality. On the other hand, it has the potential to prevent unnecessary antibiotic use in children without increased infection risk.

Research

R.1. What is the research question? Please indicate what scientific contributions you expect from the research.

Primary Objective:

- To develop thermography into a technique that can be used to predict infection before clinical symptoms are present.

Secondary Objectives:

- To explore whether thermography can be used in clinical practice, by exploring normal values of thermography of different body areas in preterm and term children.
- To explore whether thermography can distinguish neonates with a (suspected) infection from neonates without infection.
- To explore whether thermography can monitor the response to antibiotic treatment of infections.

The social and scientific relevance of this study are such that it could help to detect infections (and even prevent infection/disease) in neonates in the early stages of disease, so prompt treatment can be started, thereby preventing

morbidity and mortality. On the other hand, it has the potential to prevent unnecessary antibiotic use in children without increased infection risk.

R.2. What will the research conducted be a part of?

Bachelor's thesis

Master's thesis

PhD thesis

Research skills training

Other, namely: Enter what the research is part of here.

R.3. What type of research is involved?

Questionnaire

Observation

Experiment

Other, namely: Enter the type of research here.

R.4. Where will the research be conducted?

Online

At the university

Off-campus / non-university setting: Hospital

Other, namely: Enter where the research will be conducted here.

R.5. On what type of variable is the research based?

Give a general indication, such as questionnaire scores, performance on tasks, etc.

Infrared radiation which is translated into temperature

R.6. If the research is experimental, what is the nature of the experimental manipulation?

--

R.7. Why is the research socially important? What benefits may result from the study?

The social and scientific relevance of this study are such that it could help to detect infections (and even prevent infection/disease) in neonates in the early stages of disease, so prompt treatment can be started, thereby preventing morbidity and mortality. On the other hand, it has the potential to prevent unnecessary antibiotic use in children without increased infection risk.

R.8. Are any external partners involved in the experiment? If so, please name them and describe the way they are involved in the experiment.

Hospital. We want to observe neonates (in incubators) at the paediatric department.

Participants

Pa.1. What is the number of participants needed? Please specify a minimum and maximum.

Minimum: To be discussed with a paediatrician.

Maximum: To be discussed with a paediatrician.

Pa.2.a. Does the study involve participants who are particularly vulnerable or unable to give informed consent? (e.g., children, people with learning difficulties, patients, people receiving counselling, people living in care or nursing homes, people recruited through self-help groups)

Yes, the research population will consist of healthy neonates and neonates with suspected infection, who are born between 32 and 42 weeks of gestation.

Pa.2.b. If yes and unable to give informed consent, has permission been received from caretakers/parents?

Parents/caretakers will be asked to sign a written informed consent form.

Pa.3. Will the participants (or legal guardian) give written permission for the research with an 'Informed Consent' form that states the nature of the research, its duration, the risk, and any difficulties involved? If no, please explain.

Yes, the (preterm) neonate's parents or legal guardians will be asked to sign a written informed consent form.

Pa.4. Are the participants, outside the context of the research, in a dependent or subordinate position to the investigator (such as own children or students)? If yes, please explain.

No.

Pa.5. How much time in total (maximum) will a participant have to spend on the activities of the study?

They will only be recorded during normal activities and thus no action is required on their part.

Pa.6. Will the participants have to take part in multiple sessions? Please specify how many and how long each session will take.

Yes, as many as allowed by the nurse/doctors and advice of the physician.

Pa.7. What will the participants be asked to do?

Nothing, they will be recorded while they perform normal activities.

Pa.8. Will participants be instructed to act differently than normal or be subject to certain actions which are not normal? (e.g. subject to stress inducing methods)

No.

Pa.9. What are the possible (reasonably foreseeable) risks for the participants? Please list the possible harms if any.

Nothing.

Pa.10. Will extra precautions be taken to protect the participants? If yes, please explain.

No, as they will not be subjected to any harmful radiation or any other form of harm or physical contact.

Pa.11. Are there any positive consequences for a participant by taking part in the research? If yes, please explain.

The child that will be monitored will experience no positive consequences yet. However, the child will contribute to the prediction of potential infection or disease so that it can be prevented. This will increase the survival chances of future neonates. Being able to monitor when and how neonates respond to administered medicine will improve the understanding of required dosage of medicine for the child.

Pa.12. Will the participants (or their parents/primary caretakers) be fully informed about the nature of the study? If no, please explain why and state if they will receive all information after participating.

Yes.

Pa.13. Will it be made clear to the participants that they can withdraw their cooperation at anytime?

Yes.

Pa.14. Where can participants go with their questions about the research and how are they notified of this?

The researcher (Bas Bosma), his technical supervisor (Kianoush Rassels), or his medical supervisor at the hospital (Drs. Laura van der Meer-Kappelle).

Pa.15. Will the participants receive a reward?

Travel expenses

Compensation per hour

Nothing

Other, namely: Enter the reward here.

Pa.16. How will participants be recruited?

The neonates will already be in the paediatric department or neonatal intensive care unit, and in collaboration with the nurses/doctors/paediatricians, we will ask for written informed consent forms from their legal parents (guardians).

Privacy

Pr.1. Are the research data made anonymous? If no, please explain.

Yes, the recorded material will be treated confidentially. Any information that will be recorded will be stored in such a way that only the researchers will have access to it and will have a number instead of his/her name. The recorded material will be coloured in such a manner that the child is not identifiable or recognizable.

Pr.2. Will directly identifiable data (such as name, address, telephone number, and so on) be kept longer than 6 months? If yes, will the participants give written permission to store their information for longer than 6 months?

No, no identifiable data will be stored.

Pr.3. Who will have access to the data which will be collected?

The researcher (Bas Bosma), his technical supervisor (Kianoush Rassels), or his medical supervisor at the hospital (Drs. Laura van der Meer-Kappelle)

Pr.4. Will the participants have access to their own data? If no, please explain.

No, the data will be stored on a computer for image processing purposes

Pr.5. Will covert methods be used? (e.g. participants are filmed without them knowing)

No.

Pr.6. Will any human tissue and/or biological samples be collected? (e.g. urine)

No.

Documents

Please attach the following documents to the application:

- Text used for ads (to find participants);
- Text used for debriefings;
- Form of informed consent for participants;
- Form of consent for other agencies when the research is conducted at a location (such as a hospital or school).

D

Informed Consent Leaflet and Written Consent Form

Informatiebrief voor ouders

ThermocamPro

Het voorspellen van infectie in baby's en respons op behandeling

Inleiding:

Graag willen wij u vragen of u toestemming wilt geven om u kind mee te laten doen aan dit onderzoek. Het doel van het onderzoek is om middels een infraroodcamera een eventuele infectie bij pasgeboren baby's nog sneller dan tot nu toe te herkennen om zo vroeg mogelijk met de behandeling te kunnen starten. U beslist zelf of u en uw kind mee doet. Meedoen is vrijwillig en beïnvloedt op geen enkele wijze de behandeling van uw kind. Voordat u beslist of u wilt meedoen aan dit onderzoek, krijgt u uitleg over wat het onderzoek inhoudt. Lees deze informatie rustig door en vraag de onderzoeker uitleg als u vragen heeft. Om mee te kunnen doen hebben we van beide ouders schriftelijke toestemming nodig.

Algemene Informatie:

Dit onderzoek wordt gedaan op de afdeling neonatologie van het Reinier De Graaf Gasthuis te Delft.

Doel en achtergrond van het onderzoek:

Infecties bij pasgeboren baby's zijn over het algemeen goed te behandelen door middel van antibiotica. Het is belangrijk om infecties in een vroeg stadium op te sporen om op tijd met de behandeling te kunnen starten. Wanneer uw kind tekenen van een infectie vertoont zal bloed worden afgenomen om dit te controleren op waarden die op een infectie kunnen wijzen. Deze waarden in het bloed kunnen echter ook stijgen tijdens de bevalling zonder dat er sprake is van een infectie. Wanneer de temperatuur van uw kind stijgt zullen er maatregelen worden genomen om deze weer te laten dalen, bijvoorbeeld door de couveuse temperatuur aan te passen. Koorts is dus niet goed bruikbaar als teken van infectie bij pasgeboren baby's.

Het doel van het onderzoek is om een techniek te ontwikkelen die in staat is in een vroeg stadium een infectie te herkennen of voorspellen door een draadloze infraroodcamera.

Wanneer er bij uw kind een verdenking op een infectie is, zal gestart worden met antibiotica. Een van de onderzoeksvragen is of we na start van de antibiotica verschillen kunnen meten met de infraroodcamera die een vlot herstel van uw kind kunnen voorspellen.

Procedure:

Wanneer uw kind in een couveuse, wieg of warmebed ligt en u toestemming geeft voor het onderzoek zullen we middels een infrarood camera de warmte uitstraling van uw kind meten. In het geval van een couveuse zal de camera gericht worden op een kleine warmtestraling doorlatende opening die aan de bovenkant in de couveuse aanwezig is, omdat de camera niet door het basismateriaal van de couveuse kan filmen. Uw kind is niet herkenbaar in het beeld dat de camera vastlegt. Het filmmateriaal zal daarna anoniem worden geanalyseerd op een computer. Verder worden er medische gegevens uit het medisch dossier verzameld, zoals



gegevens over de geboorte, hartslag, ademhaling, temperatuur, symptomen en bloedsuitslagen. Deze gegevens worden gecodeerd opgeslagen en zijn dus niet herleidbaar tot uw kind.

Mogelijke voor- en nadelen van deelname aan dit onderzoek:

Dit onderzoek brengt geen risico's met zich mee. Uw kind zal geen andere behandeling krijgen en de reeds ingezette behandeling wordt niet beïnvloed door het onderzoek. Infrarood wordt door zowel voorwerpen als levende wezens uitgezonden. Deze infraroodstraling kan door de camera worden vastgelegd. De camera zendt zelf geen straling uit en is niet schadelijk voor uw kind.

Het onderzoek brengt geen voordeel mee voor uw kind. Wij hopen met dit onderzoek patronen middels de infraroodcamera te kunnen gaan herkennen die ons zullen helpen om infectie bij pasgeborenen in een vroeg stadium te herkennen zodat op tijd gestart kan worden met antibiotica zonder dat we te veel kinderen antibiotica geven die geen infectie blijken te hebben. In de toekomst, zullen wij mogelijk ook kunnen zien hoe snel de medicijnen helpen zodat de duur van de antibiotica beter afgestemd kan worden op het kind.

Vertrouwelijkheid en beschermde informatie:

Het beeldmateriaal zal verzameld worden door een master student van de TU Delft welke voor geheimhouding getekend heeft. Het beeldmateriaal welke door infraroodcamera wordt gereconstrueerd is dusdanig dat uw kind niet herkenbaar is.

De naam en andere persoonlijke gegevens van uw kind die hem/haardirect kunnen identificeren worden weggelaten en het beeldmateriaal wordt geanonimiseerd bewaard.

Alle gegevens van uw kind blijven vertrouwelijk. Alleen de onderzoeker en het onderzoeksteam weten welke code bij de geanonimiseerde gegevens horen. De sleutel voor de code blijft bij de onderzoeker. Ook in rapporten over het onderzoek worden nooit persoonlijke gegevens gebruikt.

Alleen de onderzoekers en een eventuele controleur van het onderzoek mogen uw medische gegevens inzien. Dit is om te controleren of het onderzoek goed en betrouwbaar uitgevoerd is. Mensen die uw gegevens kunnen inzien zijn vermeld in deze informatiebrief en maken deel uit van het onderzoeksteam. Zij houden uw gegevens geheim. Als u de toestemmingsverklaring ondertekent, geeft u toestemming voor het verzamelen, bewaren en inzien van de medische en persoonlijke gegevens van uw kind. De onderzoeker bewaart uw gegevens maximaal 15 jaar.

Deelname & Stoppen:

U beslist zelf of uw kind meedoet aan het onderzoek. Deelname is vrijwillig. Als u besluit niet mee te doen, hoeft u verder niets te doen. U hoeft niets te tekenen. U hoeft ook niet te zeggen waarom u niet wilt meedoen. Als uw kind wel meedoet, kunt u zich ten aller tijden bedenken



en het onderzoek laten stoppen. Eventueel verzamelde data zal met uw toestemming in het bezit van de onderzoeker blijven.

Vergoeding voor meedoen:

U wordt niet betaald voor het meedoen aan dit onderzoek.

Heeft u vragen?

Mocht u na het lezen van deze informatiebrief nog vragen hebben, dan kunt u deze altijd stellen aan de contactpersonen die hieronder genoemd worden.

Ondertekening toestemmingsformulier:

Wanneer u voldoende bedenktijd heeft gehad, wordt u gevraagd te beslissen over de deelname van uw kind aan dit onderzoek. Indien u toestemming geeft vragen wij u de bijbehorende toestemmingsverklaring te ondertekenen. Door uw schriftelijke toestemming geeft u aan dat u de informatie heeft begrepen en instemt met deelname aan het onderzoek.

Het handtekeningblad wordt door de onderzoeker bewaard. U krijgt een kopie of een tweede exemplaar van deze toestemmingsverklaring.

Dank voor uw aandacht.

Contact:

Supervisor / Reinier de Graaf Gasthuis:

Drs. Laura van der Meer-Kappelle

Kinderarts-neonatoloog

E: kinderartsen@rdgg.nl

T: 0152603688

TU Delft onderzoekers:

Supervisor / Biomedical Instrumentation TU-Delft

MSc. Kianoush Rassels, MSc.

E: K.Rassels@tudelft.nl

M: 06 11455666

Student Biomedical Engineering

Bas Bosma, BSc.

E: B.Bosma@Student.tudelft.nl

M: 06 48 28 09 24

ThermocamPro: Voorspellen van infectie in baby's en de respons op behandeling
Versie1 /11-10-2018

Ik ben gevraagd om toestemming te geven, zodat mijn kind meedoet aan dit medisch-wetenschappelijke onderzoek:

Naam proefpersoon:

Geboortedatum: __ / __ / __

Ik heb de informatiebrief voor de proefpersoon gelezen, of de inhoud is aan mij voorgelezen. Ik kon aanvullende vragen stellen. Deze vragen zijn naar tevredenheid beantwoord. Ik heb voldoende tijd gehad om te beslissen of mijn kind meedoet.

Ik weet dat dit onderzoek beeldmateriaal van mijn kind opslaat en analyseert. Dit beeldmateriaal is dusdanig opgeslagen dat mijn kind niet te identificeren is.

Ik weet dat meedoen helemaal vrijwillig is. Ik weet dat ik op ieder moment kan beslissen dat mijn kind toch niet meedoet. Daarvoor hoef ik geen reden te geven.

Ik weet dat sommige mensen de gegevens van mijn kind kunnen zien. Die mensen staan vermeld in de informatiebrief.

Ik geef toestemming om de gegevens te gebruiken voor de doelen die in de informatiebrief staan.

Ik vind het goed dat mijn kind meedoet aan dit onderzoek.

Naam ouder/voogd:

Handtekening:

Datum: __ / __ / __

Naam ouder/voogd:

Handtekening:

Datum: __ / __ / __

Ik verklaar hierbij dat ik bovengenoemde persoon/personen volledig heb geïnformeerd over het genoemde onderzoek.

Als er tijdens het onderzoek informatie bekend wordt die de toestemming van de ouder of voogd zou kunnen beïnvloeden, dan breng ik hem/haar daarvan tijdig op de hoogte.

Naam onderzoeker:

Handtekening:

Datum: __ / __ / __

E

WMO Checklist

Vragenlijst ter bepaling WMO plichtigheid

1. Wat is de titel van het onderzoek?

Predicting Infection and response to antibiotic treatment in Neonates Using Thermography Technology

2. Betreft het onderzoek waarbij proefpersonen aan handelingen worden onderworpen of hen gedragsregels worden opgelegd (inclusief het afnemen van vragenlijsten)?

Ja Nee

Indien ja, welke handelingen of gedragsregels gebeuren buiten het kader van de standaardbehandeling van de proefpersoon?

-

3. Betreft het een onderzoek waarbij een ongeregistreerd geneesmiddel wordt gebruikt?

Ja Nee

4. Betreft het een geregistreerd geneesmiddel dat voor een andere indicatie wordt gebruikt?

Ja Nee

5. Typeer de proefpersonenpopulatie (meerdere opties aankruisen mogelijk):

minderjarigen

wilsonbekwamen

wilsbekwamen \geq 18 jaar

patiënten

geen patiënten

6. Worden de proefpersonen gerandomiseerd?

Ja Nee

7. Is de privacy gewaarborgd?

Ja Nee

Zo ja, hoe?

Infrarood afbeeldingen zijn niet identificeerbaar of herleidbaar tot een patient. Bovendien zullen er geen gegevens van de patient, zoals naam, initialen, geboorteplaats/dag, etc. opgeslagen worden, maar zal een patient een studienummer krijgen waar mee gewerkt zal worden. De gegevens worden dus gecodeerd opgeslagen. De onderzoekopstelling zal niet aan de Electronische Patient Dossier (EPD) of het netwerk van het ziekenhuis aangesloten worden.

8. Gaat u vragenlijsten of interviews afnemen?

Ja Nee

Indien ja, gelieve vragenlijsten en/of interviewvragen bij te voegen.

Naam : G. Driessen

Functie : Kinderarts Haga Ziekenhuis, Juliana Kinderziekenhuis.

Datum : 24-10-2018

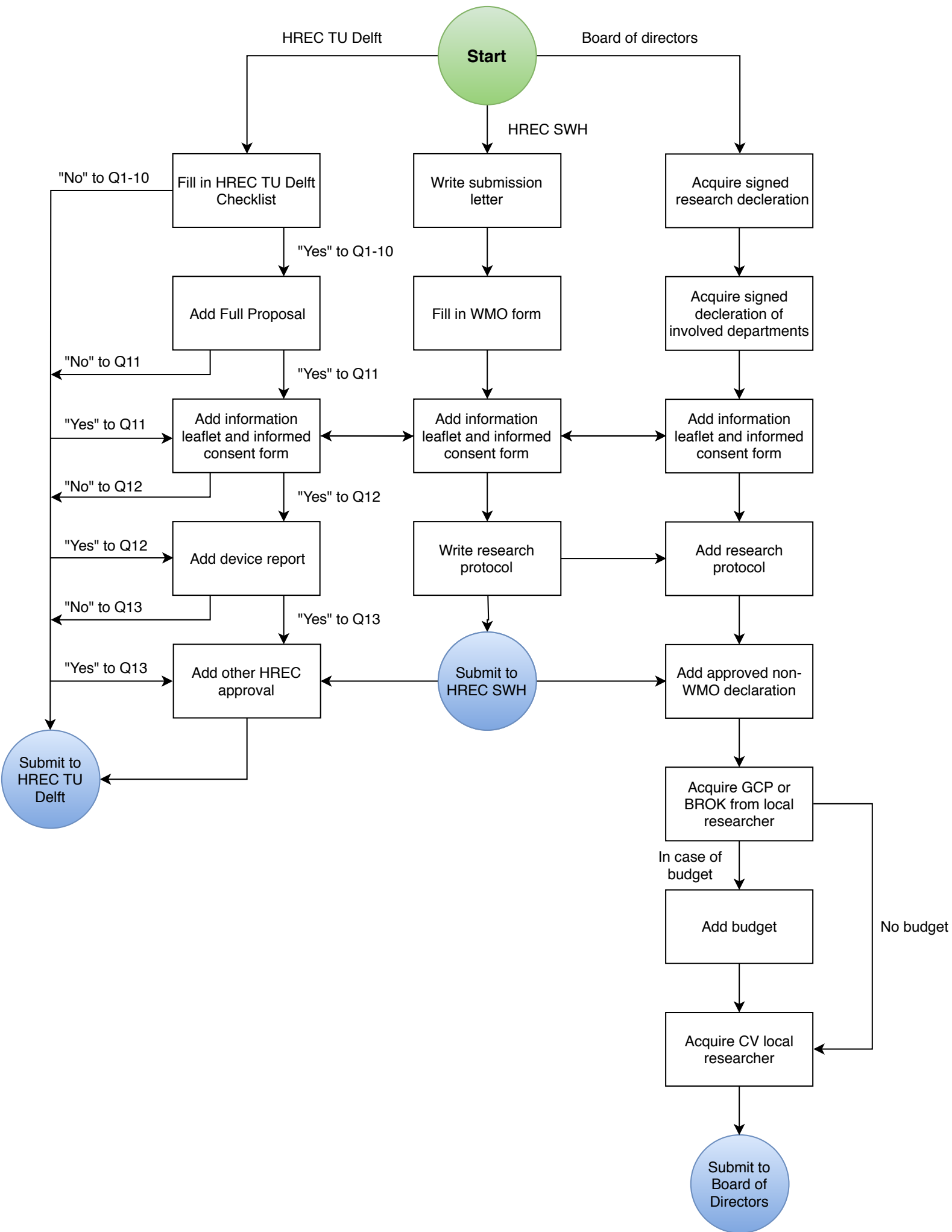
Bijvoegen:

- Protocol.
- Proefpersoneninformatie.
- Vragenlijsten (indien deze er zijn): geen.

F

Flowchart

A flowchart that one must follow so that submitting a proposal to a HREC can become easier can be found in this appendix.



G

GE Giraffe Omnibed Parameter Definition

Data Link Detail Description for Giraffe OmniBed & Giraffe Incubator

The data stream from the Giraffe products is repeated approximately every two seconds. The RS-232 parameters are:

- Baud rate: 19200
- Parity: None
- Data bits: 8
- Stop bits: 1
- Hardware flow control: None

The data is in ASCII format, comma delimited. White space within the string is used for formatting and should be discarded. The string is described below.

AAA_B.BB,CCCC,DDDD,EEEE,FFFF,GGGG,HHH,J,K,L,MM,NNN,P,Q,RRRRR,SSSS,TT,UU,VVV,WWW,XX,00

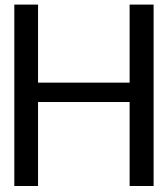
Parameter	Definition	Units	Range	Width
AAA	Product type: HYB is OmniBed, INC is Incubator. The Giraffe platform of products includes an OmniBed and an Incubator. The OmniBed is an incubator that can convert into a warmer with a button press from the customer.	N/A	HYB or INC	3
B.BB	Main application version number. There are more than one processor on the unit; however, the main application processor controls the RS-232 and the thermoregulation.	N/A	N/A	4
CCCC	Temperature from Patient Probe #1. The patient skin temperature will read the actual value; however, the display on the unit will only display between 30 and 42. If the probe is disconnected from the unit, the reading will be 'OPEN'.	°C	15.0 - 45.0 or open	4
DDDD	Temperature from Patient Probe #2. The patient skin temperature will read the actual value; however, the display on the unit will only display between 30 and 42. If the probe is disconnected from the unit, the reading will be 'OPEN'.	°C	15.0 - 45.0 or open	4
EEEE	Temperature from the Compartment Probe. This temperature is the environmental temperature inside the infant compartment. If the probe is disconnected from the unit, the reading will be 'OPEN'.	°C	15.0 - 45.0 or open	4
FFFF	Desired Environmental Temperature. This DET is the control temperature input to the air thermoregulation algorithm. The clinician sets it in the manual mode and the patient algorithm in the patient mode.	°C	20.0 - 39.0	4
GGGG	Patient Control (Set) Temperature. The clinician sets this control temperature; it is the control temperature input to the patient control algorithm.	°C	35.0 - 37.5	4
HHH	Heater Power. This is the percent heater power. In the closed bed state, this is the incubator heater, and in the open bed state, this is the warmer heater.	% Power	000 - 100	3
J	Thermoregulation Control Mode: Patient "P" or Manual "N". This mode determines the operating mode for thermoregulation. The patient mode is also referred to as baby mode or servo mode.	N/A	P or N	1
K	Open Bed State: Open "O" or Not Open "N". In an OmniBed, the open state is when the canopy is fully raised and the warmer heater doors are fully open. This will always be "N" in an incubator.	N/A	O or N	1
L	Closed Bed State: Closed "C" or Not Open "N". In an OmniBed, the closed state is when the canopy is fully lowered. This will always be "C" in an incubator.	N/A	C or N	1

Parameter	Definition	Units	Range	Width
MM	Humidifier Set Point. This is the control input for the humidifier. The clinician sets this parameter. If the humidifier is off (no set point selected), then this will read 00.	%RH	30 – 95 or 00	2
NNN	Relative Humidity. This is the relative humidity measured by the compartment probe inside the infant compartment.	%RH	000 – 100	3
P	Air boost Status. This is a flag describing the status of the Air boost button. A 'D' means that the Boost Air Curtain feature is off. An 'A' means that it is on. An 'L' means that the user forced the feature off by pressing the Air boost button and the Down button simultaneously.	N/A	D or A or L	1
Q	Fan Speed. This is the state of the fan speed. The fan has two speeds: high (H) and low (L).	N/A	H or L	1
RRRRR	Heat Sink Sensor Resistance. The incubator heater has a heat sink with a temperature sensor attached to it. The NTC thermistor has a resistance inversely proportional to its temperature. This reading is the resistance.	Ohms	00000 – 99999 but should be between 500 and 20000	5
SSSS	Last Weight. If the user weighed the patient since the unit was powered on, this reading will represent the last weight taken. If no weight has been taken, it will be zero.	Grams	0300 – 8000 or 0000	4
TT	Oxygen Set Point. This is the control input to the oxygen control system. This system is an option to the Giraffe products. The clinician can set the oxygen control level, and the hood will fill with that percent oxygen. If the option is absent or the clinician does not use it (no set point), this reading will be zero.	%O2	21 – 65 or 00	2
UU	Oxygen Reading. If the oxygen control system is installed, this reading will be the oxygen percent in the infant compartment. If it is not installed, it will be zero.	%O2	00 – 99	2
VVV	Saturation. If the pulse oximeter option is installed, this reading will be the saturation parameter. Otherwise, it will be zero. This option is currently not in use for the Giraffe OmniBed and Incubator.	%O2	000 – 105	3
WWW	Pulse Rate. If the pulse oximeter option is installed, this reading will be the pulse rate parameter. Otherwise, it will be zero. This option is currently not in use for the Giraffe OmniBed and Incubator.	bpm	000 – 250	3
XX	Alarms. If there are alarms active, they will be listed here, separated by commas. For example, if there are no alarms, this reading will not appear. If one alarm, then the XX will be that alarm code (see next table for alarm codes). If two alarms, then there will be XX, YY. There are a maximum of sixteen alarms.	N/A	00 - 99	2
00	There is a carriage return and line feed after this double zero. There is no checksum for the data string.	N/A	N/A	2

The alarm codes for the Giraffe OmniBed and Giraffe Incubator are described below.

Alarm	Code
System Failure	2
Enter Setting	3
Fan Failure	4
Fan Failure	5
Air Probe Failure	6
Air Probe Failure	7
Air Probe Disconnected	8
Air Probe Disconnected	9
Air Temperature > 40°C	10
Air Temperature > 38°C	11
High Air Temperature	12
Low Air Temperature	13
Baby Hot - Check Probe 1	14
Baby Cold - Check Probe 1	15
Baby Hot - Check Probe 1	16
Baby Cold - Check Probe 1	17
In Transition - Heat Off	18
Baby Probe 1 Failure	19
Baby Probe 1 Failure	20
Baby Probe 1 Failure	21
Disconnected Baby Probe 1	22
Disconnected Baby Probe 1	23
Check Baby	24
Check Baby - Heat Off	25
Fan Always in High Speed	26
Fan Always in High Speed	27
Heater Doors Not Opened	28
Heater Doors Not Closed	29
Line Comp out of Range	30
Bad Membrane Switch	31
In Transition - Heat Off	32
Elevation Time Out	33
Humidity High	34
Humidity Low	35
Humidity Probe Failure	36
Humidity Failure	37
Add Water	38
Water Reservoir Not Engaged	39
Low SpO ₂	40
High SpO ₂	41
Low Pulse Rate	42
High Pulse Rate	43
SpO ₂ Probe Disconnected	44
SpO ₂ Probe off Patient	45
SpO ₂ Probe Failure	46
High Oxygen	47
Low Oxygen	48

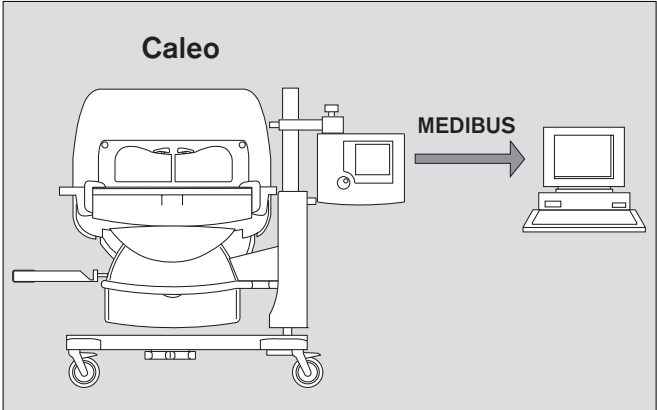
Alarm	Code
Calibrate Oxygen	49
Oxygen Probe Failure	50
Oxygen System Failure 1	51
Oxygen System Failure 2	52
Oxygen System Failure 3	53
Oxygen System Failure 4	54
O ₂ Cal Lost - No O ₂	55
Exceeds Maximum Weight	56
Scale Failure 7	57
Scale Failure 1	58
Scale Failure 2	59
Scale Failure 3	60
Scale Failure 4	61
Scale Failure 5	62
Scale Failure 6	63
Check Baby	64
Check Baby - Heat off	65
Baby Probe 1 Failure	66
Baby Probe 2 Failure	67
Canopy Pedal Failure	68
Bed Up Pedal Failure	69
Bed Down Pedal Failure	70
Too Many Modules	71
Fan Failure	72
Bed Heater Failure	73
Radiant Heater Failure	74
Motor Drive Failure	75
In Transition - Heat Off	76
Oxygen System Failure 5	78
Check O ₂ Supply	79
Oxygen System Failure 6	80
Oxygen System Failure 7	81
High Oxygen	82
Low Oxygen	83
Check SpO ₂ Sensor	84
Air Probe Failure	85
Canopy Pedal Disabled	86
Bed Height Pedals Disabled	87
Canopy Pedal Pressed	88
Bed Up Pedal Pressed	89
Bed Down Pedal Pressed	90
Baby Mode Disabled	91
Disconnect Probe 2 for Baby Mode	92
Temperature Out of Calibration	93
FiO ₂ > 26%	94
Warm Up Mode	95
Pre-heat Zone	96



Medibus Specification for Caleo

MEDIBUS Specification for Caleo

Device Connection



Port Specification

Connector	
Type	RS-232-C
Pins	9 pin Sub D (female)
Isolation	1.5 kV
Location	rear side of Caleo display housing
	Label: Baby Link®

To connect a PC to Caleo the "Medi-Cable" 83 06 488 is recommended.

Port Configuration

Baudrate	9600 Baud
Databits	8
Startbits	1
Stopbits	1
Parity	none

Device Identification

ID Number	Name	MEDIBUS-Version
8008	Caleo	04.00

Available Data

Current Measured Data, Alarm status, Device settings and text messages for Caleo are available from version 1.21.

Commands

Transmitted Commands

Code	Command Specification
30H	Do nothing (NOP)
51H	Initialize Communication (ICC)
52H	Request Device Identification

Processed and responded Commands

Code	Command Specification
24H	Request current DATA
27H	Request current ALARMS (Codepage 1)
2EH	Request current ALARMS (Codepage 2)
29H	Request current DEVICE SETTINGS
2AH	Request current TEXT MESSAGES
30H	Do nothing (NOP)
4AH	Configure Response
4BH	Set language
51H	Initialize Communication (ICC)
52H	Request Device Identification
55H	Stop Communication

Measured Data

Code	Data Description	Unit	Format
6CH	Air Humidity	%	_XX_
6DH	Air Temperature	°C	XX.X
C3H	Temperature 1	°C	XX.X
BEH	Temperature 2	°C	XX.X
F0H	Inspiratory O ₂ -Concentration	%	XXX_

Temperature 1 = Core temperature
 Temperature 2 = Peripheral temperature

Alarm Messages

Air Module (Codepage 1)

CODE	PRIO 18	Problems with Fan		
CAH	D: LUEFTER INOP	GB: FAN ERR	F: VENT INOP	
	I: ERR VENTOLA	NL: VENT INOP	E: VENT INOP	

CODE	PRIO 20	Air Temp. > high Limit		
30H	D: AMB TEMP "#	GB: AMB TEMP HI	F: AMB TEMP "#	
	I: AMB TEMP "#	NL: AMB TEMP "#	E: AMB TEMP "#	

CODE	PRIO 20	Air Temperature Sensor inop		
48H	D: AMB TEMPINOP	GB: AMB TEMP ERR	F: AMB TEMPINOP	
	I: AMB TEMPINOP	NL: AMB TEMPINOP	E: AMB TEMPINOP	

CODE	PRIO 8	Air Temp. Setting Deviation > X,X °C		
6BH	D: AMB TEMP DIF	GB: AMB TEMP DIF	F: AMB TEMP DIF	
	I: AMB TEMP DIF	NL: AMB TEMP DIF	E: AMB TEMP DIF	

Skin Module (Codepage 1)

CODE	PRIO 20	Skin Temp. 1 – Probe disconnected or fault		
46H	D: TEMP 1 INOP	GB: TEMP 1 ERR	F: TEMP 1 INOP	
	I: ERR TEMP 1	NL: TEMP 1 INOP	E: TEMP 1 INOP	

CODE	PRIO 20	Skin Temp. 2 – Probe disconnected or fault		
47H	D: TEMP 2 INOP	GB: TEMP 2 ERR	F: TEMP 2 INOP	
	I: ERR TEMP 2	NL: TEMP 2 INOP	E: TEMP 2 INOP	

CODE	PRIO 8	Skin Temp. 1 – Setting Deviation > X.X °C		
6DH	D: TEMP 1 DIF	GB: TEMP 1 DIF	F: TEMP 1 DIF	
	I: TEMP 1 DIF	NL: TEMP 1 DIF	E: TEMP 1 DIF	

CODE	PRIO 11	Skin Temp. 1 too high		
	D: TEMP 1 "#	GB: TEMP 1 HIGH	F: TEMP 1 "#	
CBH	I: TEMP 1 "#	NL: TEMP 1 "#	E: TEMP 1 "#	

CODE	PRIO 11	Skin Temp. 2 too high		
	D: TEMP 2 "#	GB: TEMP 2 HIGH	F: TEMP 2 "#	
CCH	I: TEMP 2 "#	NL: TEMP 2 "#	E: TEMP 2 "#	

O2 Module (Codepage 1)

CODE	PRIO 20	O2 Sensor inoperable		
	D: O2 SENS INOP	GB: O2 SENS ERR	F: CAPT O2 INOP	
43H	I: ERR SENS O2	NL: O2-SENS INOP	E: SENS O2 INOP	

CODE	PRIO 8	O2 Setting Deviation > 5 %		
	D: O2 DIF > 5 %	GB: O2 DIF > 5 %	F: O2 DIF > 5 %	
70H	I: O2 DIF > 5 %	NL: O2 DIF > 5 %	E: O2 DIF > 5 %	

O2 Module (Codepage 2)

CODE	PRIO 20	O2 Module inoperable		
	D: O2 MOD INOP	GB: O2 MOD INOP	F: MOD O2 INOP	
50H	I: O2 MOD INOP	NL: O2 MOD INOP	E: MOD O2 INOP	

Humidity Module (Codepage 1)

CODE	PRIO 15	Humidity Sensor inoperable		
	D: FEU SEN INOP	GB: HUM SENS ERR	F: HUM CAP INOP	
34H	I: ERR UMI SENS	NL: HUM SEN INOP	E: HUM SEN INOP	

CODE	PRIO 7	Water Reservoir empty		
	D: WASSERMANGEL	GB: WATER OUT	F: EAU FINI	
9EH	I: ACQUA FINI	NL: WATER STOP	E: AQUA FALTA	

Humidity Module (Codepage 2)

CODE	PRIO 15	Humidifier inoperable		
	D: FEUCHTE INOP	GB: HUM INOP	F: HUM INOP	
0CH	I: UMIDITA INOP	NL: BEVOCHT INOP	E: HUM INOP	

CODE	PRIO 7	Humidity setting deviation		
	D: FEUCHTE ABW	GB: HUMIDITY DEV	F: DEV HUM	
0DH	I: DEV UMIDITA	NL: VOCHT AFW	E: HUM DESV	

Device Settings

Code	Data Description	Unit	Format
1CH	Air Humidity	%	__XX_
1AH	Air Temperature	°C	_XX.X
1BH	Temperature Skin	°C	_XX.X
01H	Inspiratory O2-Concentration	%	_XXX_

Text Messages

DS mode is active

	D: Betriebsart DS	GB: Mode DS
CODE	F: Mode DS	NL: Mode DS
12H	I: Modo DS	E: Modo DS

Air module is active

	D: Modul LUFT aktiv	GB: Module AIR active
CODE	F: Module AIR actif	NL: Module LUCHT aktief
13H	I: Modo ARIA attivo	E: Modo AERE activado

Skin module is active

	D: Modul HAUT aktiv	GB: Module SKIN active
CODE	F: Mode PEAU actif	NL: Module HUID aktief
14H	I: Modo PELLE attivo	E: Modo PIEL activado

O2 module is active

	D: Modul O2 aktiv	GB: Module O2 active
CODE	F: Module O2 actif	NL: Module O2 aktief
15H	I: Modo O2 attivo	E: Modo O2 activado

Humidity module is active

	D: Modul FEUCHTE aktiv	GB: Module HUM. active
CODE	F: Mode HUMID actif	NL: Module HUMID aktief
16H	I: Modo HUMID attivo	E: Modo HUMID activado

Kangaroo mode is active

	D: KANGAROOMODE aktiv	GB: KANGAROO MODE active
CODE	F: Mode KANGAROO actif	NL: KANGOEROE MODUS actief
51H	I: Modo KANGAROO attivo	E: Modo CANGURO activo

Configuration mode is active

	D: KONFIGURATIONSMODE aktiv	GB: CONFIGURATION MODE active
CODE	F: Mode CONFIGURATION actif	NL: CONFIGURATIE MODUS actief
52H	I: Modo CONFIGURAZIONE attivo	E: Modo CONFIGURACION activo

Set language

This command is sent to set a certain language. This command effects the language for MEDIBUS only, the language used elsewhere, e.g. on display, will not be changed by this command. The command and the response have the following format:

Command:

ESC	4BH	Language Code	Checksum	CR	
0	1	2	4	6	Byte

Response:

SOH	4BH	Language Code	Checksum	CR	
0	1	2	4	6	Byte

ESC ASCII "escape" character (1BH)

SOH ASCII "start of header" character (01H)

Language Code "1" = 31H for German
"2" = 32H for English
"3" = 33H for French
"4" = 34H for Dutch
"5" = 35H for Spanish
"6" = 36H for Italian

Checksum Least significant 8-bit sum of all preceding bytes beginning with "ESC" or "SOH" in ASCII HEX format

CR ASCII "carriage return" character (0DH)

NOTE: Caleo responds with the code of the language it will set itself to. This may be either the language requested by command or the actual language if the received language code is illegal.



Opening Portholes - Filming Through Port 4

In Sec. 9.2.5 a measurement was performed to gain an understanding of the effects opening portholes can have on the temperature measured by the camera when filming without foil, through port 5. In this appendix, the graphs of the same measurement can be found, only now the temperature with the camera was measured through port 4.

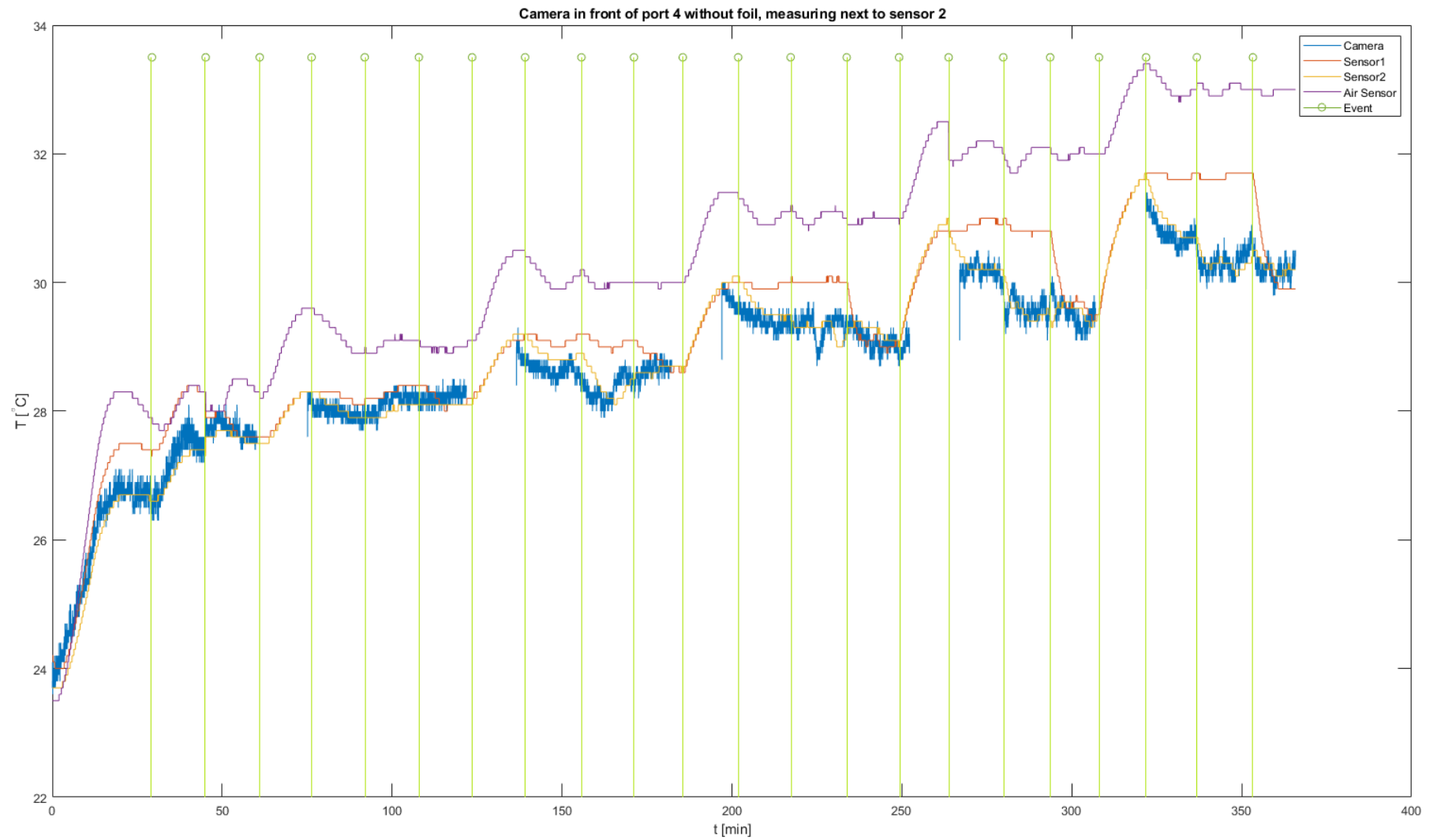


Figure I.1: Visualisation of the effect of opening additional portholes on the temperature as measured by multiple sensors. The blue line depicts the temperature as measured by the IRT camera, the red and yellow line depict the values measured by the temperature sensors that are stuck to the paperboard boxes through hospital adhesives. The purple line represents the air temperature sensor, and the green vertical lines indicate an event.

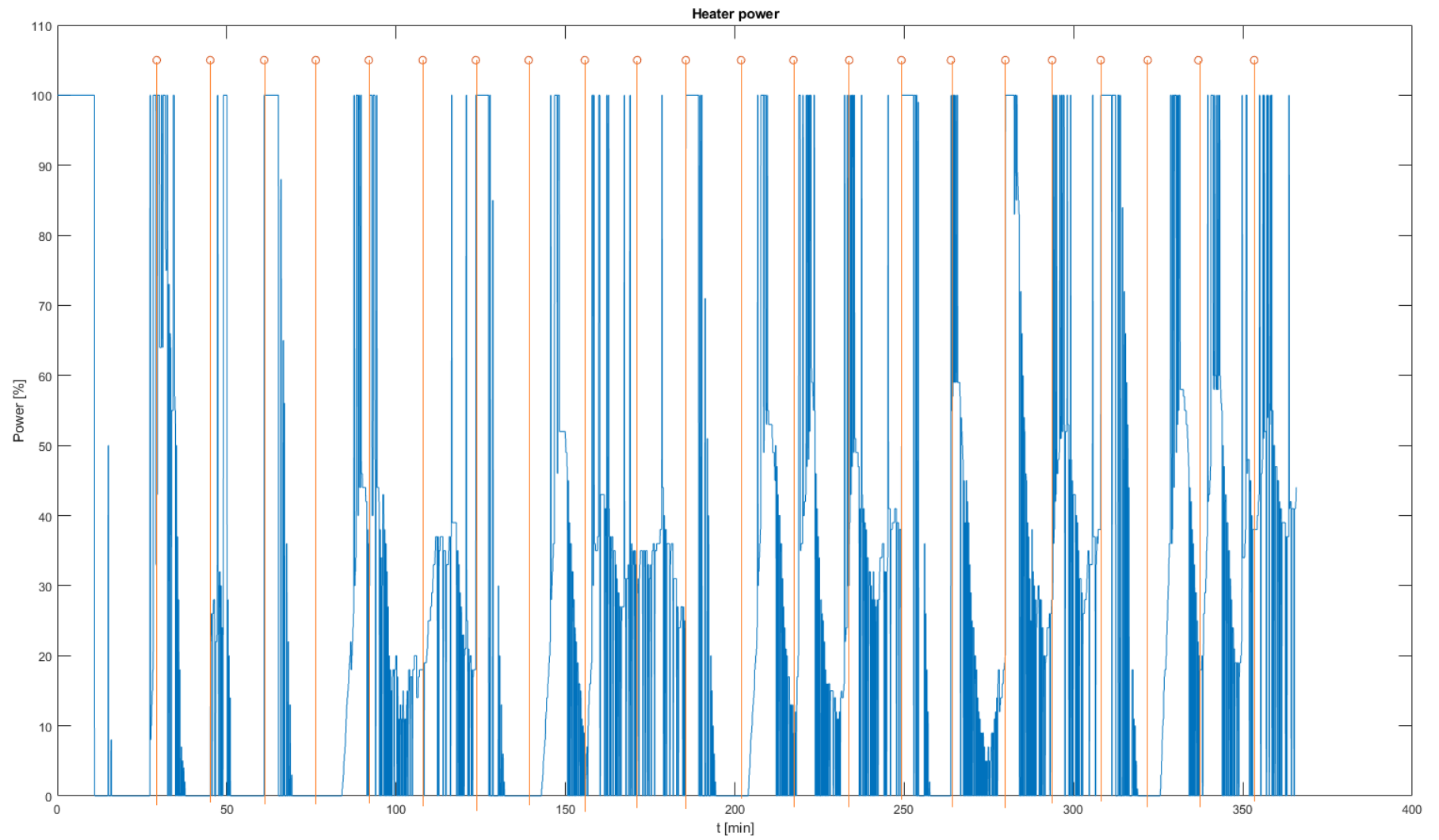


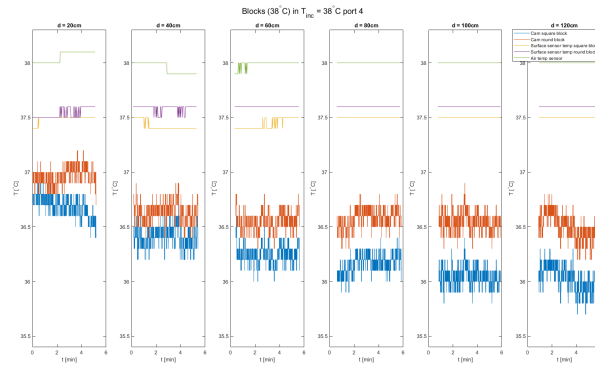
Figure I.2: Heater power percentage during the *Opening Portholes* measurement. Blue line depicts the power percentage of the heater during the measurement. The red lines indicate the same event.

J

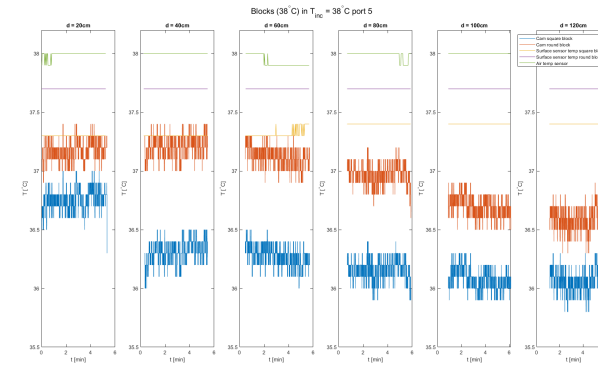
Changing Distance from Camera to Incubator

In Sec. 9.2.4 a measurement was performed to determine whether the losses in radiation due to the atmosphere were negligible or not. The camera was placed at an initial distance of $d = 20\text{cm}$, measured from the lens of the camera to the porthole through which was filmed, and set to record for 5 minutes at 9Hz. Simultaneously, the incubator sensor readout was logged. Afterwards the data was synchronized. These measurements were performed using the GE GiraffeTM Omnibed incubator, hence the sensor readout was done at 0.5Hz. The measurement was stopped after 5 minutes and the camera was moved 20cm backwards. This was repeated up to $d = 120\text{cm}$. All four different measurements were made once with HDPE covering the porthole, once with LDPE, and once without any foil covering the porthole through which was filmed. Sec. 9.2.4 shows the situation without foil, whereas this appendix shows the situation with HDPE (App. J.1) and with LDPE (App. J.2).

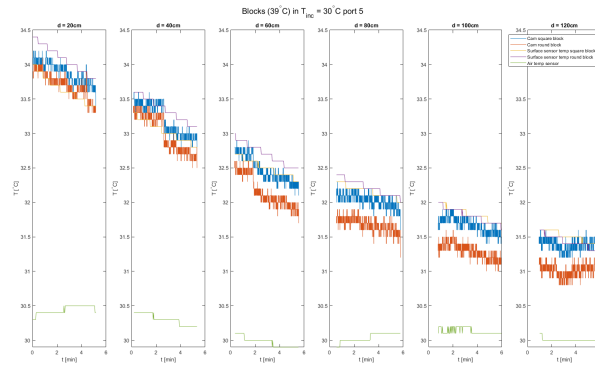
J.1. Porthole Covered with HDPE



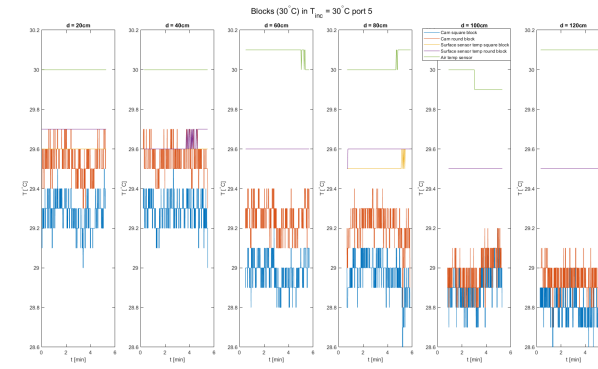
(a) Blocks (38°C) in $T_{inc} = 38^\circ\text{C}$ filmed through port 4 covered with HDPE.



(b) Blocks (38°C) in $T_{inc} = 38^\circ\text{C}$ filmed through port 5 covered with HDPE.



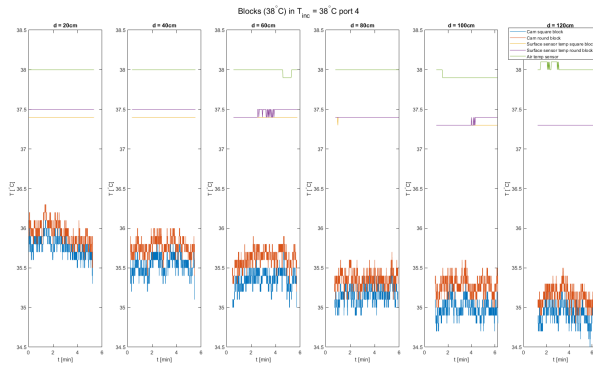
(c) Blocks (39°C) in $T_{inc} = 30^\circ\text{C}$ filmed through port 5 covered with HDPE.



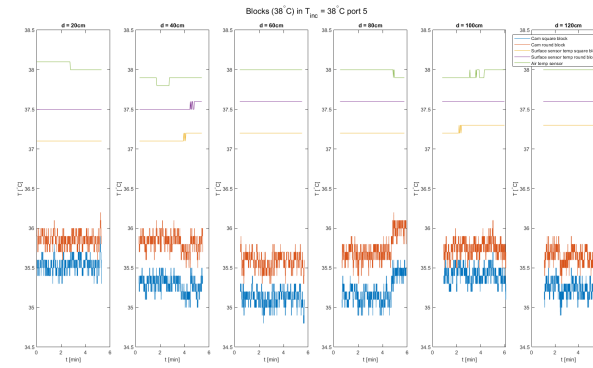
(d) Blocks (39°C) in $T_{inc} = 30^\circ\text{C}$ filmed through port 5 covered with HDPE.

Figure J.1: Each set of four graphs depict the effect of the distance between the camera and the incubator on the temperature when the porthole is covered with HDPE.

J.2. Porthole Covered with LDPE

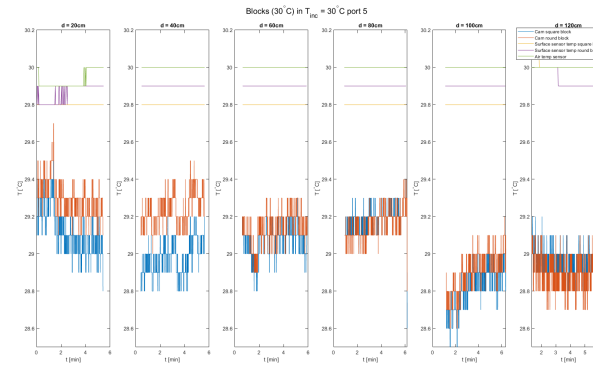


(a) Blocks (38°C) in $T_{inc} = 38^\circ\text{C}$ filmed through port 4 covered with LDPE.



(b) Blocks (38°C) in $T_{inc} = 38^\circ\text{C}$ filmed through port 5 covered with LDPE.

(c) Missing data.



(d) Blocks (30°C) in $T_{inc} = 30^\circ\text{C}$ filmed through port 5 covered with LDPE.

Figure J.2: Each set of four graphs depict the effect of the distance between the camera and the incubator on the temperature when the porthole is covered with HDPE.

K

Pt-100 Certificate of Calibration



Dutch
Metrology
Institute

CERTIFICATE OF CALIBRATION

Number T1271410
Page 1 of 26

Applicant TU Delft Faculteit EWI
Gebouw 36, Kamer HB 15.080
Cornelis Drebbelweg 12
2628 CM DELFT

Item Twelve platinum resistance thermometers

The identification of the sensor(s) is given with the results on following page(s).

Calibration procedure The thermometers were placed in a liquid tide tube and have been calibrated in a liquid bath by comparison with a standard thermometer, based on the ITS-90. The measurement current is a direct current of 1 mA and has a commutation frequency of 5 Hz.
At the start and end of the calibration the sensor(s) is measured at 0 °C.

The ambient temperature was (23.0 ± 1.0) °C.

Calibration period 10 May 2017 until 17 May 2017

Result The results of the calibrations are given on following page(s).
The reported uncertainty of measurement is based on the standard uncertainty of measurement multiplied by a coverage factor of $k = 2$, which for a normal distribution corresponds to a coverage probability of approximately 95 %. The standard uncertainty has been determined in accordance with the 'Guide to the Expression of Uncertainty in Measurement' (GUM).

Traceability The result of the calibration is traceable to primary and/or (inter)national accepted measurement standards.



Dutch
Metrology
Institute

Delft, 23 May 2017
VSL B.V.

R. van Breugel
Principal Metrologist

Identification of the sensor

Manufacturer : Thermo Electra
Type : Pt100
Identification number : VSL 17 T 013
The immersion depth : at least 25 cm.

Results

The result of the calibration and the related uncertainty is given here.

By means of regression a relation is determined between the generated temperature (t_{90}) and the measured resistance (R). The table below contains this relation and the calculated coefficients. The relation is valid over the calibrated range.

$$R(t_{90}) = R_0 \cdot \left\{ \sum_{i=0}^{i=n} a_i \cdot (t_{90})^i \right\}$$

with: $R_0 = 99.88069 \Omega$

and $\alpha = (R_{100} - R_0) / (100 \cdot R_0) \text{ } ^\circ\text{C}^{-1} = 3.85153 \times 10^{-3} \text{ } ^\circ\text{C}^{-1}$

The inverse relation between R and t_{90} is approximated by:

$$t_{90} = \sum_{i=0}^{i=n} b_i \cdot (R)^i$$

The coefficients for both relations are:

i	a_i	b_i
0	1	$-2.4796 \times 10^{+2}$
1	3.9084×10^{-3}	2.4139
2	-5.4826×10^{-7}	6.0752×10^{-4}
3	-2.0238×10^{-10}	5.5464×10^{-7}
4	0	2.4484×10^{-9}

The table below was made by means of the relation between t_{90} and R and contains the following data:

1. the temperature t_{90} , according to the ITS-90;
2. the resistance value $R_{n,90}$ at temperature t_{90} according to IEC 60751 (2008-07);
3. the resistance value R ;
4. the difference $R_{n,90}-R$;
5. the temperature-equivalent $\Delta t[R_{n,90}-R]$ in the difference $R_{n,90}-R$;
6. the temperature-equivalent of the uncertainty U in the resistance value;

$t_{90} / ^\circ\text{C}$	$R_{n,90} / \Omega$	R / Ω	$R_{n,90}-R / \Omega$	$\Delta t[R_{n,90}-R] / ^\circ\text{C}$	$U / ^\circ\text{C}$
-75.00	70.332	70.303	0.029	0.07	0.06
-55.00	78.319	78.248	0.071	0.18	0.06
-35.00	86.248	86.151	0.096	0.24	0.06
-15.00	94.124	94.013	0.112	0.28	0.06
5.00	101.953	101.831	0.122	0.31	0.06
25.00	109.735	109.605	0.129	0.33	0.06
45.00	117.470	117.335	0.136	0.35	0.06
65.00	125.160	125.018	0.142	0.37	0.06
85.00	132.803	132.654	0.149	0.39	0.06
105.00	140.400	140.243	0.158	0.42	0.06
125.00	147.951	147.782	0.169	0.45	0.06
145.00	155.456	155.272	0.184	0.49	0.06

The uncertainty includes a contribution from the reproducibility of the instrument, calculated using the deviations from the regression.

Bibliography

- [1] FLIR R&D software 1.2 User's Manual, FLIR, 2010. http://www.thermokameras.com/ir-systeme/software/Handbuch_ResearchIR.pdf [Retrieved 3-4-2019]
- [2] C. Öhman, Emittansmätningar med AGEMA E-Box, Teknisk rapport, AGEMA 1999. (C. Öhman, Emittance measurements using AGEMA E-Box. Technical report, AGEMA 1999.)
- [3] W. C. Wilson, C. M. Grande, D. B. Hoyt, *Trauma: Critical Care*, Boca Raton, FL, Taylor & Francis Group, 2007, pp. 193-198, ISBN: 978-1-4200-1684-0
- [4] M. A. Bramson, *Infrared Radiation - A Handbook for Applications*, Plenumpress, N.Y., 1968.
- [5] Transmetra, Table of Emissivity of Various Surfaces. https://www.transmetra.ch/images/transmetra_-pdf/publikationen_literatur/pyrometrie-thermografie/emissivity_table.pdf [Retrieved 10-4-2020]
- [6] P. Gardner, Understanding Infrared Camera Thermal Image Quality - Electrophysics Resource Center: Infrared Inspection, Electrophysics Corp., 2011.
- [7] H. V. Kennedy, "Modeling noise in thermal imaging systems", *Infrared Imaging Systems: Design, Analysis, Modeling and Testing IV*, 1993.
- [8] M. Kohin, N. R. Butler, "Performance Limits of Uncooled VOx Microbolometer Focal Plane Arrays", *Proceedings of SPIE*, 2004.
- [9] M. C. de Goffau, K. A. Bergman, H. J. De Vries, et al., "Cold Spots in Neonatal Incubators are Hot Spots for Microbial Contamination", *Applied and Environmental Microbiology*, Vol. 77, No. 24, pp. 8568-8572, 2011.
- [10] S. D. P. Wentworth, D. C. Crawford, S. D. Edwards, "Neonatal Incubator Draeger Caleo", *MHRA evaluation*, Report No. 04020, 2004.
- [11] S. D. P. Wentworth, D. C. Crawford, S. D. Edwards, "Neonatal Incubator / Infant Radiant Warmer Ohmeda Giraffe OmniBed", *MDA evaluation*, Report No. 02090, 2002.
- [12] W. Minkina, D. Klecha, "Atmospheric transmission coefficient modelling in the infrared for thermovision measurements", *J. Sens. Sens. Syst.*, Vol. 5, pp. 17-23, 2016.
- [13] W. Minkina, D. Klecha, "Modeling of Atmospheric Transmission Coefficient in Infrared for Thermovision Measurements", *SENSOR 2015 and IRS² 2015*, AMA Conferences 2015, 2015.
- [14] World Health Organization (WHO), Preterm birth, Factsheet No 363, 2013. <http://www.who.int/en/news-room/fact-sheets/detail/preterm-birth>, [Retrieved 3-9-2018]
- [15] National Institute of Child Health and Human Development: Office of Communications, Preterm Labor and Birth: Condition Information, 2017. <https://www.nichd.nih.gov/health/topics/preterm/conditioninfo/default>, [Retrieved 4-9-2018]
- [16] H. Young, R. Freedman, "University Physics", 10th Ed., Addison-Wesley, 2000.
- [17] K. R. Holmes, T. Adams, "Epidermal thermal conductivity and stratum corneum hydration in cat foot-pad", *Am. J. Physiol.*, Vol. 228, pp. 1903-1908, 1975.
- [18] J. A. Curcio "Adsorption and Condensation of Water on Mirror and Lens Surfaces", *NRL Memorandum Report 3359*, 1976.
- [19] J. E. Castillo, J. A. Weibel, S. V. Garimella, "The Effect of Relative Humidity on Dropwise Condensation Dynamics", *CTRC Research Publications*, Vol. 244, 2015.

- [20] Vereniging van Ouders van Couveusekinderen, Neonatologie en NICU, 2015. <https://www.couveuseouders.nl/neonatologie/neonatologie-en-nicu/> [Retrieved 7-9-2018]
- [21] Manual, I.C.N.H.S., "Very low and extremely low birthweight infants", *The regents of University of California*, 2004.
- [22] S. A. Jurica, A. Čolić, S. Gverić-Ahmetašević, "Skin of the Very Premature Newborn - Physiology and Care", *Paediatr Croat.*, Vol. 60, pp. 21-26, 2016.
- [23] K. Hammarlund, B. Strömberg, G. Sedin, "Heat loss from the skin of preterm and fullterm newborn infants during the first weeks after birth", *Biol Neonate.*, Vol. 50, No. 1, pp. 1-10, 1986.
- [24] J. P. Cloherty, E. C Eichenwald, A. R. Hansen, *Manual of Neonatal Care*, Philadelphia, PA: LIPPINCOTT WILLIAMS & WILKINS, 2012, pp. 180-182, ISBN 978-1-60831-777-6.
- [25] N. Rutter, "The Dermis", *Semin Neonatol.*, Vol. 5, pp. 297-302, 2000.
- [26] EMVA, "GenICam Standard - Generic Interface for Cameras", version 2.1.1, n.d. https://www.emva.org/wp-content/uploads/GenICam_Standard_v2_1_1.pdf [Retrieved 13-4-2020]
- [27] AravisProject, "aravis", n.d. <https://github.com/AravisProject/aravis> [Retrieved 15-04-2020]
- [28] Aravis0.6, "Aravis0.6 (0.6.0)", n.d. <https://lazka.github.io/pgi-docs/Aravis-0.6/index.html#> [Retrieved 15-04-2020]
- [29] curl, "curl://", 2020. <https://curl.haxx.se/> [Retrieved 16-04-2020]
- [30] C. H. Lund, L. B. Nonato, J. M. Kuller, "Disruption of barrier function in neonatal skin associated with adhesive removal", *J Pediatr*, Vol. 131, No. 3, pp. 367-372, 1997.
- [31] GE Healthcare, "Patient Data link for the Giraffe^R and Panda^R Family - Engineering White Paper", 2016.
- [32] Dräger Medical AG & Co. KG, "Protocol Definition - Dräger RS 232 Medibus", Revision 7.00, 2015.
- [33] Dräger Medical AG & Co. KG, "MEDIBUS for Dräger Pediatric Devices - Instructions for Use", 6th Edition, 2007.
- [34] N. Rutter, "Percutaneous drug absorption in the newborn: hazards and uses", *Clin Perinatol*, Vol. 14, No. 4, pp. 911-930, 1987.
- [35] Dräger Caleo[®] Neonatal incubator - *Instructions For Use*, 7th ed., Dräger Medical GmbH, Germany, 2010.
- [36] *GE GiraffeTM Omnibed - Operators Manual*, Ohmeda Medical, Laurel, MD, 2001.
- [37] P. M. Vivier, W. J. Lewander, H. F. Martin, "Isopropyl alcohol intoxication in a neonate through chronic dermal exposure: a complication of a culturally-based umbilical care practice", *Pediatr Emerg Care*, Vol. 10, No. 2, pp. 91-93, 1994.
- [38] J. D. Fernandes, M. C. Machado, Z. N. Oliveira, "Children and newborn skin care and prevention", *An Bras Dermatol*, Vol. 86, No. 1, pp. 102-110, 2011.
- [39] J. M. Conner, R. F. Soll, W. H. Edwards, "Topical ointment for preventing infection in preterm infants", *Cochrane Database Syst Rev*, No. 1, 2004.
- [40] D. J. Watmough, P. W. Fowler, R. Oliver, "The thermal scanning of a curved isothermal surface: implications for clinical thermography", *Phys Med Biol*, Vol. 15, No. 1, pp. 1-8, 1970.
- [41] G. L. Darmstadt, N. Badrawi, P. A. Law, et al., "Topically applied sunflower seed oil prevents invasive bacterial infections in preterm infants in Egypt: a randomized, controlled clinical trial", *Pediatr Infect Dis J*, Vol. 23, No. 8, pp. 719-725, 2004.
- [42] B. F. Jones, "A reappraisal of the use of infrared thermal image analysis in medicine", *IEEE Transactions on Medical Imaging*, Vol. 17, No. 6, pp. 1019-1027, Dec. 1998.

- [43] R. F. Soll, "Heat Loss Prevention in Neonates", *Journal of Perinatology*, Vol. 28, S57-59, 2008.
- [44] L. Stern, "The newborn infant and his thermal environment", *Current Problems in Pediatrics*, Vol. 1, No. 1, pp. 3-29, 1970.
- [45] World Health Organization: Maternal and Newborn Health/Safe Motherhood, Thermal protection of the newborn: a practical guide, *Safe Motherhood*, 1997.
- [46] G. Gandy, M. Adamsons, K. Jr. Cunningham, et al., "Thermal environment and acid-base homeostasis in human infants during the first few hours of life", *J. Clin. Invest.*, Vol. 43, No. 751, 1964.
- [47] L. P. C. Neto, M. C. G. Silva, J. J. Costa, "On the use of infrared thermography in studies with air curtain devices", *Energy and Buildings*, Vol. 38, No. 10, pp. 1194-1199, 2006.
- [48] K. Adamsons, M. E. Towell, "Thermal Homeostasis in the Fetus and Newborn", *Anesthesiology* 7, Vol. 26, No. 4, pp. 531 - 548, 1965.
- [49] K. Lunze, D. E. Bloom, D. T. Jamison, et al., "The global burden of neonatal hypothermia: systematic review of a major challenge for newborn survival", *BMC Medicine*, Vol. 11, No. 24, 2013.
- [50] Champlain Maternal Newborn Regional Program, *Newborn Thermoregulation: Self-Learning Module*, 2013.
- [51] B. J. Stoll, N. I. Hansen NI, I. Adams-Chapman, et al., "Neurodevelopmental and growth impairment among extremely low-birth-weight infants with neonatal infection", *JAMA*, Vol. 292, No. 19, pp. 2357-2365, 2004.
- [52] A. K. Abbas, and S. Leonhardt, "Intelligent neonatal monitoring based on a virtual thermal sensor", *BMC Medical Imaging*, Vol. 14, No. 9, 2014.
- [53] L. Liu, S. Oza, D. Hogan, et al., "Global, regional, and national causes of under-5 mortality in 2000–15: an updated systematic analysis with implications for the Sustainable Development Goals", *The Lancet*, Vol. 388, No. 10063, pp. 3027-3035, 2016.
- [54] Ramé-hart instrument co., Information on Contact Angle, 2018. <http://www.ramehart.com/contactangle.htm> [Retrieved 22-10-2018]
- [55] H. Schneider, N. Niegisch, M. Mennig, et al., "Hydrophilic Coating Materials", In: Aegerter M.A., Mennig M. (eds) *Sol-Gel Technologies for Glass Producers and Users*. Springer, Boston, MA, 2004
- [56] J. Drelich, E. Chibowski, "Superhydrophilic and Superwetting Surfaces: Definition and Mechanisms of Control", *Langmuir*, Vol. 26, No. 24, pp. 18621-18623, 2010.
- [57] J. A. Howarter, J. P. Youngblood, "Self-Cleaning and Next Generation Anti-Fog Surfaces and Coatings", *Macromol. Rapid Commun.*, Vol. 29, pp. 455-466, 2008.
- [58] M. V. Valueva, N. N. Nagornov, P. A. Lyakhov, et al., "Application of the residue number system to reduce hardware costs of the convolutional neural network implementation", *Mathematics and Computers in Simulation*, Vol. 177, pp. 232–243, 2020.
- [59] P. B. Marshall, H. J. Halls, S. L. James, et al., "The Cost of Intensive and Special Care of the Newborn", *Med J Aust*, Vol. 150, No. 10, pp. 568-574, 1989.
- [60] Perined. *Perinatale Zorg in Nederland 2015*. Utrecht: Perined; 2016.
- [61] K. Brück, "Temperature regulation in the newborn", *Biol. Neonat.*, Vol. 3, pp. 65-119, 1961.
- [62] R. Antonucci, A. Porcella, and V. Fanos, "The infant incubator in the neonatal intensive care unit: unresolved issues and future developments", *J. Perinat. Med.*, Vol. 37, 2009.
- [63] M. C. De Goffau, K. A. Bergman, H. J. De Vries, et al., "Cold Spots in Neonatal Incubators Are Hot Spots for Microbial Contamination", *Applied and Environmental Microbiology*, Vol. 77, No. 24, pp. 8568-8572, 2011.

- [64] U.S. Army Night Vision and Electronic Sensors Directorate, Night Vision Thermal Imaging Systems Performance Model - User's Manual & Reference Guide, 2001.
- [65] J. M. Melville, T. J. M. Moss, "The immune consequences of preterm birth", *Frontiers in Neuroscience*, Vol. 7, No. 79, 2013.
- [66] B. L. Tesini, MSD Manual - Professional Version, "Overview of Neonatal Infections", 2018. <https://www.msmanuals.com/professional/pediatrics/infections-in-neonates/overview-of-neonatal-infections> [Retrieved 9-10-2018]
- [67] B. L. Tesini, MSD Manual - Professional Version, "Congenital Rubella", 2018. <https://www.msmanuals.com/professional/pediatrics/infections-in-neonates/congenital-rubella> [Retrieved 10-10-2018]
- [68] B. L. Tesini, MSD Manual - Professional Version, "Congenital and Perinatal Cytomegalovirus Infection (CMV)", 2018. <https://www.msmanuals.com/professional/pediatrics/infections-in-neonates/congenital-and-perinatal-cytomegalovirus-infection-cmv> [Retrieved 10-10-2018]
- [69] A. L. Balest, MSD Manual - Professional Version, "Apnea of Prematurity", 2018. <https://www.msmanuals.com/professional/pediatrics/respiratory-problems-in-neonates/apnea-of-prematurity> [Retrieved 10-10-2018]
- [70] M. Cohen-Wolkowicz, C. Moran, D. K. Benjamin, "Early and late onset sepsis in late preterm infants", *Pediatr Infect Dis J*, Vol. 28, No. 12, pp. 1052-1056, 2009.
- [71] K. A. Simonsen, A. L. Anderson-Berry, S. F. Delair, et al. "Early-Onset Neonatal Sepsis", *Clinical Microbiology Reviews*, Vol. 27, No. 1, pp. 21-47, 2014.
- [72] E. D. Barnett, J. O. Klein, "Bacterial infections of the respiratory tract", In: J. S. Remington, J. O. Klein, *Infectious diseases of the fetus and newborn infant*, Philadelphia: WB Saunders, 5th edition, pp. 1006-1018, 2001.
- [73] T. Duke, "Neonatal pneumonia in developing countries", *Arch Dis Child Fetal Neonatal Ed.*, Vol. 90, No. 3 pp. F211-F219, 2005.
- [74] F. Reiterer, "Neonatal Pneumonia", *Neonatal Bacterial Infection*, pp. 19-32, 2013.
- [75] M. D. Nissen, "Congenital and Neonatal Pneumonia", *Pediatrics Resp. Reviews*, Vol. 8, pp. 195-203, 2007.
- [76] R. J. Martin, M. J. Miller, W. A. Carlo, "Pathogenesis of Apnea in Preterm Infants", *The Journal of Pediatrics*, Vol. 109, No. 5, pp. 733-841, 1986.
- [77] A. Sharma, S. Ford, J. Calvert, "Adaptation for life: a review of neonatal physiology", *Anaesthesia and Intensive Care Medicine*, Vol. 12, No. 3, pp. 85-90, 2010.
- [78] S. Bagavathiappan, T. Saravanan, J. Philip, et al., "Infrared thermal imaging for detection of peripheral vascular disorders", *J Med Phys.*, Vol. 34, No. 1, pp. 43-47, 2009.
- [79] M. Bharara, J. E. Cobb, D. J. Claremont, "Thermography and thermometry in the assessment of diabetic neuropathic foot: a case for furthering the role of thermal techniques", *Int J Low Extrem Wounds*, Vol. 5, No. 4, pp. 250-260, 2006.
- [80] J. B. Mercer, S. P. Nielsen, G. Hoffman, "Improvement of wound healing by water-filtered infrared-A (wIRA) in patients with chronic venous stasis ulcers of the lower legs including evaluation using infrared thermography", *Ger Med Sci.*, Vol. 6, 2008.
- [81] J. E. Lawn, S. Cousens, J. Zupan, et al., "4 million neonatal deaths: when? Where? Why?", *Lancet*, Vol. 365, No. 9462, pp. 891-900, 2005.
- [82] Mayo Clinic Staff, "Anemia", 2017. <https://www.mayoclinic.org/diseases-conditions/anemia/symptoms-causes/syc-20351360> [Retrieved 9-10-2018]

- [83] K. Chardon, V. Cardot, A. Léké, et al., "Thermoregulatory control of feeding and sleep in premature infants", *Obesity*, Vol. 14, No. 9, pp. 1535–1542, 2006.
- [84] S. Arora, "Kangaroo mother care", *Nursing Journal of India*, Vol. 99, No. 11, pp. 248–250, 2008.
- [85] A. K. Abbas, K. Heimann, V. Blazek, et al., "Neonatal infrared thermography imaging: Analysis of heat flux during different clinical scenarios", *Infrared Phys. Technol.*, Vol. 55, No. 6, pp. 538–548, 2012.
- [86] L. S. Rosenblat, "Evaluation of distortion in clinical thermography", *Biomed. Eng. (NY)*, Vol. 12, No. 5, pp. 236–241, 1978.
- [87] H. Kaplan, *Practical Applications of Infrared Thermal Sensing and Imaging Equipment*, Tutorial Texts in Optical Engineering, SPIE Press, 2007. ISBN: 9780819467232.
- [88] L. A. Philips, "Infrared thermography on the spot: Because size does matter", *FLIR in Focus: Cost Justification Series*, 2003.
- [89] R. K. Hobbie, and B. J. Roth, *Intermediate Physics for Medicine and Biology*, 4th ed. New York: Springer Science+Business Media, LLC, 2007. ISBN: 978-0-387-30942-2.
- [90] T. Togawa, "Non-contact skin emissivity: Measurement from reflectance using step change in ambient radiation temperature", *Clin. Phys. Physiol. Meas.*, Vol. 10, No. 1, pp. 39–48, 1989.
- [91] J. Steketee, "Spectral emissivity of the skin and pericardium", *Phys. Med. Biol.*, Vol. 18, No. 5, pp. 686–694, 1973.
- [92] *Infrared Spectral Selection: It Begins with the Detector*, A. Richards, FLIR Systems, 2009. <https://www.photonics.com/Article.aspx?AID=25132> [Retrieved 17-09-2018]
- [93] *The Earth's Atmosphere*, R. Pogge, Ohio State University, 2008. <http://www.astronomy.ohio-state.edu/pogge/Ast161/Unit5/atmos.html> [Retrieved 2-10-2018]
- [94] M. Hu, G. Pei, L. Li, et al., "Theoretical and Experimental Study of Spectral Selectivity Surface for Both Solar Heating and Radiative Cooling", *International Journal of Photoenergy*, Vol. 2015, pp. 1-9, 2015.
- [95] *Environmental humidity for premature neonates*, Tara Doyle, CNS, Butterfly Ward, The Royal Children's Hospital Melbourne, 2016. https://www.rch.org.au/rchcpg/hospital_clinical_guideline_index/Environmental_humidity_for_premature_neonates/ [Retrieved 1-10-2018]
- [96] C. B. Pereira, X. Yu, M. Czaplik, et al., "Remote Monitoring of Breathing Dynamics Using Infrared Thermography", *Optical Society of America*, Vol. 6, No. 11, 2015.
- [97] T. I. Sherman, J. S. Greenspan, N. S. Clair, et al., "Optimizing the Neonatal Thermal Environment", *Neonatal Network: The Journal of Neonatal Nursing*, Vol. 25, No. 4, pp. 251-260, 2006.
- [98] A. M. Smith, M. C. Mancini, S. Nie, "Second window for in vivo imaging", *Nature Nanotechnology*, Vol. 4, pp. 710-711, 2009.
- [99] T. Nunak, K. Rakrueangdet, N. Nunak, et al., "Thermal Image Resolution on Angular Emissivity Measurements using Infrared Thermography", *Proceedings of the International MultiConference of Engineers and Computer Scientists*, Vol. 1, 2015.
- [100] S. S. D. Hamamatsu Photonics K.K., "Characteristics and use of infrared detectors", *Technical Information SD-12*, pp. 43, 2011.
- [101] R. N. Lawson, "Implications of surface temperatures in the diagnosis of breast cancer", *Can. Med. Assoc. J.*, Vol. 75, pp.309-310, 1956.
- [102] E. F. Bell, G. R. Rios, "Air versus skin temperature servocontrol of infant incubators", *J. Pediatr.*, Vol. 103, No. 6, pp. 954-959, 1983.
- [103] R. Kitsommart, S. Phatthanasiriwetin, "Accuracy and Precision of Digital Thermometer in Neonatal Temperature Measurement", *Siriraj Med. J.*, Vol. 57, No. 5, pp. 128-131, 2005.

- [104] What is emissivity and why is it important? (FAQ - Thermal), National Physical Laboratory, 2004. [http://www.npl.co.uk/reference/faqs/what-is-emissivity-and-why-is-it-important-\(faq-thermal\)](http://www.npl.co.uk/reference/faqs/what-is-emissivity-and-why-is-it-important-(faq-thermal)) [Retrieved 21-09-2018]
- [105] Plexiglas General Information and Physical Properties, Altuglas International, Arkema Group, Philadelphia, USA, 2006.
- [106] Y. Mastai, Y. Diamant, S. T. Aruna, et al., "TiO₂ Nanocrystalline Pigmented Polyethylene Foils for Radiative Cooling Applications: Synthesis and Characterization", *Langmuir*, Vol. 17, No. 22, pp. 7118-7123, 2001.
- [107] A. Jaffer, "FreeSnell: Polyethylene". <http://people.csail.mit.edu/jaffer/FreeSnell/polyethylene.html> [Retrieved 21-09-2018]
- [108] S. Vohra, R. S. Roberts, B. Zhang, et al., "Heat Loss Prevention(HeLP) in the Delivery Room: A Randomized Controlled Trial of Polyethylene Occlusive Sking Wrapping in Very Preterm Infants", *The Journal of Pediatrics*, Vol. 145, No. 6, pp. 750-753, 2004.
- [109] R. Nakanishi, K. Imai-Matsumura "Facial skin temperature decreases in infants with joyful expression", *Infant Behav Dev*, Vol. 31, No. 1, pp. 137-144, 2008.
- [110] M. F. Chiang, P. W. Lin, L. F. Lin, et al., "Mass screening of suspected febrile patients with remote-sensing infrared thermography: alarm temperature and optimal distance", *J Formos Med Assoc*, Vol. 107, No. 12, pp. 937-944, 2008.
- [111] W. T. Chiu, P. W. Lin, H. Y. Chiou, et al., "Infrared thermography to mass-screen suspected SARS patients with fever", *Asia Pac J Public Health*, Vol. 17, No. 1, pp. 26-28, 2005.
- [112] D. Bitar, A. Goubar, J. C. Desenclos, "International Travels and Fever Screening During Epidemics: A Literature Review on the Effectiveness and Potential Use of Non-Contact Infrared Thermometers", *Euro-surveillance*, Vol. 14, No. 6, 2009.
- [113] J. W. Fluhr, R. Darlenski, A. Taieb, et al., "Functional skin adaptation in infancy - almost complete but not fully competent", *Exp Dermatol*, Vol. 19, No. 6, pp. 483-492, 2010.
- [114] J. D. Lytle, G. W. Wilkerson, J. G. Jaramillo, "Wideband Optical Transmission Properties of Seven Thermoplastics", *Applied Optics*, Vol. 18, No. 11, 1979.
- [115] B. B. Lahiri, S. Bagavathiappan, T. Jayakumar, et al., "Medical applications of infrared thermography: A review", *Infrared Physics & Technology*, Vol. 55, No. 4, pp. 221-235, 2012.
- [116] D. G. Armstrong, L. A. Lavery, P. J. Liswood, "Infrared dermal thermometry for the high-risk diabetic foot", *Physical Therapy*, Vol. 77, pp. 169-175, 1997.
- [117] Y. Hosaki, F. Mitsunobu, K. Ashida, "Non-invasive study for peripheral circulation in patients with diabetes mellitus" *Annual reports of Misasa Medical Branch*, Vol. 72, pp. 31-37, 2002.
- [118] I. A. Shevelev, "Functional imaging of the brain by infrared radiation (Thermoencephaloscropy)", *Progress in Neurobiology*, Vol. 56, pp. 269-305, 1998.
- [119] H. Fikackova, E. Ekberg, "Can infrared thermography be a diagnostic tool for arthralgia of the temporomandibular joint?", *Oral Surgery, Oral Medicine, Oral Pathology, Oral Radiology and Endodontics*, Vol. 98, pp. 643-650, 2004.
- [120] B. Gratt, M. Anbar, "Thermology and facial telethermography: Part II. Current and future clinical applications in dentistry", *Dentomaxillofacial Radiology*, Vol. 27, pp. 68-74, 1998.
- [121] A. D. Carlo, "Thermography and the possibilities for its applications in clinical and experimental dermatology", *Clinics in Dermatology*, Vol. 13, pp. 329-336, 1995.
- [122] S. -y. Lo, "Meridians in acupuncture and infrared imaging", *Medical Hypotheses*, Vol. 58, pp. 72-76, 2002.

- [123] L. T. Clausing, "Emissivity: Understanding the difference between apparent and actual infrared temperatures", *Infrared Cameras and Emissivity*, Application Note, pp. 1-6, 2005.
- [124] J. T. Costello, C. D. McInerney, C. M. Bleakley, "The use of thermal imaging in assessing skin temperature following cryotherapy: a review", *Journal of Thermal Biology*, Vol. 37, pp. 103-110, 2012.
- [125] R. P. Clark, J. K. Stothers, "Neonatal skin temperature distribution using infra-red colour thermography", *J Physiol*, Vol. 302, pp. 323-333, 1980.
- [126] I. Christidis, H. Zotter, H. Rosegger, "Infrared thermography in newborns: the first hour after birth", *Gynakol Geburtshilfliche Rundsch*, Vol. 43, No. 1, pp. 31-35, 2003.
- [127] A. K. Adams, R. A. Nelson, E. F. Bell, et al., "Use of infrared thermographic calorimetry to determine energy expenditure in preterm infants", *Am J Clin Nutr*, Vol. 71, No. 4, pp. 969-977, 2000.
- [128] R. B. Knobel, B. D. Guenther, H. E. Rice, "Thermoregulation and thermography in neonatal physiology and disease", *Biological Research for Nursing*, Vol. 13, pp. 274-282, 2011.
- [129] Lubuntu, "Lubuntu", 2020. <https://lubuntu.me/> [Retrieved 3-4-2020]
- [130] Influxdata, "influxdata", 2020. <https://www.influxdata.com/> [Retrieved 3-4-2020]
- [131] FLIR, "Infrared Camera Calibration", 2019. <https://www.flir.com/support-center/Instruments/service/infrared-camera-calibration/> [Retrieved 9-4-2020]
- [132] ExifTool, "ExifTool by Phil Harvey", 2020. <https://exiftool.org/> [Retrieved 9-04-2020]
- [133] ExifTool Forum, "enhancement: extract binary data from FLIR radiometric jpg", 2013. <https://exiftool.org/forum/index.php/topic4898.msg23944.html#msg23944> [Retrieved 28-05-2019]
- [134] G. M. Hale, M. R. Query, "Optical Constants of Water in the 200-nm to 200- μm Wavelength Region", *Appl. Opt.*, Vol. 12, pp. 555-563, 1973.
- [135] J. Peckham, S. O'Young, J. T. Jacobs, "Comparison of Medium and Long Wave Infrared Imaging for Ocean Based Sensing", *Journal of Ocean Technology*, Vol. 10, No. 3, pp. 112-128, 2015.
- [136] S. D. P. Wentworth, D. C. Crawford, S. D. Edwards, "Neonatal Incubator Draeger Caleo", *MHRA evaluation*, Report No. 04020, 2004.
- [137] S. D. P. Wentworth, D. C. Crawford, S. D. Edwards, "Neonatal Incubator/Infant Radiant Warmer Ohmeda Giraffe Omnibed", *MDA evaluation*, Report No. 02090, 2002.
- [138] R. Danjoux, Infrared Training Center, "ITC Technical publication 60 Window or External Optics Transmittance", *Technical Publication*, No. 60, 2012.
- [139] R. Usamentiaga, P. Venegas, J. Guerediaga, et al., "Infrared Thermography for Temperature Measurement and Non-Destructive Testing", *Sensors*, Vol. 14, pp. 12305-12348, 2014.
- [140] Q. H. Tran, D. Han, C. Kang, et al., "Effects of Ambient Temperature and Relative Humidity on Sub-surface Defect Detection in Concrete Structures by Active Thermal Imaging", *Sensors*, Vol. 17, pp. 1-18, 2017.
- [141] M. Waldemar, K. Daniel, "Modeling of Atmospheric Transmission Coefficient in Infrared Thermovision Measurements", *AMA Conferences 2015 - SENSOR 2015 and IRS² 2015*, pp. 903 - 907, 2015.
- [142] M. Waldemar, K. Daniel, "Atmospheric Transmission Coefficient Modelling in the Infrared for Thermovision Measurements", *J. Sens. Sens. Syst.*, Vol. 5, pp. 17 - 23, 2016.
- [143] G. Gaussorgues, *Infrared Thermography*, Springer Science+Business Media, B.V., Dordrecht, pp. 552, ISBN:978-94-010-4306-9, 1994.
- [144] S. Passman, L. Larmore, "Atmospheric Transmission", *Rand Paper*, Rand Corporation, Santa Monica, pp. 897, 1956.

- [145] T. S. Huang, G. J. Yang, G. Y. Tang, "A Fast Two-Dimensional Median Filtering Algorithm", *IEEE Transactions on Acoustics, Speech, and Signal Processing*, Vol. ASSP-27, No. 1, pp. 13-18, 1979.
- [146] R. Fisher, S. Perkins, A. Walker, et al., "Median Filter", 2003. <https://homepages.inf.ed.ac.uk/rbf/HIPR2/median.htm> [Retrieved 9-11-2018]
- [147] S. Budzan, R. Wyzgolik, "Remarks on Noise Removal In Infrared Images", *Measurement Automation Monitoring*, Vol. 61, No. 6, pp. 187-190, 2015.
- [148] S. W. Smith, *The Scientist and Engineer's Guide to Digital Signal Processing*, California Technical Pub, pp. 626, ISBN:978-0966017632, 1997.
- [149] W. Heisenberg, "Über den anschaulichen Inhalt der quantentheoretischen Kinematik und Mechanik", *Zeitschrift für Physik*, Vol. 43, No. 3-4 pp. 172-198, 1927.
- [150] C. Valens, "A Really Friendly Guide to Wavelets", 1999.
- [151] J. Xie, "Scalable multi-platform medical system in a distributed environment", Bachelor Thesis, Delft University of Technology, 2019.
- [152] R. Polikar, "The Wavelet Tutorial", *The Engineer's Ultimate Guide To Wavelet Analysis*, 2001.
- [153] S. G. Mallat, "A Theory for Multiresolution Signal Decomposition: The Wavelet Representation", *IEEE Pattern Anal. and Machine Intelligence*, Vol. 11, No. 7, pp. 674-693, 1989.
- [154] S. M. R. Islam, X. Huang, M. Liao, et al., "Image Denoising Based on Wavelet for IR Images Corrupted by Gaussian, Poisson & Impulse Noises", *IJCSNS International Journal of Computer Science and Network Security*, Vol. 13, No. 6, pp. 59-70, 2013.
- [155] W. Swelden, "The Lifting Scheme: A Construction of Second Generation Wavelets", *SIAM Journal on Mathematical Analysis*, 1996.
- [156] D. L. Donoho, "De-Noising by Soft-Thresholding", *IEEE Transactions on Information Theory*, Vol. 41, No. 3, pp. 613-627, 1995.
- [157] F. Deroncourt, "Introduction to Fuzzy Logic", MIT, 2013.
- [158] "Foundations of Fuzzy Logic", MathWorks Benelux, 2018. <https://nl.mathworks.com/help/fuzzy/foundations-of-fuzzy-logic.html> [Retrieved 29-11-2018]
- [159] F. Russo, G. Ramponi, "A fuzzy operator for the enhancement of blurred and noisy images," *IEEE Transactions on Image Processing*, Vol. 4, No. 8, pp. 1169-1174, 1995.
- [160] F. Russo, G. Ramponi, "A fuzzy filter for images corrupted by impulse noise", *IEEE Signal Process. Lett.*, Vol. 3, pp. 168-170, 1996.
- [161] F. Russo, "Fire operators for image processing", *Fuzzy Sets and Systems*, Vol. 103, No. 2, pp. 265-275, 1999.
- [162] S. Schulte, V. DeWitte, M. Nachtegaal, "Fuzzy random impulse noise reduction method", *Fuzzy Sets and Systems*, Vol. 158, pp. 270 - 283, 2007.
- [163] M. S. Nair, G. Raju, "A new fuzzy-based decision algorithm for high-density impulse noise removal", *Signal, Image and Video Processing*, Vol. 6, pp. 579-595, 2012.
- [164] S. J. Russel, P. Norvig, et al., *Artificial Intelligence: A Modern Approach*. Upper Saddle River, New Jersey: Pearson Education, Inc., 2009. ISBN:978-0-13-604259-4
- [165] S. Shalev-Shwartz, S. Ben-David, "Understanding Machine Learning: From Theory To Algorithms". Cambridge: Cambridge University Press, 2014. ISBN: 978-1-107-05713-5
- [166] S. Dreiseitla, L. Ohno-Machado, "Logistic regression and artificial neural network classification models: a methodology review", *Journal of Biomedical Informatics*, Vol. 35, pp. 352-359, 2002.

- [167] J. Watt, R. Borhani, A. K. Katsaggelos, *Machine Learning Refined: Foundations, Algorithms, and Applications*. New York: Cambridge University Press, 2016.
- [168] G. Litjens, T. Kooi, B. E. Bejnordi, et al., "A Survey on Deep Learning in Medical Image Analysis", *Medical Image Analysis*, Vol. 42, pp. 60-88, 2017.
- [169] A. Krizhevsky, I. Sutskever, G. E. Hinton "Imagenet classification with deep convolutional neural networks" *Proc. NIPS*, pp. 1–9, 2012.
- [170] G. E. Dahl, T. N. Sainath, G. .E. Hinton, "Improving deep neural networks for lvcsr using rectified linear units and dropout", *Proc. ICASSP*, pp. 8609–8613, 2013.
- [171] N. Tajbakhsh, J. Y. Shin, S. R. Gurudu, et al., "Convolutional Neural Networks for Medical Image Analysis: Full Training or Fine Tuning?", *IEEE Transactions on Medical Imaging*, Vol. 35, No. 5, pp. 1299-1312, 2016.
- [172] Q. Li, W. Cai, X. Wang, et al., "Medical Image Classification with Convolutional Neural Network", *13th International Conference on Control*, pp. 844-848, 2014.
- [173] H. Mohsen, E. A. El-Dahshan, E. M. El-Horbaty, et al., "Classification using deep learning neural networks for brain tumors", *Future Computing and Informatics Journal*, Vol. 3, No. 1, pp. 68-71, 2018.